Luminescent Bimetallic Two-Coordinate Gold (I) Complexes Utilizing Janus Carbenes

Jie Ma^{1‡}, Jonas Schaab^{2‡}, Sritoma Paul³, Stephen R. Forrest^{3,4,5}, Peter Djurovich², Mark E. Thompson^{1,2*}

¹Mork Family Department of Chemical Engineering and Materials Science, University of Southern California, Los Angeles, CA 90089 USA

²Department of Chemistry, University of Southern California, Los Angeles, CA 90089 USA

³Department of Electrical Engineering and Computer Science, University of Michigan, Ann Arbor, MI 48109, USA

⁴Department of Material Science and Engineering, University of Michigan, Ann Arbor, MI 48109, USA

⁵Department of Physics, University of Michigan, Ann Arbor, MI 48109, USA

[‡] These authors contributed equally

Corresponding Author: Mark E. Thompson, orcid.org/0000-0002-7764-4096, met@usc.edu

Abstract

A series of bimetallic carbene-metal-amide (cMa) complexes have been prepared with bridging biscarbene ligands to serve as a model for the design of luminescent materials with large oscillator strengths and small energy differences between the singlet and triplet states ($\Delta E_{\rm ST}$). The complexes have a general structure (R₂N)Au(:carbene—carbene:)Au(NR₂). The bimetallic complexes show solvation-dependent absorption and emission that is analyzed in detail. It is found that the molar absorptivity of the bimetallic complexes is correlated with the energy barrier to rotation of the metal-ligand bond. The bimetallic cMa complexes also exhibit short emission lifetimes ($\tau = 200$ -300 ns) with high photoluminescence efficiencies ($\Phi_{PL} > 95\%$). The radiative rates of bimetallic cMa complexes are 3 to 4 times faster than that of the corresponding monometallic complexes. Analysis of temperature-dependent luminescence data indicates that the lifetime for the singlet state (τ_{S_1}) of bimetallic cMa complexes are near 12 ns with a $\Delta E_{\rm ST}$ of 40-50 meV. The presented compounds provide a general design for cMa complexes to achieve

small values for $\Delta E_{\rm ST}$ while retaining high radiative rates. Solution processed OLEDs made using two of the complexes as luminescent dopants show high efficiency and low roll-off at high luminance.

Keywords: Janus carbene, bimetallic cMa, high radiative rate, solvatochromism, solution OLEDs

Introduction

The first observation of photoluminescent coinage metal (Cu, Ag, Au) complexes was in 1970, although they were rarely considered for practical applications because of the poor luminescence efficiency of compounds known at that time. A resurgence in interest in the photophysics of coinage metal complexes came with the report of highly luminescent two-coordinate carbene-metal-amide (cMa) complexes of copper, silver and gold. The cMa complexes are composed of a carbene ligand serving as an electron acceptor (A) and an amide ligand as an electron donor (D) bridged by the monovalent metal ion. By judicious choice of the two ligands, a metal perturbed amide-to-carbene interligand charge transfer (ICT) is the lowest energy excited state, which undergoes thermally assisted delayed fluorescence (TADF) with high photoluminescence efficiency (Φ_{PL}). The high luminescence efficiencies of cMa complexes has enabled application in organic electronics, the high redox potentials of the ICT state for the cMa complexes also make them promising candidates as sensitizers for photocatalysis.

Emission from TADF is observed when the lowest excited singlet (S_1) and triplet (T_1) state are close enough in energy ($\Delta E_{ST} < 2000 \, \mathrm{cm}^{-1}$, 250 meV) that the two states are in dynamic equilibrium at room temperature. The cMa complexes have a large separation (~4 Å) between donors and acceptor ligands which leads to a small energy difference between the S_1 and T_1 states, on the order of 100 meV.^{3, 4, 19} Rates for intersystem crossing (k_{ISC}) of over $10^{10} \, \mathrm{s}^{-1}$ have been observed for cMa complexes leading to a rapid equilibrium between the S_1 and T_1 states.² Considering the high Φ_{PL} values for the cMa complexes, as well as the fast ISC rate, the excited state lifetime is approximated by the TADF rate. A steady-state pre-equilibrium approximation allows the radiative lifetime of TADF (and thus the decay rate of the excited state) to be equated to the product of the radiative rate from the S_1 state ($k_r^{S_1}$) and the equilibrium constant between these states $K_{eq}(T_1 \rightleftharpoons S_1)$, equation $1.^{21}$

$$k_r^{TADF} = k_r^{S_1} \cdot K_{eq} \tag{1}$$

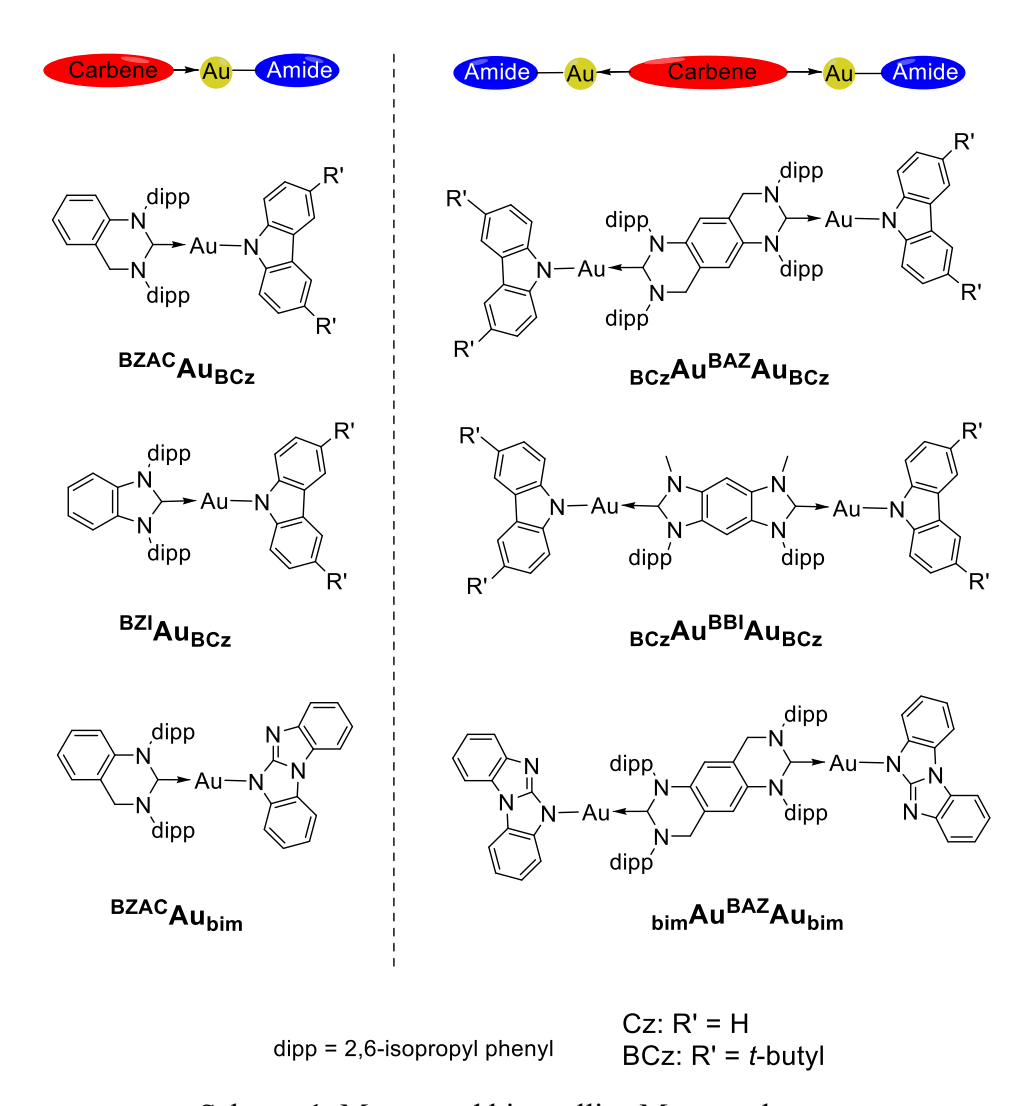
Here, K_{eq} depends on the value of $\Delta E_{\rm ST}$ (eq. S1), which in turn is determined by the Coulombic repulsion between the two unpaired spins in the S₁ and T₁ states. Spatial separation between the hole (h⁺) and electron (e⁻) of the natural transition orbital (NTO) in the lowest excited states decreases $\Delta E_{\rm ST}$, thereby increasing K_{eq} . However, there is a trade-off when optimizing for both $\Delta E_{\rm ST}$ (K_{eq}) and $k_r^{S_1}$. The rate of $k_r^{S_1}$ depends on the transition dipole moment $\mu_{S_0}^{S_1}$, which is tied to the product of h⁺ and e⁻ overlap in the NTO (eq. S2). An increase in the h⁺ and e⁻ separation (and concomitant decrease in orbital overlap) will decrease $\Delta E_{\rm ST}$ (and consequently K_{eq}) but also decrease $k_r^{S_1}$.

Several research groups have performed experimental and theoretical investigations on monometallic cMa complexes having various donors and acceptors with the goal to adjust $k_r^{S_1}$ and $\Delta E_{\rm ST}$. ^{11, 12, 14, 22} For example, by selectively extending the π -system of the carbene or/and amide ligands we prepared cMa complexes with lifetimes ranging from 250 ns to 1 μ s. ^{11, 12} In contrast, photophysical studies of bimetallic cMa complexes applying this approach are scarce. A previous report from our group described a bimetallic cMa complex prepared by extending a mono-nuclear carbene by addition of a second metal-carbene, *i.e.* C: \rightarrow Au-C: \rightarrow Au-Cz where C: is a carbene acceptor, -C: is a bridging ditopic donor-carbene, and Cz in an *N*-carbazolyl donor. ⁹ This bimetallic complex has a small $\Delta E_{\rm ST} = 50$ meV. However, the overlap between the donor-carbene and the amide is poor, leading to a slow $k_r^{S_1}$ and radiative lifetime for TADF of 0.5 μ s.

To further investigate the trade-off between $k_r^{S_1}$ and $\Delta E_{\rm ST}$, an alternative design strategy for bimetallic cMa complexes is presented here. The complexes utilize Janus carbenes, $^{23, 24}$ facially-opposed ditopic ligands, as an acceptor, where each end is coordinated by a metal-amide donor moiety, providing a general structure of amide-metal—:carbene~carbene: \rightarrow metal-amide (aMc~cMa), e.g. BAZ and BBI in Scheme 1. The benefit of this symmetrical D-A-D structural motif is that k_r^{TADF} can be enhanced by an increase in value of $k_r^{S_1}$ or a decrease in the value of $\Delta E_{\rm ST}$ by increasing the h⁺ and e⁻ separation. Extending the excited states over two amides and a Janus carbene moiety is expected to increase the oscillator strength of S₁ state of the chromophore. A similar approach to increase k_r^{TADF} was reported by Yersin, et al, invoking exciton coupling. Alternatively, if the molecular symmetry is broken in the excited state, the bimetallic complex can still benefit from the extended electronic π -system of the Janus carbene,

leading to a decrease in $\Delta E_{\rm ST}$ relative to the monometallic analogs.¹¹ Therefore, based on the equation 1, the overall value for k_r^{TADF} will be enhanced by either mechanism.

Herein we report a series of bimetallic cMa complexes using Janus carbene ligands that have high PL efficiencies ($\Phi_{PL} > 0.95$) and lifetimes for TADF ($\tau < 300$ ns) that are about one third of their monometallic analogs (Scheme 1). The fast TADF rates for the bimetallic complexes come about from short radiative lifetimes from S_1 to S_0 states ($\tau_{S_1} \sim 12$ ns) and a decrease in the exchange energies ($\Delta E_{ST} = 40$ to 50 meV) relative to monometallic analogs. The absorption and emission spectra of these bimetallic complexes are strongly solvent dependent, indicating that two-fold symmetry is lost in the excited states of these materials. Lastly, two of the bimetallic complexes were used as emissive dopants in solution-processed organic light emitting devices (OLEDs) that display high quantum efficiency with low roll-off at high brightness.



Scheme 1. Mono- and bimetallic cMa complexes.

Results and Discussion

Synthesis

The chemical structures of two Janus carbenes used here, 1,3,6,8-tetrakis(2,6-diisopropylphenyl)-3,4,8,9-tetrahydropyrimido[4,5-g]quinazoline-1,6-diium (BAZ) and 3,4-dimethyl-1,7-bis(2,6-diisopropylphenyl)benzobis(imidazolium) iodide (BBI) are shown in Scheme 1. The synthesis of the BAZ ligand was adapted from literature procedures,²³ whereas BBI ligand was prepared by modifying a protocol of Bielawski, *et al.*.^{23, 24} The bulky BBI imidazolate was prepared by treating dichlorodinitrobenzene with an excess of 2,6-diisopropylaniline (DIPA) as both reactant and solvent and heated to 150 °C overnight. The metal chloride precursor complexes were prepared by treatment of BAZ ligand with potassium

bis(trimethylsilyl)amide followed by reaction with (MeS)₂AuCl, whereas the BBI gold chloride complex was prepared using a weaker base (Ag₂O) to prevent polymerization of the BBI ligand (Scheme 2). The final cMa complexes were made using three various deprotonated amides: N-carbazole (Cz), 3,6-di-tert-butylcarbazole (BCz) and N-benzo[d]benzo[4,5]imidazo[1,2-a]-imidazolyl (bim). Their corresponding monometallic complexes were synthesized in an analogous procedure using either 1,3-bis(2,6-diisopropylphenyl)-3,4-dihydroquinazolin-1-ium (BZAC) or 1,3-bis(2,6-diisopropylphenyl)benzo-imidazolium (BZI) acceptor carbenes. The details of synthesis and characterization of the complexes are given in the Support Information.

The bimetallic complexes are significantly less soluble than their monometallic analogs. The solubilities of the three bimetallic complexes in a range of solvents are listed in Table S1. For example, complexes with unsubstituted carbazole ligands are soluble in a moderately polar solvent like THF but insoluble in both polar solvents, such as DMSO and MeCN, as well as non-polar solvents, such as cyclohexane and toluene. Substitution of tert-butyl groups onto the 3,6-positions of carbazolyl (BCz) markedly improves the solubility of the complexes in all solvents, although BCzAu^{BAZ}Au_{BCz} remains less soluble than BCzAu^{BBI}Au_{BCz}. Thus, discussion of electrochemical and photophysical properties on these complexes will be focused on the complexes with BCz and bim ligands (BCzAu^{BAZ}Au_{BCz}, BCzAu^{BBI}Au_{BCz} and bimAu^{BAZ}Au_{bim}) and their corresponding monometallic analogues (BZAC Au_{BCz}, BZIAu_{BCz} and BZAC Au_{bim}).

X = halide or trifluoromethanesulfonate

Scheme 2. Synthesis of bimetallic cMa complexes

Crystallographic Analysis

Single-crystal X-ray structures were determined for bimetallic complexes with BAZ coordinated to Cz, BCz and bim amides, as well as for the monometallic complexes ^{BZAC}Au_{BCz} and ^{BZI}Au_{BCz}. Unfortunately, X-ray quality crystals could not be obtained for bimetallic complexes using the BBI carbene. Crystallographic data are given in Table 1, the Supporting Information and have been deposited in the CCDC database. Representative structures of the compounds of ^{BCz}Au^{BAZ}Au_{BCz} and _{bim}Au^{BAZ}Au_{bim} are shown in Figure 1. The bimetallic complexes crystallize

into centrosymmetric space groups with the inversion center located in the middle of the bridging aromatic ring of the carbene. There are no significant differences in metrical parameters between the bimetallic complexes and the related bonds in the monometallic cMa analogs. 2 , 7 , 11 All complexes display near linear two-coordinate geometries ($C_{carbene}$ -Au- N_{amide} = 175~177°) along with near equal Au- $C_{carbene}$ and Au- N_{amide} bond lengths (1.989-2.020 Å) (see Table 1). The sum of angles around $C_{carbene}$ and N_{amide} are 360°, indicating a trigonal planar geometry for the ligated atoms. The bimetallic complexes crystallize with the carbene and both amides in a near coplanar conformation as dihedral angles for these ligands vary between 0° to 5°. The amide ligands in $b_{im}Au^{BAZ}Au_{bim}$ are oriented antiparallel to each other, with the longer side of the amide opposite to the methylene group of the BAZ carbene (Figure 1b). A notable S-shaped curvature is also apparent in the molecular plane of the complex. This distortion is attributed to crystal packing forces as a planar arrangement of carbene and amides is found in geometry optimized calculations for the same complex (see SI).

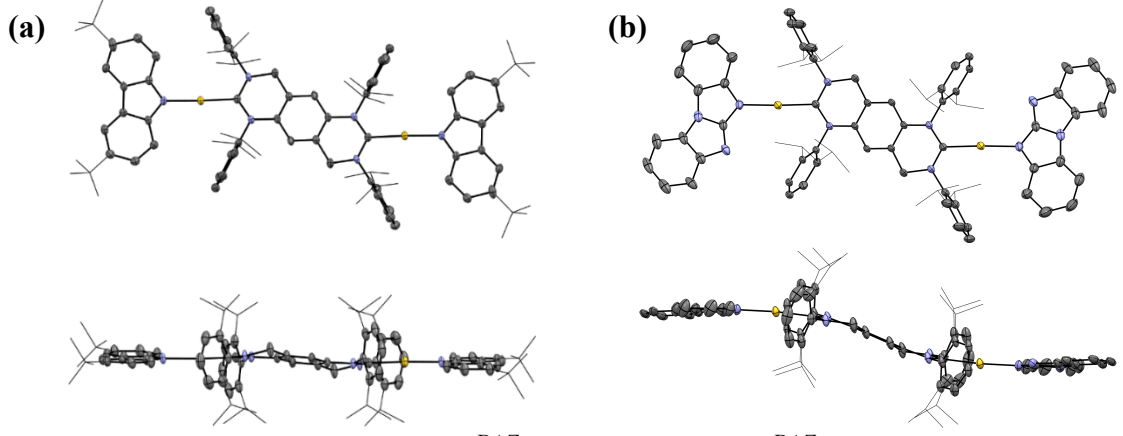


Figure 1. Crystal structures of (a) BCzAuBAZAuBCz and (b) bimAuBAZAubim

Table 1. Selected X-ray crystallographic data.

	Bond 1	ength	Bond angle	Dihedral angle	$\Sigma_{ m Angles}$
Compound	C _{carbene} -Au (Å)	Au - N_{amide} (\mathring{A})	$C_{carbene}$ -Au- N_{amide} (°)	$C_{carbene}$ -Au- N_{amide} (°)	$C_{carbene}$ / N_{amide}
$_{BCz}Au^{BAZ}Au_{BCz}$	1.989(4)	2.007(4)	177.0(2)	5.5	360 / 360
$^{\mathrm{BZAC}}\!Au_{\mathrm{BCz}}$	2.009(4)	2.013(4)	176.8(2)	0.6	360 / 358
$_{Cz}Au^{BAZ}Au_{Cz} \\$	1.995(9)	2.020(7)	177.9(3)	0.6	360 / 358
$_{\text{bim}}Au^{BAZ}Au_{\text{bim}}$	1.993(4)	2.017(3)	175.4(2)	5.4	360 / 360

Computational Results

The electronic structure of the mono- and bimetallic complexes were examined using density functional theory (DFT) and time-dependent DFT (TD-DFT) calculations, with B3LYP/LACVP and cam-B3LYP/LACVP methods, respectively. Simplified carbenes substituted with methyl groups (BBI' and BZI'), in place of bulky dipp moieties, were used to streamline the calculations (Figure 2). The $_{Cz}Au^{BBI'}Au_{Cz}$ complex was optimized using D_{2h} symmetry, and C_{2V} symmetry was applied for the $^{BZI'}Au_{Cz}$ complex. The results for the related derivatives, $^{Cz}Au^{BAZ'}Au_{Cz}$ and $^{bim}Au^{BAZ'}Au_{bim}$, optimized under C_i symmetry, along with their corresponding monometallic complexes, follow the same trends and are included in the Supporting Information (Figure S3-4 and Table S3-7).

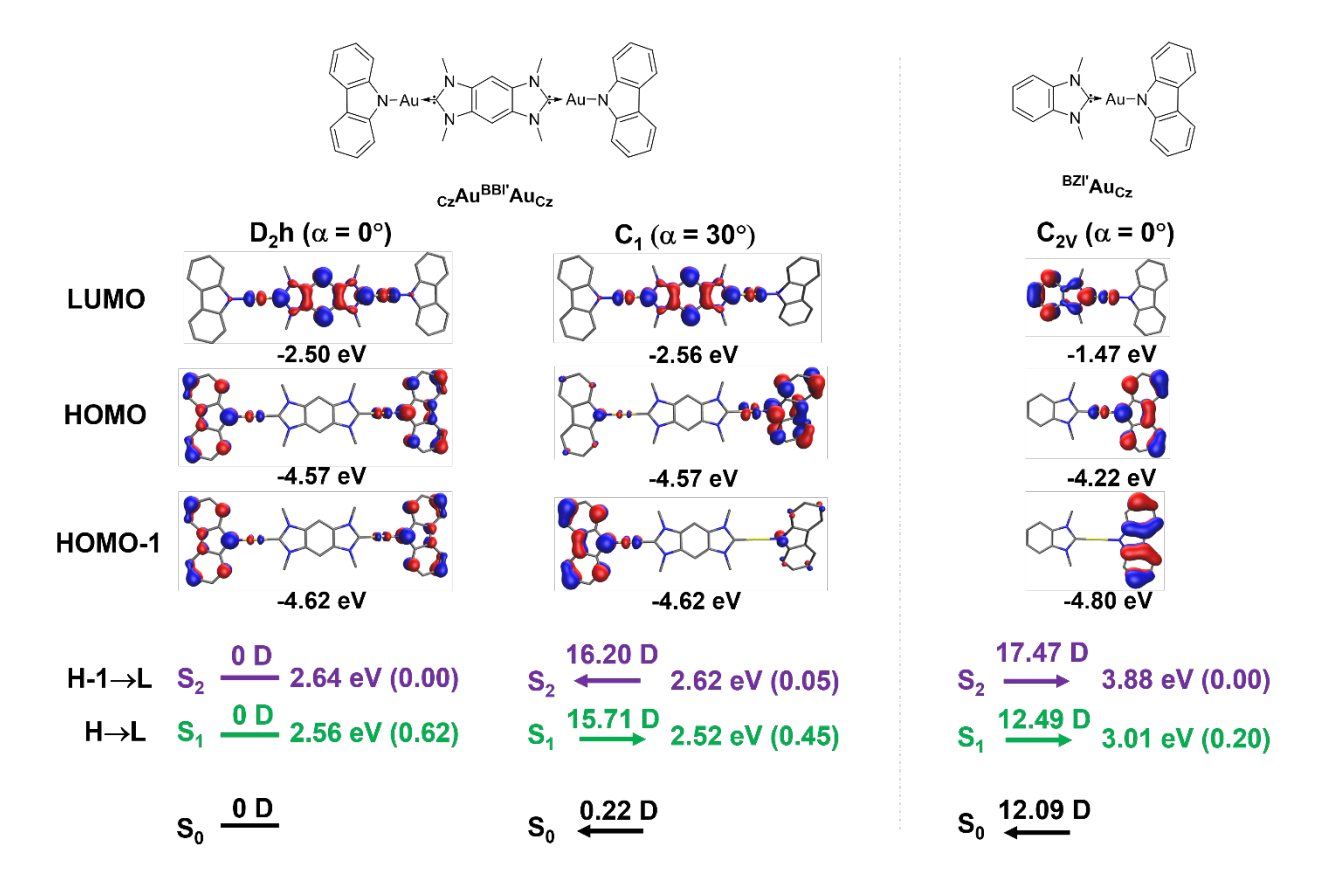


Figure 2. Top: frontier molecular orbitals for $_{Cz}Au^{BBI'}Au_{Cz}$ (left) and $^{BZI'}Au_{Cz}$ (right). The isovalue are set to 0.1. The orbital contributions, energies (oscillator strength) and magnitude of the electronic dipole moment are given for the ground and S_n states below the structures. The direction of the dipole moment for each state is indicated with the arrow.

The $_{Cz}Au^{BBI'}Au_{Cz}$ complex has a HOMO and HOMO-1 comprised of in phase and out of phase combinations of the carbazole π -orbitals that are similar in energy (-4.57 and -4.62 eV, respectively, Figure 2). In contrast, the energy of HOMO-1 for the monometallic analog is roughly 0.6 eV deeper than the HOMO and has no contribution from the nitrogen of the carbazole (Figure 2 right). The lowest unoccupied molecular orbital (LUMO) of $_{Cz}Au^{BBI'}Au_{Cz}$ is delocalized throughout the bridging carbene ligand and stabilized by more than 1 eV relative to the LUMO for $_{BBI'}Au_{Cz}$. The electronic dipole moments for ground and excited states for $_{Cz}Au^{BBI'}Au_{Cz}$ in D_{2h} symmetry are zero. Therefore, the hole density of the S_1 and the lowest triplet excited state (T_1) states distribute evenly over both amides (see Figure S3a). The high symmetry of the bimetallic complex has a significant influence on the oscillator strength for the ICT state. There are two ICT transitions in $_{Cz}Au^{BBI'}Au_{Cz}$, an S_1 state with large oscillator strength (f = 0.62) and a symmetry

forbidden S_2 state (f = 0). Notably, the oscillator strength for the S_1 state of the bimetallic complex is three times larger than that for the S_1 state of $^{BBI'}Au_{Cz}$.

Rotation about the metal-ligand bond can break the two-fold molecular symmetry in bimetallic complexes that markedly alters their electronic properties. Thus, the geometries of the bimetallic complexes in the ground state were also optimized without symmetry. Asymmetry was imparted by constraining one dihedral angle between the carbene and the amides (Cz or bim) at 0° while twisting the other dihedral angle (α) away from 0° . The energies and compositions for the S_1 state are not significantly affected with twist angles up to 20° (Table S3-5). However, when α increases to 30° , the hole of the S_1 state becomes localized on the twisted Cz, the oscillator strength decreases to 0.45, and the net dipole moment for the S_1 state increases to 16 D (Table S3). The magnitude for the dipole moment is comparable to the value for the monometallic analog and indicative of long-range charge transfer in the excited state (Figure 2).^{3, 19} The oscillator strength of the S_1 state decreases as the dihedral angle increases to 90° , at which point the value drops to zero (Figure S4a-c). In brief, a large angle for α ($\geq 20^{\circ}$ for the BAZ based complexes and 30° for the BBI based complex) leads to a low oscillator strength and a large increase in the net dipole moment for the S_1 state of the bimetallic complexes.

To evaluate the energy barrier for rotation about the metal-ligand bond, potential energy surface (PES) calculations were performed using the B3LYP/LACVP method that included a DFT-D3(BJ) dispersion correction. Both mono- and bimetallic complexes with dipp groups were examined by varying the dihedral angles between a carbene and amide from 0° to 180°. The results for these calculations are shown in Figure 3. Energy barriers for rotation from 0° to 180° are similar for corresponding monometallic and bimetallic complexes. The energy barriers for all the derivatives remain low (<1.6 kcal/mol) until dihedral angles reach 30°, which allows facile libration about the metal-ligand bond. Such geometric twisting of the metal-ligand bonds breaks the two-fold molecular symmetry in the bimetallic complexes, particularly in a fluid medium. It is noteworthy that the energy barriers for BZACAubim and bimAuBAZAubim are the lowest among cMa complexes despite the presence of bulky dipp groups on the BAZ ligand. The energy barrier is 5.4 kcal/mol for czAuBAZAucz but only 1.5 kcal/mol for bimAuBAZAubim. The significant decrease in the rotation barriers for cMa complexes with the bim ligand is due to a combination of lower steric hinderance and loss of an attractive edge-to-π interactions present between the C-H bonds

of the carbazole and dipp moieties. An intermediate energy barrier for the $_{Cz}Au^{BBI}Au_{Cz}$ complex of 2.8 kcal/mol is attributed to the absence of one dipp group on each side of carbene and reduced steric interactions imparted by the narrow N-C-N angle of the five-membered ring.

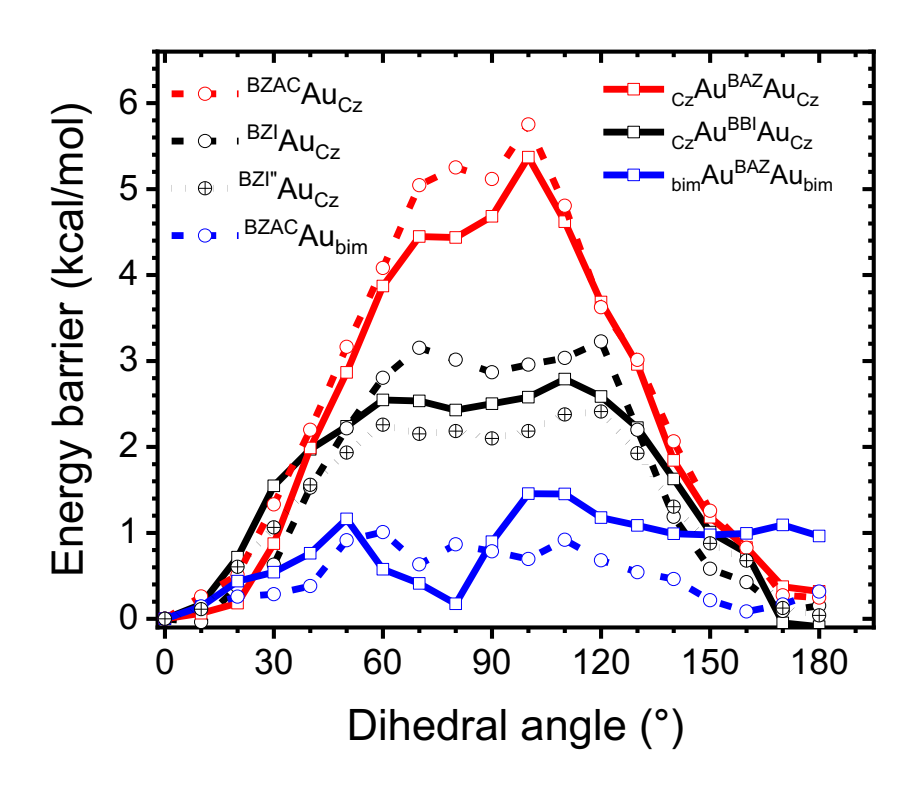


Figure 3. Potential energy surface scan for ligand rotation of the complexes. BZI" is the carbene substituted with a methyl group in place of one dipp moiety.

Electrochemistry

The electrochemical properties of the cMa complexes were examined using cyclic and differential pulse voltammetry (Figure S5), and their redox potentials relative to an internal ferrocene reference are listed in Table 2. The measurements were performed in N,N-dimethylformamide (DMF) solution except for the BAZ based complexes which were carried out in tetrahydrofuran (THF) due to poor solubility in DMF. Unfortunately, the reduction wave of BAZ based complexes overlaps with the THF solvent window and obscures the reduction peak. Thus, the reduction potential for CIAuBAZAuCI measured in DMF was used to estimate the value for BCzAuBAZAuBCZ and bimAuBAZAubim. Previous studies have shown that energies for the LUMO in related two-coordinated complexes are determined by the identity of the carbene and metal ion, but independent of anionic ligand.

Both mono- and bimetallic complexes exhibit reversible anodic waves at similar potentials, ranging from 0.1 V to 0.2 V, that are assigned to oxidation of BCz or bim ligands. The absence of a second oxidation wave for the bimetallic complexes within the potential window of the solvent indicates that the amide ligands are electronically uncoupled. In contrast, reduction waves are irreversible, except for $^{\rm BZI}$ Au_{BCz}. The potentials for the bimetallic complexes are shifted to less negative values by 0.3 V to 0.4 V than their monometallic counterparts (Table 2). This difference is due to stabilization from the extended conjugation in the π -system of the Janus carbene ligands and replicated in the LUMO energies calculated for both types of species.

Table 2. Electrochemical data. Measurements were performed using 0.1 M TBAPF₆ electrolyte in DMF (except where noted), and the potentials are listed relative to a ferrocene internal reference.

compound	oxidation (V)	reduction (V)	redox gap (V)	HOMO ^d (eV)	LUMO ^d (eV)
$_{BCz}Au^{BAZ}Au_{BCz}$	0.07 a	b	2.65	-4.87	-
$_{Cl}Au^{BAZ}Au_{Cl} \\$	-	-2.58	2.65	-	-1.79
$^{\mathrm{BZAC}}\mathrm{Au}_{\mathrm{BCz}}^{}\mathrm{c}}$	0.15 °	-2.83 °	2.95	-4.96	-1.49
$_{BCz}Au^{BBI}Au_{BCz}^{d}$	0.20	-2.44	2.64	-5.02	-1.95
$^{\mathrm{BZI}}\mathrm{Au_{BCz}}^{\mathrm{d}}$	0.21	-2.85	3.06	-5.03	-1.47
$_{\text{bim}}Au^{BAZ}Au_{\text{bim}}$	0.22 a	b	2.80	-5.04	-1.79
$^{\mathrm{BZAC}}\!\mathrm{Au_{bim}}$	0.31 °	-2.69°	3.00	-5.15	-1.66

^a in THF; ^b insoluble in DMF; ^c from reference¹¹; ^d calculated using the equations: HOMO = $-1.15(E_{ox}) - 4.79$; LUMO = $-1.18(E_{red}) - 4.83$ according to reference²⁹.

Photophysical properties

The UV-visible absorption and emission spectra of the complexes were recorded in a toluene solution (Figure 4). The absorption spectra of all complexes display structured bands at high energy (BCz: λ < 350 nm, bim: λ < 380 nm) that are assigned to π - π * transitions localized on the carbene and amide ligands. Absorption maxima at 336 and 352 nm in $_{BCz}Au^{BAZ}Au_{BCz}$ are assigned to π - π * transitions on the carbene as absorption bands at the same wavelength are found in the precursor complex, $_{Cl}Au^{BAZ}Au_{Cl}$ (Figure S7). Broad featureless absorption bands at lower energy (λ > 350 nm) are assigned to transitions from the ICT state. The ICT transitions in the bimetallic complexes are at lower energy than the monometallic analogs consistent with the

stabilization of the LUMO observed in the reduction potentials of complexes. Luminescence at room temperature from all complexes is broad and featureless in all solvents except MeCy, where emission is vibronically structured (Figure 4b, 4d, 5a, S9 and S11) as found in previous literature.², 6,8

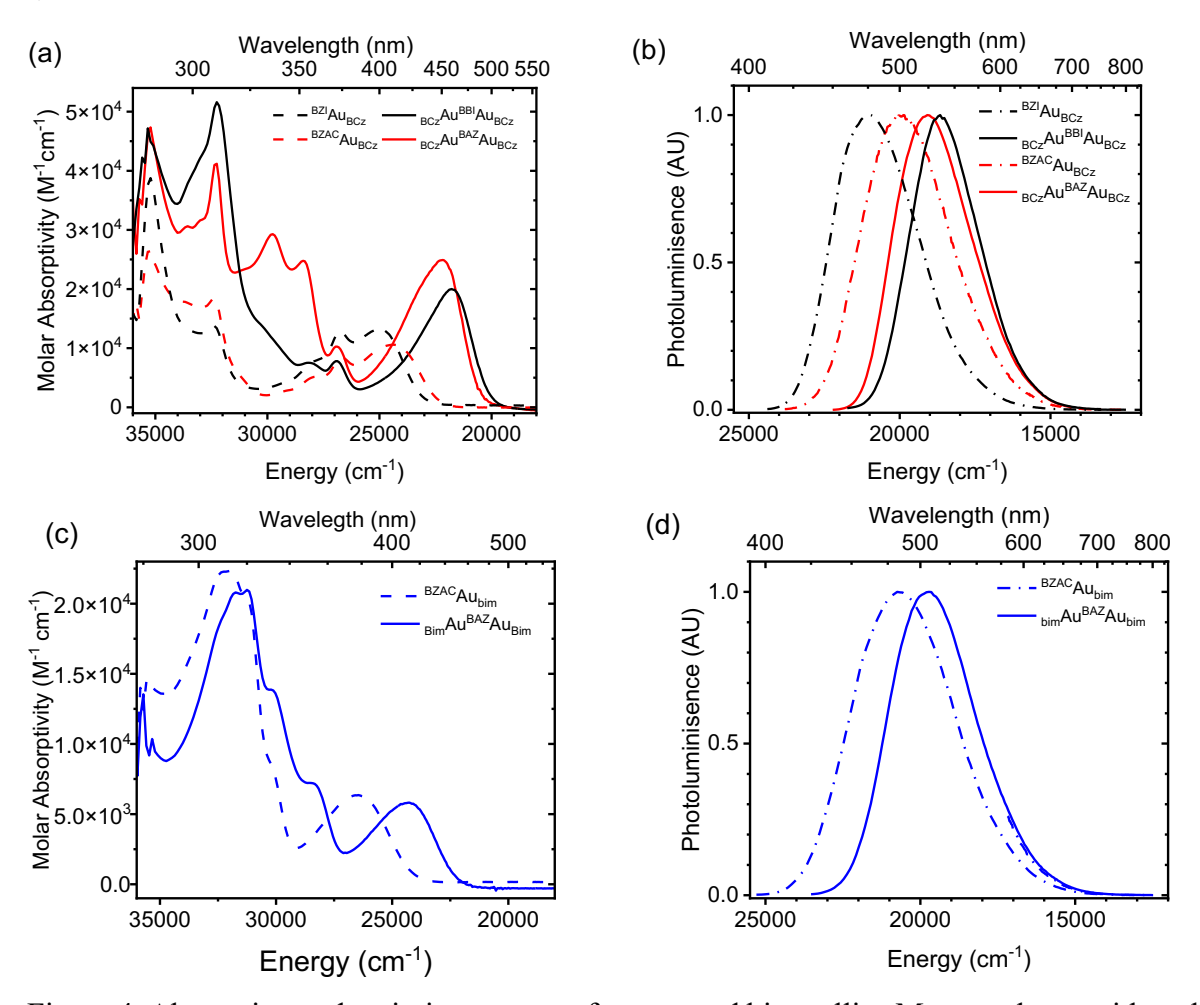


Figure 4. Absorption and emission spectra of mono- and bimetallic cMa complexes with carbazole (a, b) and bim (c, d) in toluene.

The degree of electronic coupling between the amides and Janus carbene in the bimetallic complexes can be assessed from the intensity of the absorption band for the ICT transition.³⁰ For example, the molar absorptivities for the ICT transitions in the bimetallic complexes with BCz donors are larger than those in the monometallic analogs. Integration of the ICT bands (see Figure S6 and Table S10) show an increase by a factor 1.9 for BCzAuBAZAuBCz and 1.3 for BCzAuBBIAuBCz (Table S10). In contrast, the ICT bands for BZACAubim and bimAuBAZAubim have similar molar absorptivities (Figure 4a and c). The intensities follow the same order as the energy barrier to

rotation calculated in the PES scan ($_{BCz}Au^{BAZ}Au_{BCz} > _{BCz}Au^{BBI}Au_{BCz} > _{bim}Au^{BAZ}Au_{bim}$). This correlation suggests that a high percentage of $_{BCz}Au^{BAZ}Au_{BCz}$ molecules have both amides and carbene ligands in a near coplanar geometry since the oscillator strength for the ICT transition is markedly lower for highly twisted geometries. Conversely, the low energy barrier to rotation for $_{bim}Au^{BAZ}Au_{bim}$ leads to a high percentage of molecules with the two amides in a random orientation, thus mitigating any enhancement in molar absorptivity from electronic coupling.

The photostability of each of the bimetallic complexes and their monometallic analogs were tested in degassed toluene using 375 nm excitation (see S10). The complexes with BZAC and BAZ carbenes displayed similar photostability, undergoing less than 10% decrease in absorbance at the λ_{max} of the ICT band after irradiation for 24 h. For comparison, *fac*-Ir(ppy)₃ also showed a 10% decrease in the λ_{max} for the absorption band (380 nm) after 24 h under the same conditions. The complexes with BZI and BBI carbenes decomposed much faster as the absorbance of $_{BCz}Au^{BBI}Au_{BCz}$ complex at the ICT λ_{max} decreased 20%, and a 40% decrease was observed for $_{BZI}Au_{BCz}$ after 24 hours of irradiation.

Solvatochromism is a characteristic feature for the optical properties of monometallic cMa complexes owing to large differences in the magnitude and direction of the dipole moments for the ground and excited states.^{2, 3} This effect gives rise to large hypsochromic shifts in absorption and smaller bathochromic shifts for emission with increasing polarity of solvents. This response to solvent polarity is also displayed in bimetallic complexes (Figure 5a). The energy of the absorption band undergoes a larger solvatochromic shift than does the emission band. This effect can be explained by the solvent reorganization energy being greater in the excited state upon absorption than in the ground state upon emission (see Figure 5b). To evaluate the solvatochromic shift in the ground and excited states, absorption and emission maxima for BZACAuBCz and BCzAuBAZAuBCz are plotted against the solvent polarity indexed using the ET(30) scale in Figure 5c.31 The absorption and emission values for each compound were fit using a linear least squares routine and the slopes are listed in Figure 5d. Similar plots for the other bimetallic complexes and the original data are given in Figure S9 and S13. The absorption and emission maxima of all compounds show a linear dependence with respect to the solvent polarity, indicating that emission originates from a common state in all solvents. The absolute slope for absorption is larger than the one for emission, which is true for all cMa complexes. The slopes of absorption and emission of the bimetallic complexes in the ET(30) plots parallel the slopes of their monometallic analogs, indicating the strength of the transition dipoles are similar for both absorption and emission in mono- and bimetallic complexes. Note that if the bimetallic complex remains symmetric in the ground and excited state, the modeling studies described above predict solvatochromism to be negligible. However, the strong solvatochromic response is indicative of an asymmetric geometry, since rotation of the ligand(s) will cause the excited state to localize largely on only half of the complex. This rotation leads to a large dipole moment for the ICT state, which is similar in magnitude to the value found for the monometallic analog.

Emission spectra from cMa complexes are distinguished by large rigidochromic shifts upon going from fluid solutions to frozen media at low temperatures. Likewise, luminescence spectra for the bimetallic complexes recorded in fluid 2-MeTHF and methylcyclohexane (MeCy) change markedly upon cooling solutions to frozen glass at 77 K (see Figure S11). The featureless ICT emission bands from $_{BCz}Au_{BAZ}Au_{BCz}$ and $_{BCz}Au_{BBI}Au_{BCz}$ blueshift at 77 K and are replaced by narrow, highly structured bands, which are assigned to phosphorescence from a triplet excited state localized on the BCz ligand (^{3}LE). This change occurs because the immobile solvent molecules freeze around the ground state dipole, destabilizing the ICT state so much that it rises above the ^{3}LE state. 2,3 Destabilization of the ICT state occurs to a lesser extent in a polystyrene (PS) matrix at 77 K, leading only to a small blue shift in the ICT emission band. Similarly, the $_{bim}Au_{BAZ}Au_{bim}$ complex displays a narrow, vibronically structured band at 430 nm in 2-MeTHF, MeCy and a PS matrix at 77 K (Figure S11). However, this emission band in this derivative is assigned to a ^{3}LE state localized on the BAZ ligand. The energy of the ^{3}LE state for the bim ligand is higher (E_{00} = 365 nm) than BAZ and therefore the amide does not contribute to emission.

The solvatochromic effects in rigid media at room temperature were examined in polymer matrices. The series ZEONEX® (fully aliphatic copolymer of ethylene and norbornene), PS and polymethylmethacrylate (PMMA) go from nonpolar to moderately polar. The absorption and emission maxima of the CT band for all mono- and bimetallic complexes blue shift upon going from nonpolar (ZEONEX®) to weakly polar PS to moderately polar (PMMA). The Stokes shift between absorption and emission maxima for all complexes is smallest in ZEONEX and largest in PMMA (see Table S14 and Figure S15). The blue shift in absorption in PMMA is consistent with the polymer organizing in response to the ground state dipole moment on deposition, leading to a

destabilization the excited state. Unlike a fluid solvent, the rigid polymer matrix cannot rearrange at room temperature so the "solvent" environment around each emitter remains fixed, leading to a small Stokes shift and a net blue shift in emission relative to the nonpolar ZEONEX® and PS matrices.

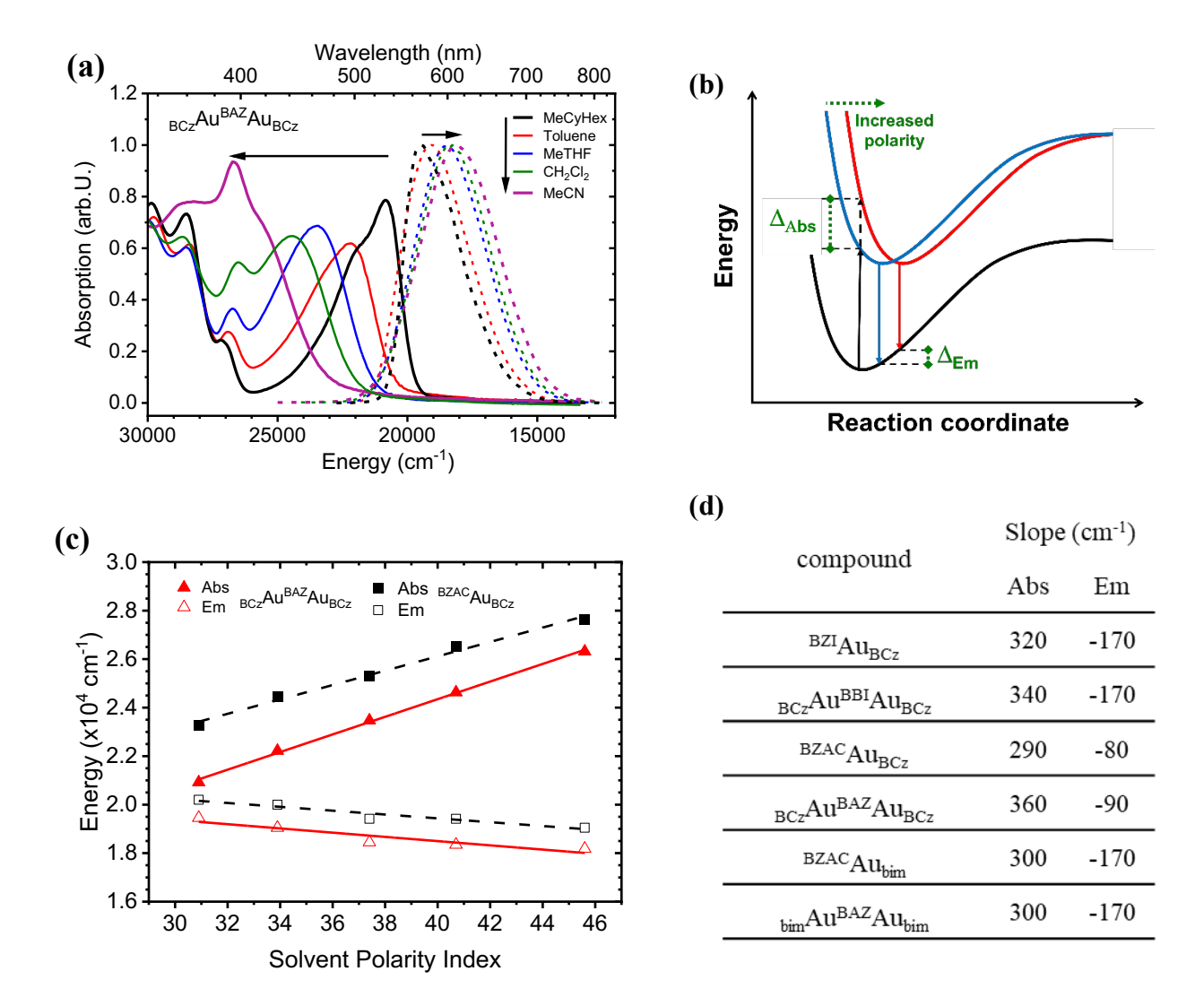


Figure 5: (a) Absorption and emission spectra of $_{BCz}Au^{BAZ}Au_{BCz}$ in various solvents. (b) Qualitative potential surfaces for ground and excited states in solvents polarities. (c) Absorption and emission maxima vs solvent polarity (ET(30) scale) for $_{BCz}Au^{BAZ}Au_{BCz}$ and $^{BZAC}Au_{BCz}$. (d) Slopes of absorption and emission maxima vs ET(30).

An attractive feature of the cMa complexes is their high photoluminescence quantum yields and short emission lifetimes for TADF ($\tau < 1~\mu s$). The bimetallic complexes, like monometallic complexes, can have near unity quantum yields in nonpolar solvents. Quantum yields and emission lifetimes decrease with increasing solvent polarity (Table S11). Similarly, radiative rates decrease

in more polar solvents. The rate for non-radiative decay in all bimetallic complexes is greater than that of the monometallic complexes. The enhanced nonradiative decay rates for bimetallic complexes are likely due to the additional rotational degrees of freedom introduced by the second metal-amide ligand rotor and lower energy for emission (energy gap law). ^{28, 32, 33} Importantly, the bimetallic complexes with BCz donor ligands have radiative rates for TADF that are significantly faster than their monometallic analogs (see Table 3 and S11). Hence, $_{BCz}Au^{BAZ}Au_{BCz}$ and $_{BCz}Au^{BBI}Au_{BCz}$ complexes have radiative rates around $3{\sim}4\times10^6\,\mathrm{s}^{-1}$, whereas the highest radiative rates of monometallic analogs are near $1.5\times10^6\,\mathrm{s}^{-1}$. Both bimetallic complexes also have near unit quantum yields in PS films ($\Phi_{PL}\geq0.9$). In contrast, the radiative rate for $_{bim}Au^{BAZ}Au_{bim}$ in toluene is only marginally faster with respect to its monometallic analog. The photoluminescence quantum yields in PS films for this derivative are also lower than the other bimetallic derivatives ($\Phi_{PL}=0.76$).

To probe the origin of the fast radiative rates for TADF in the bimetallic complexes, temperature dependent photophysical measurements were carried out from 4 K to 300 K in doped PS films (see SI). An Arrhenius model for emission decay was used to fit data in the temperature region of 200-300 K, where TADF is the dominant mechanism emission, to extract values for k_{S_1} and ΔE_{ST} (Table 4 and Figure S15a-c). At temperature below 200 K, the emission decay at each temperature was also fit to a three-level Boltzmann model (see SI), which gives the zero-field splitting (ZFS) and the radiative rate for the T_1 state. Data for $^{\rm BZI}Au_{\rm BCz}$ is not included in Table 3 because the 3 ICT state and 3 LE state on the BCz ligand have energies close enough to only give biexponential emission decays traces that change in contributions upon cooling to cryogenic temperatures (see SI). Data for $_{\rm bim}Au^{\rm BAZ}Au_{\rm bim}$ is included, despite also having transient decay traces in PS films that required biexponential fits. However, as opposed to $^{\rm BZI}Au_{\rm BCz}$, a second longer lived component contributed steadily by 20% to the overall decay trace from 200-300 K. This allowed us to assume that the decay mechanism is invariant over this temperature range. Thus, only the first (faster) decay trace was used for data evaluation of this complex as TADF is the sole mechanism for this process.

Table 3. Photophysical data for mono- and bimetallic cMa complexes in toluene and polystyrene films.

complexes	$abs \ \lambda_{max} \\ (nm)$	$\begin{array}{c} em \; \lambda_{max} \\ (nm) \end{array}$	Ф _{РL} (%)	τ (μs)	$\frac{k_r}{(10^6 \text{ s}^{-1})}$	k_{nr} (10 ⁶ s ⁻¹)	λ _{max} 77 K (nm)	τ 77 K (μs)
				toluene				
$^{\mathrm{BZI}}\mathrm{Au}_{\mathrm{BCz}}$	400	475	94	0.64	1.5	0.09	-	-
$_{BCz}Au^{BBI}Au_{BCz} \\$	455	535	>95	0.24	3.9	< 0.01	-	-
$^{\mathrm{BZAC}}\mathrm{Au}_{\mathrm{BCz}}$	410	500	>95	0.56	1.7	< 0.01	-	-
$_{BCz}Au^{BAZ}Au_{BCz} \\$	450	525	90	0.33	2.7	0.3	-	-
BZAC Aubim	380	480	>95	0.43	2.3	< 0.01	-	-
$_{\text{bim}}Au^{BAZ}Au_{\text{bim}}$	410	505	78	0.29	2.7	0.8	-	-
			1 wt%	polystyrene f	ilm			
BZI Au _{BCz}	-		94	1.58 (0.5) 8.98 (0.5)	-	-	445	65 (0.3) 219 (0.7)
$_{BCz}Au^{BBI}Au_{BCz} \\$	-	515	93	0.21	4.3	0.33	505	25
$^{\mathrm{BZAC}}\mathrm{Au}_{\mathrm{BCz}}$	-	484	>95	0.72	1.4	< 0.01		
$_{BCz}Au^{BAZ}Au_{BCz} \\$	-	506	90	0.30	3	0.33	506	50
$^{\mathrm{BZAC}}\!\mathrm{Au_{bim}}$	-	452	>95	0.28	3.7	< 0.01	-	-
$_{\text{bim}}Au^{BAZ}Au_{\text{bim}}$	-	475	76	0.33 (0.8) 2.85 (0.2)	-	-	455	27 (0.2) 346 (0.8)

Comparison of the k_{S_1} and ΔE_{ST} parameters allows us to determine the origin of the fast rates for TADF found for the bimetallic complexes (Table 4). Both mono- and bimetallic complexes have similar values for k_{S_1} , whereas values of ΔE_{ST} for the latter derivatives are found to be much smaller ($\Delta E_{ST} = 70$, 54 and 43 meV for $^{BZAC}Au_{BCz}$, $_{BCz}Au^{BAZ}Au_{BCz}$ and $_{BCz}Au^{BBBi}Au_{BCz}$, respectively). Thus, the high radiative rate for the bimetallic complexes is mainly attributed to the significant increase in K_{eq} induced by the small ΔE_{ST} imparted by the π -extended Janus carbene (see eq 1). This conclusion is consistent with the calculated distance between the centers of positive and negative charge ($d(h^+, e^-)$) in the S_1 state. We recently determined the relationship between $d(h^+, e^-)$ and k_r^{TADF} for related monometallic cMa complexes. In general, a larger separation of h^+ and e^- leads to a smaller ΔE_{ST} , and therefore a faster rate for k_r^{TADF} . The $d(h^+, e^-)$ values calculated for $_{BCz}Au^{BAZ}Au_{BCz}$ and $_{BCz}Au^{BBI}Au_{BCz}$ (6.17 and 6.87 Å, respectively), are larger than

for $^{\text{BZAC}}\text{Au}_{\text{BCz}}$ (5.19 Å) (Table S8-9), which is consistent with a decrease in ΔE_{ST} for the bimetallic complexes. The details for calculating $d(h^+, e^-)$ are included in the Supporting Information.

The value of k_T^{TADF} for $_{\text{bim}}\text{Au}^{\text{BAZ}}\text{Au}_{\text{bim}}$ complex is not faster than the mono-nuclear analog despite having a value for ΔE_{ST} of 20 meV, one of the smallest ΔE_{ST} values reported to date for 2-coordinate TADF complexes. ^{2, 11, 13-15} The difference in ΔE_{ST} values is consistent with the larger value of $d(h^+, e^-)$ for $_{\text{bim}}\text{Au}^{\text{BAZ}}\text{Au}_{\text{bim}}$ (6.29 Å) than for $_{\text{BZAC}}^{\text{BZAC}}\text{Au}_{\text{bim}}$ (5.39 Å) (Table S8-9); however, the S₁ state for $_{\text{bim}}\text{Au}^{\text{BAZ}}\text{Au}_{\text{bim}}$ has a slower radiative lifetime ($\tau_{S_1} = 50$ ns) than does $_{\text{BZAC}}^{\text{BZAC}}\text{Au}_{\text{bim}}$ ($\tau_{S_1} = 19$ ns). These parameters likely originate from the low energy barrier to rotation for the bim ligand (see Figure 3). The presence of two rotation centers in $_{\text{bim}}\text{Au}^{\text{BAZ}}\text{Au}_{\text{bim}}$ increases the probability that at least one amide ligand is rotated out of plane in the molecule. The large fraction of molecules with amide ligands in highly twisted conformations will lead to an overall increase in τ_{S_1} . Thus, the opposing effects of a decrease in ΔE_{ST} and increase in τ_{S_1} results in similar radiative rates of TADF for $_{\text{BZAC}}^{\text{BZAC}}\text{Au}_{\text{bim}}$ and $_{\text{bim}}^{\text{BAZ}}\text{Au}_{\text{bim}}$.

Table 4. Energy and rate data from variable temperature photophysical measurements for mono- and bimetallic cMa complexes in polystyrene films (1 wt%).

	$ au_{S_1}$ (ns) $\pm 9\%$	ΔE_{ST} (meV / cm ⁻¹) $\pm 3\%$	$ au_{T_1} ag{\mu s} ag{5\%}$	ZFS (meV / cm ⁻¹) ± 10%	h ⁺ /e ⁻ pair distance in S ₁ state (Å)
$^{\mathrm{BZI}}\mathrm{Au}_{\mathrm{BCz}}$	a	a	a	a	a
$_{BCz}Au^{BBI}Au_{BCz} \\$	12.6	43 / 346	33.1	1.1 / 9	6.87
$^{\mathrm{BZAC}}\!\mathrm{Au}_{\mathrm{BCz}}$	14.0	70 / 564	46.7	1.0 / 8	5.19
$_{BCz}Au^{BAZ}Au_{BCz} \\$	12.7	54 / 432	32.9	0.9 / 7	6.17
$^{\mathrm{BZAC}}\!\mathrm{Au_{bim}}$	19 ^b	41 / 330 ^b	19 ^b	1.2 / 10 ^b	5.39
$_{\text{bim}}Au^{BAZ}Au_{\text{bim}}$	50°	20 / 161°	d	d	6.26

^a Luminescence from the ³LE state below room temperature contributed to the lifetime and was changing contribution upon cooling, preventing a determination of all values.

b Data from reference

^c Biexponential decay is observed due to aggregation, even at concentrations <0.1 wt-%. Only the fast component was used to determine $\Delta E_{\rm ST}$ and τ_{S_1} as the relative amplitude stayed constant at 0.65 in the measured temperature range.

^d Luminescence from the ³LE state on BAZ at temperatures below 150 K prevented accurate fits of the ³ICT parameters to determine τ_{T_1} and ZFS.

OLEDs

The high photoluminescence efficiencies and radiative rates of the bimetallic complexes make them promising candidates as luminescent dopants for OLEDs. Thermogravimetric analysis under flowing nitrogen showed that BCzAuBBIAuBCz and BCzAuBAZAuBCz both undergo a 10% weight loss at 315 °C. Attempts to sublime the materials under vacuum at temperatures approaching 315 °C led to decomposition of the material and no observable sublimation. Therefore, emissive layers for the devices were prepared using solution processing methods. The monometallic MACAucz complex was chosen as an emissive dopant for comparative purposes as this derivative has HOMO, LUMO and emission energies that are similar to the bimetallic complexes. The host material tris(4-carbazoyl-9-ylphenyl)amine (TCTA) was selected due to its low barrier for hole injection, high hole mobility and ability to disperse the dopants in the matrix. Photoluminescence data for the cMa complexes doped into TCTA films are given in Table 5. Photoluminescence (PL) spectra of the films were exclusively from the dopant (Table S14). The BCzAu^{BBI}Au_{BCz} complex has a higher Φ_{PL} than BCzAu^{BAZ}Au_{BCz} in a TCTA thin film. The lower Φ_{PL} could be due to a higher degree of aggregation for _{BCz}Au^{BAZ}Au_{BCz}, leading to greater selfquenching for BCzAuBAZAuBCz than the BBI analog. This observation is consistent with lower solubility of BCzAuBAZAuBCz in liquid solution compared to BCzAuBBIAuBCz (Table S1). All three complexes show a decrease in Φ_{PL} and radiative rate with increasing concentration that is consistent with static quenching caused by aggregation of the dopant (see Table S16).

Table 5: Photophysical characterization of cMa complexes doped into thin films of TCTA (10 wt%).

complex	$\Phi_{\mathrm{PL}}(\%)$	τ(ns)	$k_{\rm r}(10^6~{\rm s}^{-1})$	$k_{\rm nr}(10^6{\rm s}^{-1})$
$^{ m MAC}{ m Au_{Cz}}$	79	752	1.1	0.28
$_{BCz}Au^{BBI}Au_{BCz} \\$	74	209	3.5	1.2
$_{BCz}Au^{BAZ}Au_{BCz} \\$	50	250	2.0	2.0

OLEDs were fabricated with the general structure ITO/MoO_x (5 nm)/10% dopant in TCTA (30 nm)/TPBi (50 nm)/Liq (1.5 nm) / Al (100 nm). The layer of MoO_x deposited onto the ITO was used to passivate the ITO surface, facilitate hole injection and improve device stability (see Figure S18) relative to the commonly used PEDOT:PSS.³⁴ The optimal thickness for the MoO_x layer is 5 nm. Devices with a 10 nm of MoO_x layer lead to less uniform organic film coverage and give

high dark currents and turn-on voltages. Devices were fabricated at doping levels of 5%, 10%, 15% and 20%, with the 10% doping giving the best device performance (see Figure S19). Details of process and devices used to optimize these device structures are included in the SI.

The characteristics of optimized devices are shown in Figure 6 and Table 6. The energy levels for frontier orbitals for the materials used in the device are shown in Figure 6b. The energy levels of the dopants are nested within those of hosts, so it is expected that charges will be both carried and trapped by the dopants. The electroluminescence spectra are identical to the photoluminescence spectra of a given dopant, indicating no contribution from either host or ETL material. The current-voltage characteristics show higher current at a given bias for devices using BCzAuBAZAuBCz compared to those using BCzAuBBIAuBCz and MACAuCz (Figure 6c). Further, the BCzAuBAZAuBCz device turns on at a lower voltage (2.5 V) than either the BCzAuBBIAuBCz (2.7 V) or MACAuCz device (2.8 V), and shows a higher current density between turn on and 10 V, likely due to differences in charge mobility. The MACAuCz device has an external quantum efficiency (EQE) of 14% at 6.2 V with a luminance of 300 cd/m², whereas the BCzAuBBIAuBCz device reaches a higher EQE (17%) at 6.1 V at a comparable luminance (Figure 6c,d). In contrast, devices using BCzAuBAZAuBCz reach an EQE = 11% at 3.5 V with a luminance of 6 cd/m² and achieves a stable performance of EQE = 10% at 5.5 V with a luminance of 280 cd/m².

The Φ_{PL} limits the highest possible EQE that can be achieved for a given dopant in the EML. If the EQE_{max} is divided by the Φ_{PL} of that dopant in the same matrix, one can obtain an EQE that would be achieved if the dopant had $\Phi_{PL} = 1.0$. The EQE values adjusted to unity PL efficiency are 18, 22 and 23 % for $^{MAC}Au_{Cz}$, $_{BCz}Au^{BAZ}Au_{BCz}$ and $_{BCz}Au^{BBI}Au_{BCz}$, respectively. Therefore, the solution-processed OLEDs give the maximum theoretical efficiency for OLEDs of 20% without extrinsic or intrinsic (dopant alignment) outcoupling enhancement. The brightness and EQE values for all the devices are comparable to other solution processed OLEDs using cMa dopants. 17, 18, 36-38

The roll-off in EQE with increasing current density for the ^{MAC}Au_{Cz} device is 50% from 1 to 100 mA/cm². In contrast, the roll-off for the device with the _{BCz}Au^{BBI}Au_{BCz} emitter is only 40% in the same range, which suggests that a fast radiative rate helps suppress luminescence quenching by triplet-triplet (TTA) or triplet-polaron annihilation (TPA).

Table 6: OLED device performance.

 $\begin{array}{l} \textbf{--} _{BCz}Au^{BAZ}Au_{BCz} & \textbf{--} _{MAC}Au_{Cz} \\ \textbf{--} _{BCz}Au^{BBI}Au_{BCz} & \textbf{--} \text{TCTA} \end{array}$

	Von	EQE _{max}	1 mA cm ⁻²		100	mA cm ⁻²	λ_{\max} (nm),
dopant	(V)	(%)	EQE (%)	luminance (cd/m²)	EQE (%)	luminance (cd/m ²)	CIE
$^{MAC}\!Au_{Cz}$	2.8	14	14	440	7	22,000	531, (0.25, 0.45)
$_{BCz}Au^{BBI}Au_{BCz} \\$	2.7	17	17	610	10	34,000	526, (0.21, 0.48)
$_{BCz}Au^{BAZ}Au_{BCz}$	2.5	11	10	320	5	18,000	534, (0.27, 0.50)
(a)			(C) 10 ³				10 ⁷
	N		(2 ± 10 ² ± 10 ¹	BCzAu ^{BBI} Au _{BCz} BCzAu ^{BAZ} Au _{BCz} MACAu _{Cz}			10 ⁶
	_		Current density (mA/cm ²)				10⁴ B)
TAPC		TCTA	S 10 ⁻² ep ≠ 10 ⁻³				10 ³ 90 uniu ance
N-N-N-N-N-N-N-N-N-N-N-N-N-N-N-N-N-N-N-	iPr-	N iPr	O nr.e				10 ¹ 5
N=N	iPr-	Au—N iPr	10 ⁻⁶	0 2	4 6	8 10	10 ⁻¹
ТРВі		^{MAC} Au _{Cz}			Voltage	(V)	
(b)			(d)	· · · · · · · · · · · · · · · · · · ·			
-1.9 -1.9 = = = = = -2.0	1.	64	45				
ITO		LiF/Al	15 ②		*****		
<u> </u>	= =-5.0		EQE (%)	1.0	•••••••••		
5.5 -5.7	l	<u>.∠</u> ——	5	El in the sign of		■ _{BCz} Au ^{BE} • _{BCz} Au ^{BA}	Z _{Aun}
5nm 30n		nm	0.0	0.0 500 600 Wavelength (n	700 m)	▲ MACAu _C	z 100
_{BCz} Au ^{BAZ}	Au _{BCz} -	MACAu _{Cz}	0.0	O.1		/m / / / / / / / / / / / / / / / / / /	100

Figure 6: Device characteristics of OLEDs using BCzAuBBIAuBCz, BCzAuBAZAuBCz and MACAuCz dopants. (a) Molecular structures of host and electron transport materials. (b) Device architecture with HOMO and LUMO levels in eV. (c) Current-voltage and luminance-voltage curves. (d) Efficiency (EQE) curves and electroluminescence spectra (inset).

Current Density (mA/cm²)

Conclusion

In summary, we have designed and synthesized a series of luminescent bimetallic cMa complexes by using Janus carbenes to bridge Au-amide moieties. The presence of one donor on each side of Janus carbene maintains the high oscillator strength between the donors and central carbene acceptor. Luminescence from the bimetallic complexes occurs via TADF and spans from blue ($\lambda_{em} = 470$ nm) to green ($\lambda_{em} = 540$ nm) with PL efficiencies close to unity. The bimetallic complexes can have radiative rates that are 2~3 times faster than their monometallic analogs. Theoretical and photophysical analyses show that the fast radiative rate is due to a decrease in the singlet-triplet energy gap caused by spatial extension of the ICT exciton over the entire Janus carbene ligand. OLEDs fabricated using solution-based deposition methods utilizing the bimetallic complexes as dopants give high luminance efficiency. Moreover, MoO_x as the hole injection material is a viable alternative to PEDOT:PSS. The small roll-off demonstrates that fast radiative rate of the emitter can indeed suppress the TTA and TPA in the devices.

Supporting Materials

The supplementary crystallographic data for this paper has been deposited at the Cambridge Crystallographic Data Centre (CCDC numbers: 2206141, 2233511, 2206146, 2216913 and 2216906). These data can be obtained free of charge via www.ccdc.cam.ac.uk/data_request/cif, or by emailing data_request@ccdc.cam.ac.uk. In addition, a supporting information document accompanies this publication containing Synthesis description, ¹H- and ¹³C-NMRs, electrochemistry (CV and DPV) spectra, thermal gravimetric analysis (TGA) spectra, all Photophysical characterizations as well as HOMO, LUMO, and spin-density calculations for all complexes. This can be downloaded from DOI: XXX.

Acknowledgements

The authors would like to thank Dr. Yongxi Li, Xinjing Huang and Haonan Zhao from the University of Michigan for very helpful discussions regarding solution processing of OLEDs, and Dr. Eric McClure for help on molecular modeling. The authors would like to acknowledge the Department of Energy, Office of Basic Energy Science, Award: DE-SC0016450 (Thompson), the Department of Energy, Office of Energy Efficiency and Renewable Energy, Award: EE0009688 (Forrest, Ma and Schaab) and the Universal Display Corporation (Djurovich, Paul) for support. Funds were provided by the National Science Foundation (Award: CHE-2018740) to acquire the

X-ray diffractometer that was used to determine the crystal structures reported here. In addition, we thank National Science Foundation (DBI-0821671, CHE-0840366) and National Institute of Health (S10 RR25432) for funds to acquire the NMR spectrometers used in our work.

Statement of competing interests: Two of the authors, Mark Thompson and Stephen Forrest have a financial interest in the Universal Display Corporation (UDC), one of the funding sources for this work. Forrest's conflict is under management by the University of Michigan Office of the Vice President for Research. Also, the University of Michigan has a license agreement with UDC.

References

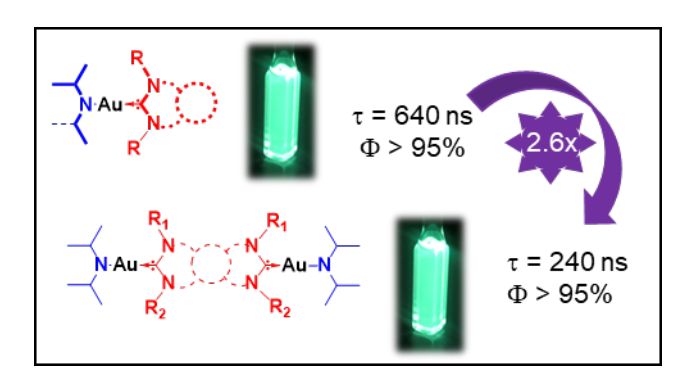
- 1. Ziolo, R. F.; Lipton, S.; Dori, Z., The Photoluminescence of Phosphine Complexes of D10 Metals. Journal of the Chemical Society D: Chemical Communications 1970, (17), 1124-1125, DOI: 10.1039/C29700001124
- 2. Hamze, R.; Shi, S.; Kapper, S. C.; Muthiah Ravinson, D. S.; Estergreen, L.; Jung, M.-C.; Tadle, A. C.; Haiges, R.; Djurovich, P. I.; Peltier, J. L.; Jazzar, R.; Bertrand, G.; Bradforth, S. E.; Thompson, M. E., "Quick-Silver" from a Systematic Study of Highly Luminescent, Two-Coordinate, D10 Coinage Metal Complexes. *Journal of the American Chemical Society* **2019**, *141* (21), 8616-8626, DOI: 10.1021/jacs.9b03657
- 3. Shi, S.; Jung, M. C.; Coburn, C.; Tadle, A.; Sylvinson M. R, D.; Djurovich, P. I.; Forrest, S. R.; Thompson, M. E., Highly Efficient Photo- and Electroluminescence from Two-Coordinate Cu(I) Complexes Featuring Nonconventional N-Heterocyclic Carbenes. *Journal of the American Chemical Society* **2019**, *141* (8), 3576-3588, DOI: 10.1021/jacs.8b12397
- 4. Feng, J.; Reponen, A.-P. M.; Romanov, A. S.; Linnolahti, M.; Bochmann, M.; Greenham, N. C.; Penfold, T.; Credgington, D., Influence of Heavy Atom Effect on the Photophysics of Coinage Metal Carbene-Metal-Amide Emitters. *Advanced Functional Materials* **2021**, *31* (1), 2005438, DOI: https://doi.org/10.1002/adfm.202005438
- 5. Conaghan, P. J.; Matthews, C. S. B.; Chotard, F.; Jones, S. T. E.; Greenham, N. C.; Bochmann, M.; Credgington, D.; Romanov, A. S., Highly Efficient Blue Organic Light-Emitting Diodes Based on Carbene-Metal-Amides. *Nature Communications* **2020**, *11* (1), 1758, DOI: 10.1038/s41467-020-15369-8
- 6. Romanov, A. S.; Becker, C. R.; James, C. E.; Di, D.; Credgington, D.; Linnolahti, M.; Bochmann, M., Copper and Gold Cyclic (Alkyl)(Amino)Carbene Complexes with Sub-Microsecond Photoemissions: Structure and Substituent Effects on Redox and Luminescent Properties. *Chemistry A European Journal* **2017**, *23* (19), 4625-4637, DOI: 10.1002/chem.201605891
- 7. Hamze, R.; Idris, M.; Muthiah Ravinson, D. S.; Jung, M. C.; Haiges, R.; Djurovich, P. I.; Thompson, M. E., Highly Efficient Deep Blue Luminescence of 2-Coordinate Coinage Metal Complexes Bearing Bulky Nhc Benzimidazolyl Carbene. *Frontiers in Chemistry* **2020**, *8*, DOI: 10.3389/fchem.2020.00401
- 8. Li, T.-y.; Muthiah Ravinson, D. S.; Haiges, R.; Djurovich, P. I.; Thompson, M. E., Enhancement of the Luminescent Efficiency in Carbene-Au(I)-Aryl Complexes by the Restriction of Renner-Teller Distortion and Bond Rotation. *Journal of the American Chemical Society* **2020**, *142* (13), 6158-6172, DOI: 10.1021/jacs.9b13755
- 9. Li, T.-y.; Shlian, D. G.; Djurovich, P. I.; Thompson, M. E., A Luminescent Two-Coordinate Aui Bimetallic Complex with a Tandem-Carbene Structure: A Molecular Design for the Enhancement of Tadf Radiative Decay Rate. *Chemistry A European Journal* **2021,** *27* (20), 6191-6197, DOI: https://doi.org/10.1002/chem.202100512

- 10. Ma, J.; Kapper, S. C.; Ponnekanti, A.; Schaab, J.; Djurovich, P. I.; Thompson, M. E., Dynamics of Rotation in Two-Coordinate Thiazolyl Copper(I) Carbazolyl Complexes. *Applied Organometallic Chemistry n/a* (n/a), e6728, DOI: https://doi.org/10.1002/aoc.6728
- 11. Muniz, C. N.; Schaab, J.; Razgoniaev, A.; Djurovich, P. I.; Thompson, M. E., Π-Extended Ligands in Two-Coordinate Coinage Metal Complexes. *Journal of the American Chemical Society* **2022**, *144* (39), 17916-17928, DOI: 10.1021/jacs.2c06948
- 12. Yang, J.-G.; Song, X.-F.; Wang, J.; Li, K.; Chang, X.; Tan, L.-Y.; Liu, C.-X.; Yu, F.-H.; Cui, G.; Cheng, G.; To, W.-P.; Yang, C.; Che, C.-M.; Chen, Y., Highly Efficient Thermally Activated Delayed Fluorescence from Pyrazine-Fused Carbene Au(I) Emitters. *Chemistry A European Journal* **2021**, *27* (71), 17834-17842, DOI: 10.1002/chem.202102969
- 13. Tang, R.; Xu, S.; Lam, T.-L.; Cheng, G.; Du, L.; Wan, Q.; Yang, J.; Hung, F.-F.; Low, K.-H.; Phillips, D. L.; Che, C.-M., Highly Robust Cui-Tadf Emitters for Vacuum-Deposited Oleds with Luminance up to 222 200 Cd M-2 and Device Lifetimes (Lt90) up to 1300 Hours at an Initial Luminance of 1000 Cd M-2. *Angewandte Chemie International Edition* **2022**, *61* (33), e202203982, DOI: 10.1002/anie.202203982
- 14. Chotard, F.; Sivchik, V.; Linnolahti, M.; Bochmann, M.; Romanov, A. S., Mono-Versus Bicyclic Carbene Metal Amide Photoemitters: Which Design Leads to the Best Performance? *Chemistry of Materials* **2020**, *32* (14), 6114-6122, DOI: 10.1021/acs.chemmater.0c01769
- 15. Romanov, A. S.; Jones, S. T. E.; Yang, L.; Conaghan, P. J.; Di, D.; Linnolahti, M.; Credgington, D.; Bochmann, M., Mononuclear Silver Complexes for Efficient Solution and Vacuum-Processed Oleds. *Advanced Optical Materials* **2018**, *6* (24), 1801347, DOI: doi:10.1002/adom.201801347
- 16. Conaghan, P. J.; Menke, S. M.; Romanov, A. S.; Jones, S. T. E.; Pearson, A. J.; Evans, E. W.; Bochmann, M.; Greenham, N. C.; Credgington, D., Efficient Vacuum-Processed Light-Emitting Diodes Based on Carbene–Metal–Amides. *Advanced Materials* **2018**, *30* (35), 1802285, DOI: 10.1002/adma.201802285
- 17. Romanov, A. S.; Jones, S. T. E.; Gu, Q.; Conaghan, P. J.; Drummond, B. H.; Feng, J.; Chotard, F.; Buizza, L.; Foley, M.; Linnolahti, M.; Credgington, D.; Bochmann, M., Carbene Metal Amide Photoemitters: Tailoring Conformationally Flexible Amides for Full Color Range Emissions Including White-Emitting Oled. *Chemical Science* **2020**, *11* (2), 435-446, DOI: 10.1039/C9SC04589A
- 18. Di, D.; Romanov, A. S.; Yang, L.; Richter, J. M.; Rivett, J. P. H.; Jones, S.; Thomas, T. H.; Jalebi, M. A.; Friend, R. H.; Linnolahti, M.; Bochmann, M.; Credgington, D., High-Performance Light-Emitting Diodes Based on Carbene-Metal-Amides. *Science* **2017**, *356* (6334), 159-163, DOI: doi:10.1126/science.aah4345
- 19. Hamze, R.; Peltier, J. L.; Sylvinson, D.; Jung, M.; Cardenas, J.; Haiges, R.; Soleilhavoup, M.; Jazzar, R.; Djurovich, P. I.; Bertrand, G.; Thompson, M. E., Eliminating Nonradiative Decay in Cu(I) Emitters:

- >99% Quantum Efficiency and Microsecond Lifetime. *Science* **2019**, *363* (6427), 601-606, DOI: doi:10.1126/science.aav2865
- 20. Kalyanasundaram, K., Photophysics, Photochemistry and Solar Energy Conversion with Tris(Bipyridyl)Ruthenium(Ii) and Its Analogues. *Coordination Chemistry Reviews* **1982**, *46*, 159-244, DOI: 10.1016/0010-8545(82)85003-0
- 21. Ravinson, D. S. M.; Thompson, M. E., Thermally Assisted Delayed Fluorescence (Tadf): Fluorescence Delayed Is Fluorescence Denied. *Materials Horizons* **2020**, *7* (5), 1210-1217, DOI: 10.1039/D0MH00276C
- 22. Li, T.-y.; Schaab, J.; Djurovich, P. I.; Thompson, M. E., Toward Rational Design of Tadf Two-Coordinate Coinage Metal Complexes: Understanding the Relationship between Natural Transition Orbital Overlap and Photophysical Properties. *Journal of Materials Chemistry C* **2022**, *10* (12), 4674-4683, DOI: 10.1039/d2tc00163b
- 23. Shen, W.; Li, J.; Zhang, C.; Shi, M.; Zhang, J., Copper, Silver and Sodium Salt-Mediated Quaternization by Arylation: Syntheses of N-Heterocyclic Carbene Precursors and 6-H-Phenanthridine Derivatives. *Chemistry An Asian Journal* **2016**, *11* (13), 1883-1886, DOI: https://doi.org/10.1002/asia.201600563
- 24. Khramov, D. M.; Boydston, A. J.; Bielawski, C. W., Synthesis and Study of Janus Bis(Carbene)S and Their Transition-Metal Complexes. *Angewandte Chemie International Edition* **2006**, *45* (37), 6186-6189, DOI: https://doi.org/10.1002/anie.200601583
- 25. Telfer, S. G.; McLean, T. M.; Waterland, M. R., Exciton Coupling in Coordination Compounds. *Dalton Transactions* **2011**, *40* (13), 3097-3108, DOI: 10.1039/c0dt01226b
- 26. Schinabeck, A.; Chen, J.; Kang, L.; Teng, T.; Homeier, H. H. H.; Suleymanova, A. F.; Shafikov, M. Z.; Yu, R.; Lu, C.-Z.; Yersin, H., Symmetry-Based Design Strategy for Unprecedentedly Fast Decaying Thermally Activated Delayed Fluorescence (Tadf). Application to Dinuclear Cu(I) Compounds. *Chemistry of Materials* **2019**, *31* (12), 4392-4404, DOI: 10.1021/acs.chemmater.9b00671
- 27. Sagara, Y.; Shizu, K.; Tanaka, H.; Miyazaki, H.; Goushi, K.; Kaji, H.; Adachi, C., Highly Efficient Thermally Activated Delayed Fluorescence Emitters with a Small Singlet–Triplet Energy Gap and Large Oscillator Strength. *Chemistry Letters* **2015**, *44* (3), 360-362, DOI: 10.1246/cl.141054
- 28. Shafikov, M. Z.; Martinscroft, R.; Hodgson, C.; Hayer, A.; Auch, A.; Kozhevnikov, V. N., Non-Stereogenic Dinuclear Ir(Iii) Complex with a Molecular Rack Design to Afford Efficient Thermally Enhanced Red Emission. *Inorganic Chemistry* **2021**, *60* (3), 1780-1789, DOI: 10.1021/acs.inorgchem.0c03251
- 29. Sworakowski, J.; Lipiński, J.; Janus, K., On the Reliability of Determination of Energies of Homo and Lumo Levels in Organic Semiconductors from Electrochemical Measurements. A Simple Picture Based on the Electrostatic Model. *Organic Electronics* **2016**, *33*, 300-310, DOI: 10.1016/j.orgel.2016.03.031

- 30. Marciniak, H.; Auerhammer, N.; Ricker, S.; Schmiedel, A.; Holzapfel, M.; Lambert, C., Reduction of the Fluorescence Transition Dipole Moment by Excitation Localization in a Vibronically Coupled Squaraine Dimer. *The Journal of Physical Chemistry C* **2019**, *123* (6), 3426-3432, DOI: 10.1021/acs.jpcc.8b11957
- 31. Reichardt, C., Solvatochromic Dyes as Solvent Polarity Indicators. *Chemical Reviews* **1994**, *94* (8), 2319-2358, DOI: 10.1021/cr00032a005
- 32. Shafikov, M. Z.; Zaytsev, A. V.; Kozhevnikov, V. N., Cyclometalation Geometry of the Bridging Ligand as a Tuning Tool for Photophysics of Dinuclear Ir(Iii) Complexes. *The Journal of Physical Chemistry C* **2021**, *125* (37), 20531-20537, DOI: 10.1021/acs.jpcc.1c05037
- 33. Shafikov, M. Z.; Pander, P.; Zaytsev, A. V.; Daniels, R.; Martinscroft, R.; Dias, F. B.; Williams, J. A. G.; Kozhevnikov, V. N., Extended Ligand Conjugation and Dinuclearity as a Route to Efficient Platinum-Based near-Infrared (Nir) Triplet Emitters and Solution-Processed Nir-Oleds. *Journal of Materials Chemistry C* **2021**, *9* (1), 127-135, DOI: 10.1039/D0TC04881J
- 34. Huang, F.; Liu, H.; Li, X.; Wang, S., Enhancing Hole Injection by Processing Ito through Moo3 and Self-Assembled Monolayer Hybrid Modification for Solution-Processed Hole Transport Layer-Free Oleds. *Chemical Engineering Journal* **2022**, *427*, 131356, DOI: https://doi.org/10.1016/j.cej.2021.131356
- 35. Brütting, W.; Frischeisen, J.; Schmidt, T. D.; Scholz, B. J.; Mayr, C., Device Efficiency of Organic Light-Emitting Diodes: Progress by Improved Light Outcoupling. *physica status solidi (a)* **2013**, *210* (1), 44-65, DOI: 10.1002/pssa.201228320
- 36. Romanov, A. S.; Yang, L.; Jones, S. T. E.; Di, D.; Morley, O. J.; Drummond, B. H.; Reponen, A. P. M.; Linnolahti, M.; Credgington, D.; Bochmann, M., Dendritic Carbene Metal Carbazole Complexes as Photoemitters for Fully Solution-Processed Oleds. *Chemistry of Materials* **2019**, *31* (10), 3613-3623, DOI: 10.1021/acs.chemmater.8b05112
- 37. Zhou, D.; Wu, S.; Cheng, G.; Che, C.-M., A Gold(Iii)—Tadf Emitter as a Sensitizer for High-Color-Purity and Efficient Deep-Blue Solution-Processed Oleds. *Journal of Materials Chemistry C* **2022**, *10* (12), 4590-4596, DOI: 10.1039/D1TC05487B
- 38. Teng, T.; Li, K.; Cheng, G.; Wang, Y.; Wang, J.; Li, J.; Zhou, C.; Liu, H.; Zou, T.; Xiong, J.; Wu, C.; Zhang, H.-X.; Che, C.-M.; Yang, C., Lighting Silver(I) Complexes for Solution-Processed Organic Light-Emitting Diodes and Biological Applications Via Thermally Activated Delayed Fluorescence. *Inorganic Chemistry* **2020**, *59* (17), 12122-12131, DOI: 10.1021/acs.inorgchem.0c01054

TOC



Supporting Information

for

Luminescent Binuclear Two-Coordinate Gold (I) Complexes Utilizing Janus Carbenes

Jie Ma^{1‡}, Jonas Schaab^{1‡}, Sritoma Paul², Stephen R. Forrest², Peter Djurovich¹, Mark E. Thompson^{1*}

¹Department of Chemistry, University of Southern California, Los Angeles, CA 90089 USA

¹Mork Family Department of Chemical Engineering and Materials Science, University of Southern California, Los Angeles, CA 90089 USA

²Department of Material Science and Engineering, University of Michigan, Ann Arbor, MI 48109, USA

[‡] These authors contributed equally

Table of Contents

Table of Contents	2
Equations	5
General Synthesis	6
Synthesis _{Cl} Au ^{BAZ} Au _{Cl}	7
Synthesis _{Cz} Au ^{BAZ} Au _{Cz}	7
Synthesis BCzAuBAZAuBCz	8
Synthesis _{Bim} Au ^{BAZ} Au _{Bim}	8
Synthesis BBI ligand	9
Synthesis _{Cl} Au ^{BBI} Au _{Cl}	10
Synthesis BCzAuBBIAuBCz	10
Synthesis BZIAuBCz	11
Solubility of Binuclear Complexes	12
Table S1: Solubility of binuclear complexes in various organic solvents.	12
Single Crystal X-ray Structures	13
Table S2a: Selected bond lengths and angles for the(carbene)M(amide) complexes	13
Table S2b: Crystallographic parameters for BCzAuBZAC and BZIAuBCz	14
Table S2c: Crystallographic parameters for BCzAuBZAC and BZIAuBCz	15
Figure S1: Thermal ellipsoid drawings of (a) $_{BCz}Au^{BAZ}Au_{BCz}$, (b) $_{Cz}Au^{BAZ}Au_{Cz}$ and (c) $_{Bim}Au^{BAZ}$ (50% probability)	Au _{Bim}
Figure S2: Thermal ellipsoid drawings of (left) BZIAuBCz and (right) BCzAuBZAC (50% probability)	17
Theoretical Modeling	18
Figure S3a. The NTOs for wavefunctions of CzAuBZI' (left) and CzAuBBI'AuCz (right).	18
Figure S3b. The NTOs for wavefunctions of CzAuBZAC' (left) and CzAuBAZ'AuCz (right).	19
Figure S3c. The NTOs for wavefunctions of bimAuBZAC' (left) and bimAuBAZ'Aubim (right).	20
Table S3: HOMO-1/HOMO/LUMO/LUMO+X images of all cMa complexes.	21
Table S4. Energies of the frontier orbitals and excited states for the cMa complexes	22
Table S5. Compositions of the excited states for the cMa complexes.	23
Table S6. Dipole moments of the ground and excited states.	24
Table S7. Transition dipole moments of the excited states.	25
Figure 4a. Calculated S_1 , S_2 (with oscillator strength) and T_1 , T_2 energies of $_{Cz}Au^{BBI}Au_{Cz}$ (left) and BZ (right) with respect to their dihedral angles α	ZIAu _{Cz} 26
Figure 4b. Calculated S_1 , S_2 (with oscillator strength) and T_1 , T_2 energies of ${}_{Cz}Au^{BAZ}Au_{Cz}$ (left ${}^{BZAC}Au_{Cz}$ (right) with respect to their dihedral angles α	t) and 27

Figure 4c. Calculated S_1 , S_2 (with oscillator strength) and T_1 , T_2 energies of $_{bim}Au^{BAZ}Au_b$ $^{BZAC}Au_{bim}$ (right) with respect to their dihedral angles α	im (left) and 28
Table S8. h ⁺ ,e ⁻ separation distances for cMa complexes	29
Table S9. Center of h+,e- for S1 NTOs for cMa complexes.	30
Electrochemistry	31
Figure S5. CV (black) and DPV (red: oxidation, blue: reduction) traces of complexes	32
Photophysical measurements	33
Figure S6. Integration of the low energy half of the CT-Band for BCz and bim complexes in	Tol. 34
Figure S7. Absorption spectrum of CIAuBAZAUCI in MeCy.	35
Figure S8. Emission of all BCz mono and dinuclear complexes in PS.	35
Table S10: Integrated Area of the CT Band in Toluene from Figure S5.	36
Figure S9(a-d): Solvent dependent Absorption and Emission spectra for BCzAuBAZAuBCz, BCz-	Au ^{BAZ} 37
Figure S9(f-i): Solvent dependent Absorption and Emission spectra for BCzAuBBIAuBCz, BCzA	u ^{BZ} 38
Figure S9(l-o): Solvent dependent Absorption and Emission spectra for BimAuBAZAuBim, BimA	Au ^{BAZ} 39
Figure S10. Emission spectra in PS, MeTHF and Me-Cyclo-Hexane at RT and 77K	40
Table S11: Photophysical Data for all BCz and bim compounds in MeCy, 2MeTHF, MeCN	and CH ₂ Cl ₂ 41
Figure S11. ET30 plots and linear fits for all complexes.	42
Table S12. The value of solvatochromic shift from MeCN to MeCy	43
Table S13. Photophysical Data for $_{\text{Cz}}\text{Au}^{\text{BAZ}}\text{Au}_{\text{Cz}}$ based compounds in MeCy, 2MeTHF, CH_2Cl_2	MeCN and 43
Figure S12. Absorption and Emission Spectra of _{Cz} Au ^{BAZ} Au _{Cz}	44
Temperature Dependent Lifetime Measurements	45
Figure S13: Temperature dependent lifetime for _{BCz} Au ^{BAZC} Au _{BCz} in PS.	46
Figure S14: Temperature dependent lifetime for _{BCz} Au ^{BZAC} in PS.	47
Figure S15: Temperature dependent lifetime for _{BCz} Au ^{BBI} Au _{BCz} in PS.	48
Figure S16: Temperature dependent lifetime for _{Bim} Au ^{BAZC} Au _{Bim} in PS.	49
Figure S17: Temperature dependent emission for _{BZIAuBCz} in PS.	50
OLED Device Studies	51
Figure S18. OLED Devices with 20% BCzAuBBIAuBCz in TCTA as host material.	52
Table S14: Photoluminenscence data of dinuclear complexes in different host materials.	53
Figure S19. Doping concentration-controlled OLED devices with BCzAuBBIAuBCz and C material	zSi as host 54
NMR spectra	55
Figure S20. ¹ H and ¹³ C spectra for BBI-Ligand 1 st step in CDCl ₃	55
Figure S21. ¹ H and ¹³ C spectra for BBI-Ligand 2 nd step in CDCl ₃	56

Figure S22. ¹ H and ¹³ C spectra for BBI-Ligand 3 rd step in CDCl ₃	57
Figure S23. ¹ H spectra for _{Cl} Au ^{BAZ} Au ^{Cl} in acetone-d6	58
Figure S24. ¹ H and ¹³ C spectra for _{Cz} Au ^{BAZ} Au _{Cz} in acetone-d6	59
Figure S25. ¹ H and ¹³ C spectra for _{BCz} Au ^{BAZ} Au _{BCz} in acetone-d6	60
Figure S26. ¹ H and ¹³ C spectra for _{Bim} Au ^{BAZ} Au _{Bim} in acetone-d6	61
Figure S27. ¹ H and ¹³ C spectra for _{BCz} Au ^{BBI} Au _{BCz} in acetone-d6	62
Figure S28. ¹ H and ¹³ C spectra for _{BZIAuBCz} in acetone-d6	63
References	64

Equations

$$\Delta E_{ST} = 2K = 2 \iint f_h(r_1) f_e(r_2) \frac{1}{|r_2 - r_1|} f_h(r_1) f_e(r_2) d_{r_1} d_{r_2} \#eq.S1$$

where r_1 and r_2 denote the coordinates of a hole and an electron of NTO of the excited states.

$$k_{S1} \propto \left(\mu_{S_0}^{S_1}\right)^2 = |\langle f_H(r) | r | f_L(r) \rangle|^2 = \left| \int f_H(r) r f_L(r) d_r \right|^2 \#eq.S2$$

r denotes the coordinate of shared electrons between a hole and an electron of NTO and operator r is coupling operator of S_0 and S_1 state.

General Synthesis

All commercial reagents were purchased from Sigma-Aldrich except for 2-chloroaniline (Acros Organics) and tri-tert-butylphosphonium tetrafluoroborate (Strem Chemicals). All were used without further purification and all reaction were performed under a N_2 atmosphere unless otherwise noted. All NMR analyses were performed using a Varian 400, Varian 500, or Varian 600 NMR spectrometer and referenced to the residual proton signal of the deuterated solvent unless otherwise noted. Elemental analyses were performed using a Thermo Scientific FlashSmart CHNS elemental analyzer.

Synthesis _{Cl}Au^{BAZ}Au_{Cl}

The BAZ Ligand was synthesized according to Literature. To a 100 mL Schlenk flask with bubble degassed dry THF (45 mL) 500 mg (0.444 mmol, 1.0 eq) BAZ-Ligand was added and cooled to -78C. 1.86 mL (0.931 mmol, 2.1 eq) 0.5M KHMDS THF solution was added dropwise over 20 min. After 2 h stirring at -78C Au(Me₂S)Cl (287 mg, 0.976 mmol, 2.2 eq) was added and reaction was slowly warmed up to room temperature overnight. Reaction was worked up by filtration through Celite, washing with dichloromethane and solvent removal. Product was precipitated from dichloromethane by adding hexanes, yielding to the off-white $_{Cl}Au^{BZAC}Au_{Cl}$ in 86% yield (495 mg, 0.383 mmol). H NMR (400 MHz, acetone-d6) δ 7.54 – 7.49 (m, 2H), 7.44 – 7.36 (m, 6H), 7.33 – 7.27 (m, 4H), 6.46 (s, 2H), 4.89 (s, 4H), 3.24 (p, J = 6.7 Hz, 4H), 3.10 (p, J = 6.9 Hz, 4H), 1.39 (dd, J = 10.9, 6.8 Hz, 24H), 1.25 (d, J = 6.8 Hz, 12H), 1.16 (d, J = 6.8 Hz, 12H).

Synthesis _{Cz}Au^{BAZ}Au_{Cz}

dipp = 2,6-diisopropyl phenyl

To a 50 mL Schlenkflask with bubble degassed dry THF (25 mL) 54 mg (0.325 mmol, 2.1 eq) 1H-carbazole ligand was added. 0.159 mL (0.317 mmol, 2.05 eq) 2M sodium *tert*-butoxide (NaOtBu) THF solution was added dropwise. After 1 h stirring at ambient temperature, $_{Cl}Au^{BZAC}Au_{Cl}$ (200 mg, 0.155 mmol, 1.0 eq) was added and reaction was stirred overnight. Reaction was worked up by filtration through Celite, washing with dichloromethane and solvent removal. Product was precipitated from dichloromethane by adding hexanes. Solid was filtered and washed with diethyl ether, yielding to the colorless $_{Cz}Au^{BZAC}Au_{Cz}$ in 80% yield (192 mg, 0.124 mmol). Under a UV light the solid is blue emissive. H NMR (400 MHz, acetone-d6) δ 7.86 – 7.66 (m, 8H), 7.60 (d, J = 7.8 Hz, 4H), 7.51 (d, J = 7.8 Hz, 4H), 6.89 (ddd, J = 8.3, 7.0, 1.3 Hz, 4H), 6.74 (ddd, J = 7.8, 7.0, 1.1 Hz, 4H), 6.61 (s, 2H), 6.08 (dt, J = 8.2, 0.9 Hz, 4H), 5.03 (s, 4H), 3.41 (hept, J = 7.7 Hz, 4H), 3.33 – 3.20 (m, 4H), 1.37 (d, J = 6.8 Hz, 12H), 1.33 (t, J = 6.8 Hz, 24H), 1.24 (d, J = 6.9 Hz, 12H). CHN: C: 62.74%, H: 5.98%, N: 5.28%; calculated: C: 63.39%; H: 5.84%; N: 5.41%

Yield 80%

Synthesis BCzAuBAZAuBCz

dipp = 2,6-diisopropyl phenyl

Yield 72%

To a 50 mL Schlenk flask with bubble degassed dry THF (25 mL) 90 mg (0.325 mmol, 2.1 eq) 3,6-Di-tert-butylcarbazole ligand was added. 0.158 mL (0.317 mmol, 2.05 eq) 2M sodium *tert*-butoxide (NaOtBu) solution was added dropwise. After 1 h stirring at ambient temperature, $_{Cl}$ Au BAZ Au $_{Cl}$ (200 mg, 0.155 mmol, 1.0 eq) was added and reaction was stirred overnight. Reaction was worked up by filtration through Celite, washing with dichloromethane and solvent removal. Product was washed with -40C hexanes and collected the precipitations. Then repeat this step three times, yielding to the yellow powder $_{BCz}$ Au BAZ Au $_{BCz}$ in 72% yield (198 mg, 0.111 mmol). Under a UV light the solid is skyblue emissive. 1 H NMR (400 MHz, acetone-d6) δ 7.88 – 7.80 (m, 6H), 7.72 (t, J = 7.8 Hz, 2H), 7.62 (d, J = 7.8 Hz, 4H), 7.53 (d, J = 7.8 Hz, 4H), 7.00 (dd, J = 8.6, 2.0 Hz, 4H), 6.61 (s, 2H), 6.04 (dd, J = 8.6, 0.6 Hz, 4H), 5.03 (s, 4H), 3.41 (sept, J = 7.0 Hz, 4H), 3.27 (sept, J = 6.5 Hz, 4H), 1.40 (d, J = 6.9 Hz, 36H), 1.38 – 1.31 (m, 60H), 1.26 (d, J = 6.8 Hz, 12H). 13 C NMR (100 MHz, acetone-d6) δ 229.2, 228.3, 227.8, 223.4, 223.1, 219.3, 219.2, 214.2, 211.5, 210.0, 208.8, 205.2, 202.6, 201.1, 195.5, 194.4, 192.4, 191.0, 190.1, 189.7, 185.9, 182.5, 180.6, 177.9, 177.3, 173.7, 173.6, 166.6, 164.9, 162.8, 153.1, 148.3, 148.1, 146.8, 145.7, 145.3, 137.6, 125.5, 125.3, 123.4, 120.4, 118.7, 114.5, 113.4, 38.4, 38.1, 37.8, 37.4, 34.0, 31.7, 24.0, 24.0, 23.6. CHN: C: 65.32%, H: 6.55%, N: 4.93%; calculated: C: 66.20%; H: 6.92%; N: 4.73%

Synthesis Rim Au^{BAZ}Au_{Rim}

dipp = 2,6-diisopropyl phenyl

Yield 76%

The bim ligand was synthesized according to Literature.² To a 50 mL Schlenk flask with bubble degassed dry THF (25 mL) 61 mg (0.293 mmol, 2.1 eq) 1H-Bim ligand was added. 0.143 mL (0.286 mmol, 2.05 eq) 2M sodium *tert*-butoxide (NaOtBu) THF solution was added dropwise. After 1 h stirring at ambient temperature, $_{Cl}Au^{BAZ}Au_{Cl}$ (180 mg, 0.139 mmol, 1.0 eq) was added and reaction was stirred overnight. Reaction was worked up by filtration through Celite, washing with dichloromethane and solvent removal. Product was precipitated from dichloromethane by adding hexanes. Solid was filtered and washed with diethyl ether, yielding to the off-white $_{Bim}Au^{BAZ}Au_{Bim}$ in 76% yield (174 mg, 0.107 mmol). Under a UV light the solid is blue emissive. ^{1}H NMR (400 MHz, acetone-d6) δ 7.70 – 7.57 (m, 6H), 7.57 – 7.48 (m, 4H), 7.46 – 7.39 (m, 4H), 7.30 (ddd, J = 8.0, 1.2, 0.6 Hz, 2H), 7.06 (ddd, J = 8.0, 7.3, 1.2 Hz, 2H), 6.96 –

6.84 (m, 8H), 6.61 (s, 2H), 6.27 – 6.18 (m, 2H), 5.05 (s, 4H), 3.41 (sept, J = 6.8 Hz, 4H), 3.27 (sept, J = 6.5 Hz, 4H), 1.48 (dd, J = 14.2, 6.8 Hz, 24H), 1.32 (d, J = 6.9 Hz, 12H), 1.25 (d, J = 6.8 Hz, 12H). ¹³C NMR (100 MHz, acetone-d6) δ 146.5, 145.1, 145.0, 136.7, 130.6, 129.8, 127.2, 127.1, 126.7, 126.5, 126.1, 126.0, 125.5, 125.2, 121.0, 120.9, 118.8, 118.5, 117.4, 116.7, 115.1, 113.2, 109.0, 108.8, 24.1, 23.7. CHN: C: 42.83%, H: 2.06%, N: 14.31%; calculated: C: 43.74%; H: 2.24%; N: 14.17%

Synthesis BBI ligand

$$\begin{array}{c|c} O_2N & & & & \\ O_2N & & & & \\ CI & & & & \\ \end{array}$$

In a 500-mL two-neck flask containing a stir bar and 5.0 g (21.1 mmol) of the dichlorodinitrobenzene was equipped with a water-condenser. The system was pumped down and backfilled with nitrogen gas for three cycles. Nitrogen-degassed 2,6-diisopropoylaniline (23.9 mL, 126.6 mmol) was cannula-transferred into the reaction flask. The mixture was heated at 150°C for 48 hours after which it was allowed to cool down to room temperature. Methanol (~20 mL) was added, and the flask was placed in a freezer (-40°C) to encourage precipitation. The precipitate was collected by vacuum filtration and washed with cold methanol and dried under vacuum to yield 8.5 g (78%) of a yellow powder. ¹H NMR (400 MHz, Chloroform-d) δ = 9.43 (s, 2H), 9.39 (s, 1H), 7.23 (t, J = 7.8 Hz, 2H), 7.04 (d, J = 7.8 Hz, 4H), 5.09 (s, 1H), 2.75 (hept, J = 6.8 Hz, 4H), 1.07 (d, J = 6.8 Hz, 12H), 0.85 (d, J = 6.9 Hz, 12H). ¹³C NMR (101 MHz, Chloroform-d) δ = 149.35, 146.30, 132.03, 129.66, 129.03, 125.15,124.08, 94.82, 28.73, 24.93, 22.37.

A 500-mL round-bottom flask was charged with a magnetic stir-bar and formic acid (98%)/water mixture (90:10 mL). NaHCO₃ (9.72 g, 115.7 mmol) was added portion-wise with vigorous stirring. To the mixture was added Pd/C (0.616 g, 10 wt %, 0.578 mmol Pd) and dinitroarene (3.0 g, 5.78 mmol). The flask was fitted with a water condenser and heated in an oil bath with vigorous stirring at 120°C for 48 h. The mixture was then allowed to cool to room temperature and filtered through a plug of celite with the aid of 70 mL of Ethyl acetate. On a rotary evaporator, the filtrate volume was reduced to a slurry mixture. 50 mL of deionized water was added into the mixture, swirled, and slowly poured into a vigorously stirring solution of saturated aqueous K_2CO_3 . A beige precipitate developed and was collected via vacuum filtration, rinsed with plenty of water H_2O and dried under vacuum to yield 2.73 g (98%). 1H NMR (400 MHz, Chloroform-d): $\delta = 8.39$ (s, 1H), 7.87 (s, 2H), 7.47 (t, J = 7.8 Hz, 2H), 7.27 (d, J = 7.9 Hz, 4H), 6.52 (s, 1H), 2.26 (hept, J = 6.7 Hz, 4H), 1.06 (dd, J = 6.9, 0.7 Hz, 12H), 0.90 (dd, J = 6.8, 0.7 Hz, 12H). ^{13}C NMR (101 MHz, CDCl3) δ 147.95, 144.81, 140.84, 134.61, 130.99, 130.49, 124.38, 110.63, 89.89, 28.41, 24.88, 23.95.

In a 100-mL pressure flask, benzobis(imidazole) (500 mg, 1.04 mmol), 2-iodomethane (0.52 mL, 8.36 mmol), and acetonitrile (5 mL) were added. The pressure flask was sealed and heated at 90°C for 24 hours.

After the completion of the reaction, the mixture was cooled down to room temperature and solvents were removed under reduced pressure. Diethyl ether was added to the resulting crude solid, which was sonicated for 10 min, and collected by vacuum filtration to yield a beige solid (680 mg, 85%). 1 H NMR (400 MHz, Acetone-d6) δ = 10.73 (s, 2H), 9.91 (s, 1H), 8.24 (s, 1H), 7.63 (t, 2H), 7.45(d, J = 7.9 Hz, 4H), 4.73 (s, 6H), 2.45 (hept, J = 6.8 Hz, 4H), 1.14 (d, J = 6.8 Hz, 12H), 1.00 (d, J = 6.8 Hz,12H). 13 C NMR (101 MHz, acetone) δ 146.89, 146.78, 133.35, 132.32, 127.59, 125.10, 102.47, 98.68, 36.23, 24.25, 23.15, -2.00

Synthesis _{Cl}Au^{BBI}Au_{Cl}

dipp = 2,6-diisopropyl phenyl

To a 100 mL Schlenk flask with bubble degassed dry THF (35 mL) 400 mg (0.496 mmol, 1.0 eq) BBI-Ligand was added. 1.49 mL (1.04 mmol, 2.1 eq) 0.7M KHMDS THF solution was added dropwise. After 1h stirring at room temperature Au(Me₂S)Cl (321 mg, 1.09 mmol, 2.2 eq) was added and reaction was stirred overnight. Reaction was worked up by filtration through Celite, washing with dichloromethane and solvent removal. Product was precipitated from dichloromethane by adding hexanes. Solid was filtered and washed with methanol, yielding to the off-white $_{Cl}Au^{BBI}Au_{Cl}$ in 72% yield (348 mg, 0.358 mmol). ^{1}H NMR (400 MHz, acetone-d6) δ 8.52 (s, 1H), 7.51 (t, 2H), 7.36 (d, J = 7.8 Hz, 4H), 6.87 (s, 1H), 4.37 (s, 6H), 2.27 (sept, J = 6.5 Hz, 4H), 1.22 (d, J = 6.8 Hz, 12H), 0.94 (d, J = 6.9 Hz, 12H).

Synthesis BCzAuBBIAuBCz

dipp = 2,6-diisopropyl phenyl

To a 25 mL Schlenk flask with bubble degassed dry THF (10 mL) 120 mg (0.432 mmol, 2.1 eq) 3,6-Ditert-butylcarbazole ligand was added. 0.211 mL (0.422 mmol, 2.05 eq) 2M sodium *tert*-butoxide (NaOtBu) solution was added dropwise. After 1 h stirring at ambient temperature, $_{Cl}Au^{BBl}Au_{Cl}$ (200 mg, 0.206 mmol, 1.0 eq) was added and reaction was stirred overnight. Reaction was worked up by filtration through Celite, washing with dichloromethane and solvent removal. Product was purified by addition of Hexanes, sonicating 30 min, cooling the flask slowly in a Dewar to -40C in a deep freezer. Solid was collected at low temperature. The purification step was repeated if unreacted BCz was detected by NMR. The bright yellow solid $_{BCz}Au^{BBl}Au_{BCz}$ was obtained in 73% yield (219 mg, 0.150 mmol). Under a UV light the solid is green emissive. ^{1}H NMR (600 MHz, acetone-d6) δ 8.65 (d, J = 0.8 Hz, 1H), 8.00 (dd, J = 2.0, 0.7 Hz, 4H), 7.71 (t, J = 8.0 Hz, 2H), 7.52 (d, J = 8.0 Hz, 4H), 7.20 (dd, J = 8.5, 2.0 Hz, 4H), 7.13 – 7.10 (m, 5H), 4.62 (s, 6H), 2.76 (s, 2H), 2.48 (sept, J = 6.6 Hz, 4H), 1.42 (d, J = 6.6 Hz, 4H), 1.38 (s, 35H), 1.30 (d, J = 6.8 Hz,

12H), 1.04 (d, J = 6.9 Hz, 12H). ¹³C NMR (151 MHz, acetone-d6) δ 148.1, 147.1, 138.1, 134.0, 132.6, 131.8, 131.1, 124.8, 123.9, 121.1, 114.9, 113.0, 110.0, 109.6, 36.3, 35.6, 34.1, 31.7, 31.5, 24.1, 23.6. CHN: C: 62.08%, H: 6.17, N: 6.44%, calculated: C: 61.17%; H: 6.58%; N: 5.49% (includes 1 THF)

Synthesis BZIAu_{BC}

BZI Au_{Cl} Ligand was synthesized according to Literature.³ To a 25 mL Schlenk flask with bubble degassed dry THF (10 mL) 83 mg (0.297 mmol, 1.05 eq) 3,6-Di-tert-butylcarbazole ligand was added. 0.149 mL (0.297 mmol, 1.05 eq) 2M sodium *tert*-butoxide (NaOtBu) solution was added dropwise. After 1 h stirring at ambient temperature, ^{BZI}Au_{Cl} (190 mg, 0.283 mmol, 1.0 eq) was added and reaction was stirred overnight. Reaction was worked up by filtration through Celite, washing with dichloromethane and solvent removal. Product was precipitated from dichloromethane by adding hexanes. Solid was filtered and washed with diethyl ether, yielding to the colorless ^{BZI}Au_{BCz} in 82% yield (212 mg, 0.232 mmol). Under a UV light the solid is blue emissive. ¹H NMR (400 MHz, acetone-d6) δ 7.92 (dd, J = 2.1, 0.7 Hz, 2H), 7.87 – 7.78 (m, 2H), 7.68 – 7.58 (m, 6H), 7.43 (dd, J = 6.1, 3.2 Hz, 2H), 7.07 (dd, J = 8.5, 2.0 Hz, 2H), 6.69 (dd, J = 8.5, 0.6 Hz, 2H), 2.63 (sept, J = 6.8 Hz, 4H), 1.39 (d, J = 6.9 Hz, 12H), 1.34 (s, 18H), 1.19 (d, J = 6.9 Hz, 12H). ¹³C NMR (100 MHz, acetone-d6) δ 148.0, 146.9, 137.9, 134.9, 131.7, 131.1, 125.8, 124.7, 123.7, 120.9, 114.8, 112.8, 112.1, 34.0, 31.7, 31.4, 24.0, 23.3. CHN: C: 67.20%, H: 6.95%, N: 5.10%, calculated: C: 67.02%; H: 6.84%; N: 4.60%

Solubility of Binuclear Complexes

Table S1: Solubility of binuclear complexes in various organic solvents.

Solvents	MeCN	DMSO	DMF	Acetone	DCM	THF	Toluene	Hex	MeCy
$_{Cz}Au^{BAZ}Au_{Cz}$	insol	insol	insol	sol	sol	sol	sl sol	insol	insol
$_{BCz}Au^{BAZ}Au_{BCz}$	insol	insol	insol	sol	sol	sol	sol	sl sol	sl sol
$_{BCz}Au^{BBI}Au_{BCz}$	sl sol	sl sol	sol	sol	sol	sol	sol	sol	sol
$_{bim}Au^{BAZ}Au_{bim}$	insol	insol	insol	sol	sol	sol	sol	sl sol	sl sol

sol indicates soluble > 1g/100 ml; sl sol indicates slightly soluble (0.1 to 1) g/100ml; insol indicates insoluble < 0.1 g/100 ml

Single Crystal X-ray Structures

All crystals were grown by recrystallization. Vapor diffusion of hexanes or pentane into a solution of the compound in dichloromethane. A Cryo-Loop was used to mount the sample with Paratone oil.

All single crystal structures were determined at 100K with Rigaku Xta LAB Synergy S, equipped with an HyPix-600HE detector and an Oxford Cryostream 800 low Temperature unit, using Cu K_{α} PhotonJet-S X-ray source. The frames were integrated using the SAINT algorithm to give the hkl files. Data were corrected for absorption effects using the multi-scan method (SADABS) with Rigaku CrysalisPro. The structures were solved by intrinsic phasing and refined with the SHELXTL Software Package.⁴ If necessary, the disordered solvent treatment method BYPASS for co-crystalizing solvent molecules, was implemented and marked in the CCDC entry.

All cif files and report data including atom position, bond lengths and bond angle can be downloaded from the CCDC database, using the database number in the right column of the following table. Furthermore, the following table is giving the most important bond lengths, angles and the torsion angle around the metal center.

Table S2a: Selected	l bond lengths and	l angles for the	(carbene)M	((amide) complexes
Tubic Dau. Deiceicu	i oona iengins ana	i ungios joi inc	(Car oche) IVI	(annual) complexes.

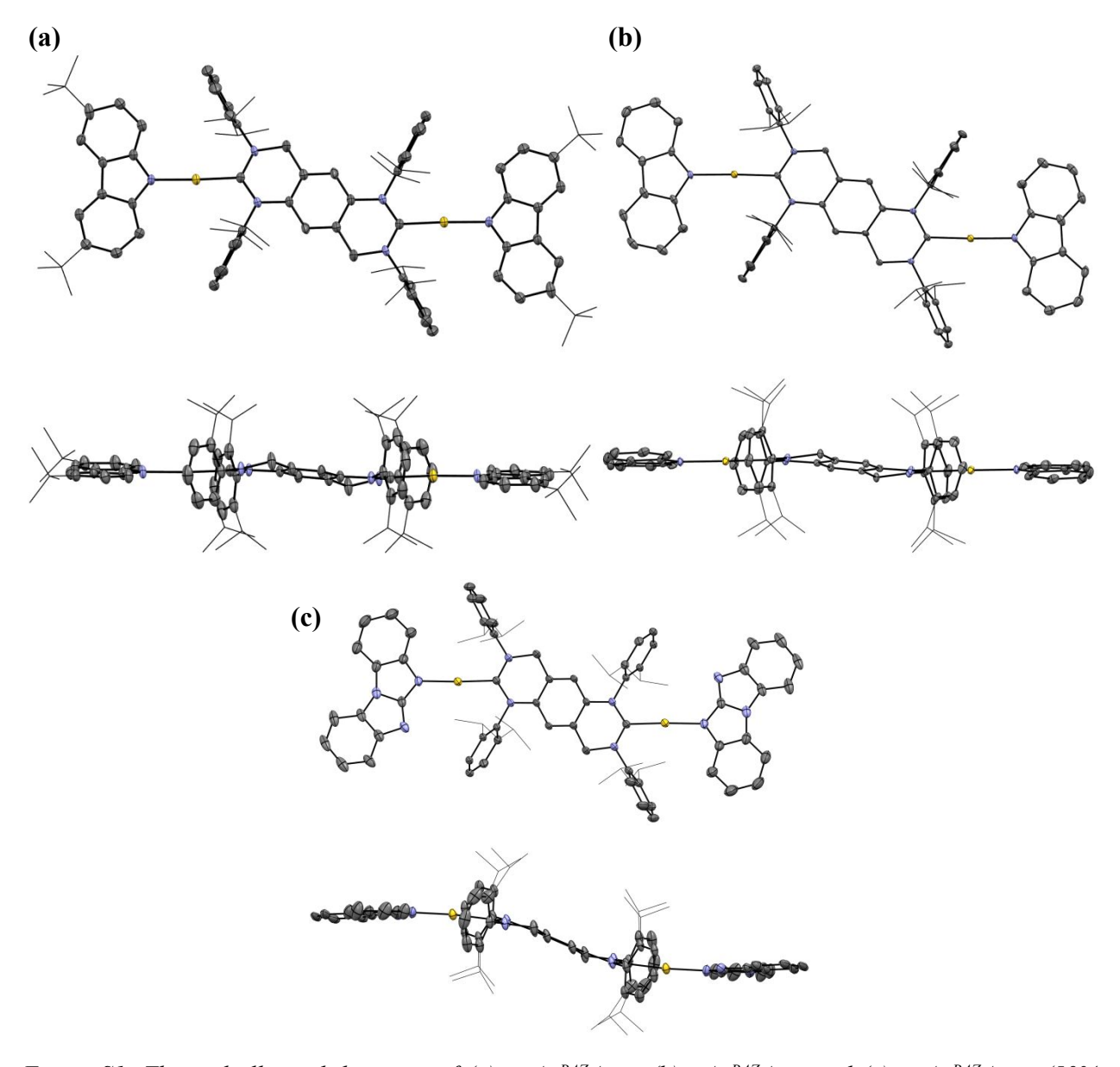
Compound	C-M (Å)	M-N (Å)	C-M-N (°)	Dihedral angel (°) NC-M-NC
$_{\mathrm{BCz}}\mathrm{Au^{BAZ}Au_{BCz}}$	1.989(4)	2.007(4)	177.0(2)	5.5
$^{\mathrm{BZAC}}\!\mathrm{Au}_{\mathrm{BCz}}$	2.009(4)	2.013(4)	176.8(2)	0.6
$_{\mathrm{Cz}}\mathrm{Au^{\mathrm{BAZ}}\mathrm{Au_{\mathrm{Cz}}}}$	1.995(9)	2.020(7)	177.9(3)	0.6
$_{Bim}Au^{BAZ}Au_{Bim}$	1.993(4)	2.017(3)	175.4(2)	5.4
$^{\mathrm{BZI}}\mathrm{Au}_{\mathrm{BCz}}$	1.995(5)	2.027(4)	175.6(2)	10.4

<u>Table S2b:</u> Crystallographic parameters for $C_zAu^{BAZ}Au_{Cz}$, $BC_zAu^{BAZ}Au_{BCz}$ and $B_{lim}Au^{BAZ}Au_{Blim}$

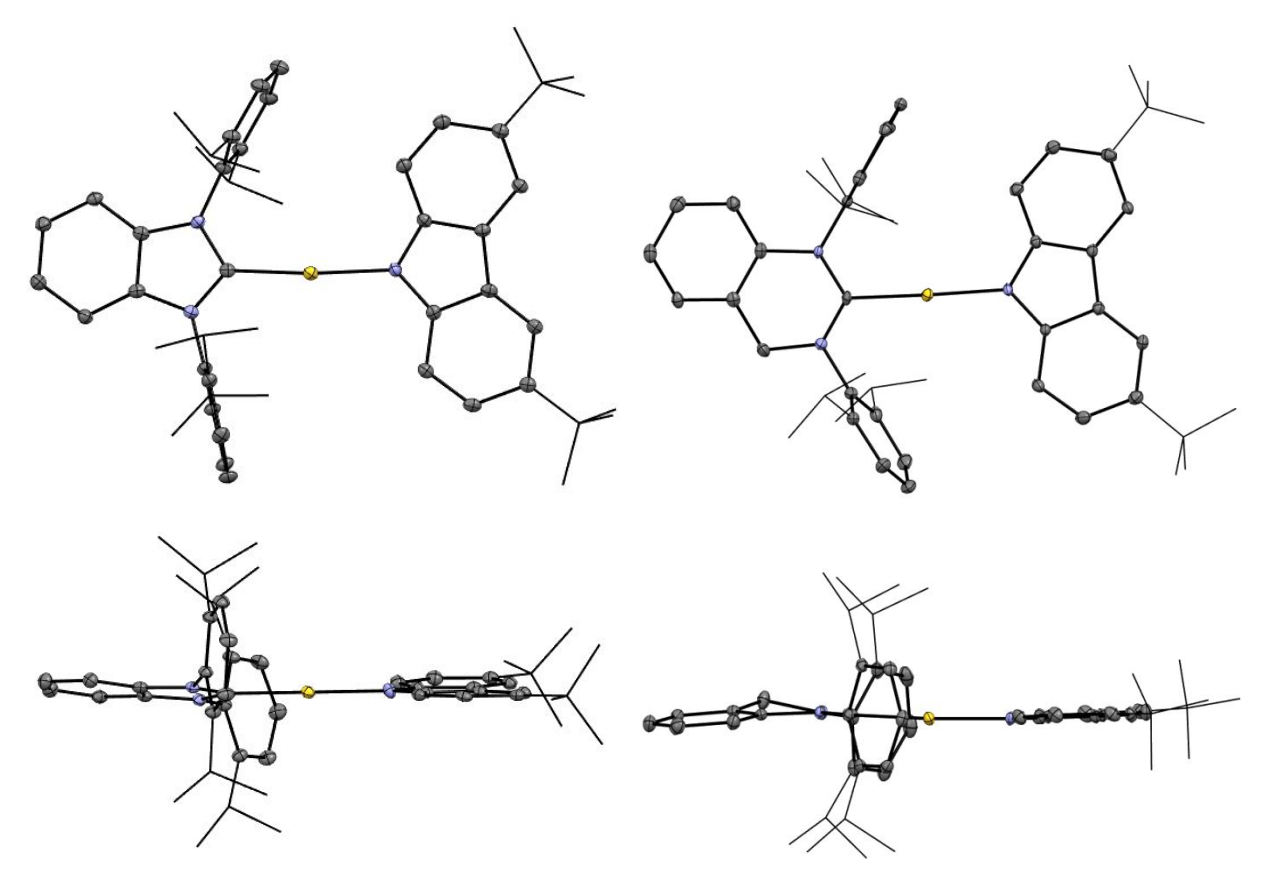
Identification code	_{Cz} Au ^{BAZ} Au _{Cz}	$\frac{\mathcal{A}u_{BCz}u_{B}u_{Bim}\mathcal{A}u}{\mathcal{B}Cz}\mathcal{A}\mathbf{u}_{BCz}$	BimAuBAZAuBim
Empirical formula	$C_{82}H_{90}Au_2N_6*2CH_2Cl_2$	$C_{98}H_{122}Au_2N_6$	$C_{84}H_{90}Au_2N_{10}$
Formula weight	1723.38	1777.94	1633.59
Temperature/K	100.15	101(2)	100(3)
Crystal system	triclinic	triclinic	trigonal
Space group	P-1	P-1	R-3c
a/Å	11.5434(2)	12.30230(10)	40.4469(3)
b/Å	13.6791(2)	14.2635(2)	40.4469(3)
c/Å	14.4472(2)	14.6554(2)	28.7613(2)
α/°	105.3850(10)	70.9900(10)	90
β/°	109.6430(10)	76.1300(10)	90
γ/°	108.0810(10)	71.3180(10)	120
Volume/Å ³	1860.21(5)	2276.82(5)	40748.3(7)
Z	1	1	18
$\rho_{calc}g/cm^3$	1.538	1.297	1.198
μ/mm ⁻¹	9.000	6.313	6.323
F(000)	866.0	910.0	14796.0
Crystal size/mm ³	$0.149 \times 0.064 \times 0.036$	$0.309 \times 0.089 \times 0.077$	$0.181 \times 0.168 \times 0.064$
Radiation	$CuK\alpha (\lambda = 1.54184)$	Cu K α ($\lambda = 1.54184$)	Cu K α ($\lambda = 1.54184$)
2Θ range for data collection/°	7.134 to 160.942	6.454 to 160.62	6.644 to 163.324
Index ranges	$-12 \le h \le 14, -17 \le k \le 17,$ $-18 \le l \le 18$	$-15 \le h \le 15, -18 \le k \le 18,$ $-18 \le l \le 18$	$-51 \le h \le 50, -50 \le k \le 45,$ $-36 \le l \le 35$
Reflections collected	55772	142760	157374
Independent reflections	$8071 [R_{int} = 0.1057, R_{sigma} = 0.0529]$	$9862 [R_{int} = 0.0873, R_{sigma} = 0.0276]$	9903 [$R_{int} = 0.0474$, $R_{sigma} = 0.0136$]
Data/restraints/parameters	8071/0/426	9862/0/523	9903/0/441
Goodness-of-fit on F ²	1.096	1.095	1.037
Final R indexes [I>=2σ (I)]	$R_1 = 0.0714, wR_2 = 0.1810$	$R_1 = 0.0441, WR_2 = 0.1127$	$R_1 = 0.0379, wR_2 = 0.1060$
Final R indexes [all data]	$R_1 = 0.0755$, $wR_2 = 0.1833$	$R_1 = 0.0479$, $wR_2 = 0.1157$	$R_1 = 0.0424, wR_2 = 0.1113$
Largest diff. peak/hole / e Å-3	1.98/-2.73	3.50/-2.44	0.98/-0.89
#CCDC	2206141	2233511	2206146

<u>Table S2c:</u> Crystallographic parameters for $^{BZAC}Au_{BCz}$ and $^{BZI}Au_{BCz}$

Identification code	BZACAu _{BCz} unu	BZIAu _{BCz}
Empirical formula	$C_{52}H_{64}AuN_3 * C_3H_6O$	$C_{51}H_{62}AuN_3*2CH_2Cl_2$
Formula weight	986.10	1083.85
Temperature/K	100(2)	100.0(2)
Crystal system	monoclinic	monoclinic
Space group	P2 ₁ /n	P2 ₁ /n
a/Å	8.39130(10)	17.0103(2)
b/Å	44.4079(3)	11.96050(10)
c/Å	13.64620(10)	25.6029(3)
α/°	90	90
β/°	102.5990(10)	106.2340(10)
γ/°	90	90
Volume/Å ³	4962.67(8)	5001.26(10)
Z	4	4
$\rho_{calc}g/cm^3$	1.320	1.439
μ/mm ⁻¹	5.861	7.773
F(000)	2032.0	2208.0
Crystal size/mm ³	$0.105 \times 0.049 \times 0.032$	$0.149 \times 0.113 \times 0.067$
Radiation	$CuK\alpha (\lambda = 1.54184)$	Cu K α ($\lambda = 1.54184$)
2Θ range for data collection/°	6.93 to 160.87	5.598 to 161.96
Index ranges	$-10 \le h \le 9, -56 \le k \le 56, -17 \le l \le 17$	$-21 \le h \le 21, -15 \le k \le 11,$ $-32 \le l \le 32$
Reflections collected	164536	114378
Independent reflections	10814 [$R_{int} = 0.0593$, $R_{sigma} = 0.0204$]	$10884 [R_{int} = 0.0676, R_{sigma} = 0.0299]$
Data/restraints/parameters	10814/0/557	10884/0/564
Goodness-of-fit on F ²	1.197	1.043
Final R indexes [I>=2σ (I)]	$R_1 = 0.0487, wR_2 = 0.1026$	$R_1 = 0.0534, wR_2 = 0.1443$
Final R indexes [all data]	$R_1 = 0.0509, WR_2 = 0.1036$	$R_1 = 0.0585, WR_2 = 0.1499$
Largest diff. peak/hole / e Å-3	1.19/-1.45	1.78/-2.15
#CCDC	2216913	2216906



<u>Figure S1:</u> Thermal ellipsoid drawings of (a) $_{BCz}Au^{BAZ}Au_{BCz}$, (b) $_{Cz}Au^{BAZ}Au_{Cz}$ and (c) $_{Bim}Au^{BAZ}Au_{Bim}$ (50% probability)



 $\underline{\textit{Figure S2:}} \ \textit{Thermal ellipsoid drawings of (left)} \ ^{\textit{BZI}} \textit{Au}_{\textit{BCz}} \ \textit{and (right)} \ ^{\textit{BZAC}} \textit{Au}_{\textit{BCz}} \ (50\% \ \textit{probability)}$

Theoretical Modeling

QCHEM software package was used to model the electronic properties of complexes using Density Functional Theory (DFT) and Time Dependent DFT (TDDFT). First, a geometry optimization was performed using the B3LYP functional and LACVP basis set which accounts for molecules containing transition metals. TDDFT calculations were performed on the ground-state optimized structures to estimate the $S_0 \rightarrow S_1$ transition energies and corresponding oscillator strengths. The TDDFT calculations were performed using the LACVP basis, the CAM-B3LYP exchange, the fit-LACVP effective core potential, the random phase approximation, and the omega value set to 0.2 arbitrary units. The center of charge of the hole and electron wavefunctions are extracted from the position of expectation values of the respective wavefunctions. The parameter $d(h^+, e^-)$ describes the separation between the hole and electron charges that constitute the exciton. The visualization of center of charges are demonstrated in Figure S9.

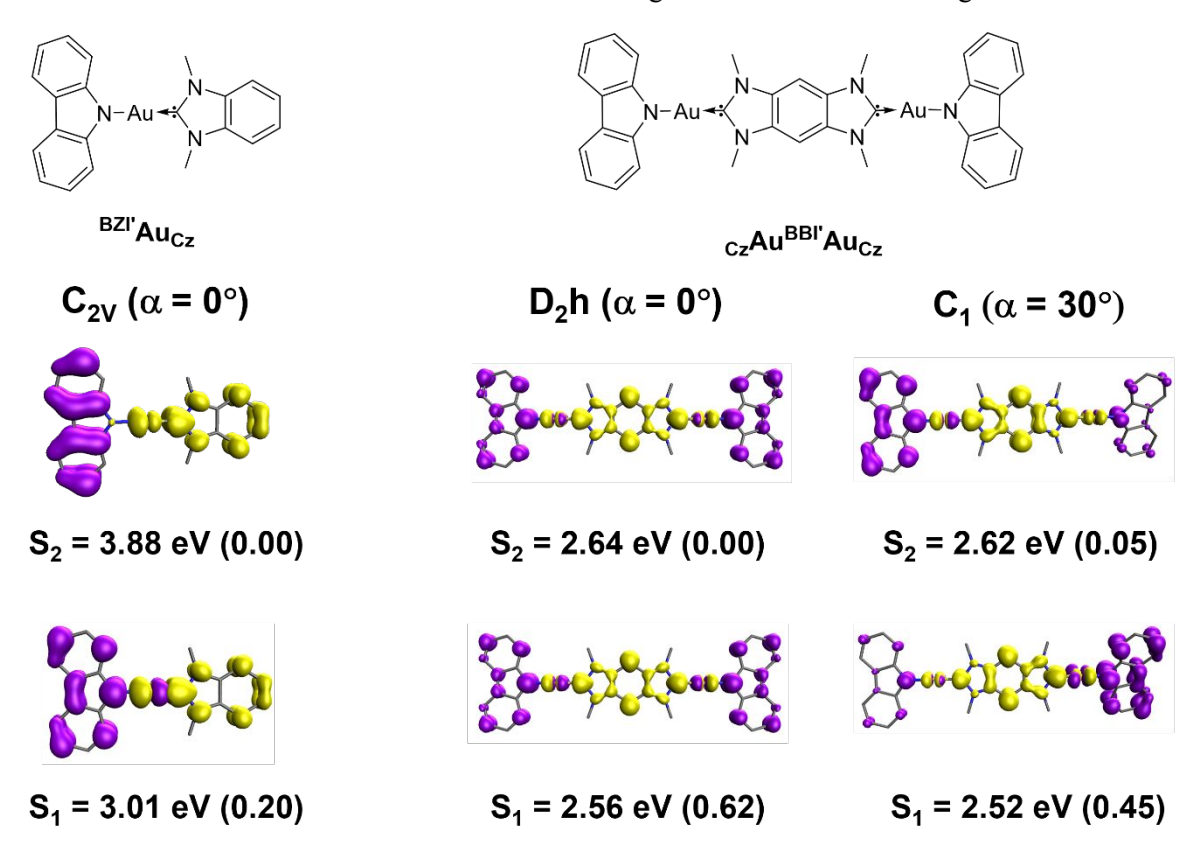


Figure S3a. The NTOs for wavefunctions of $^{BZI'}Au_{Cz}$ (left) and $_{Cz}Au^{BBI'}Au_{Cz}$ (right).

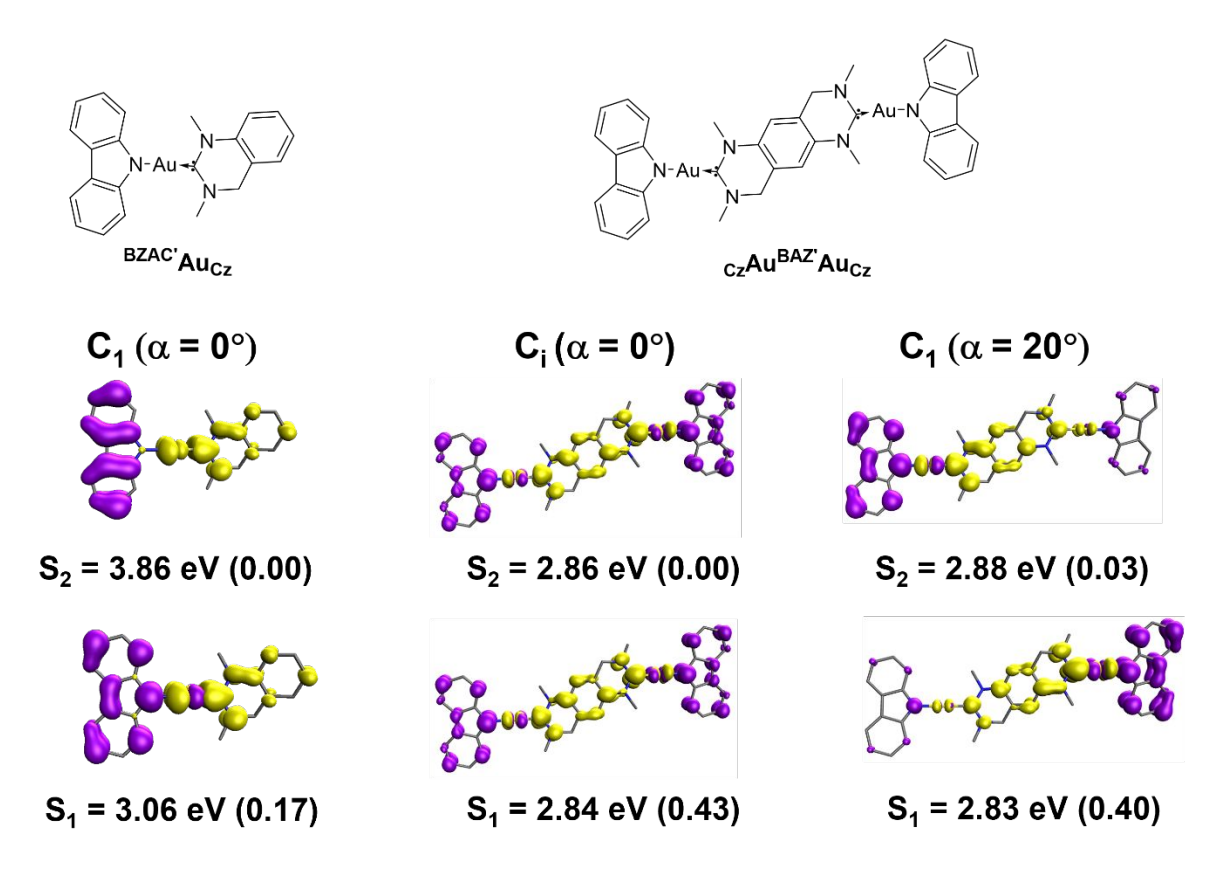


Figure S3b. The NTOs for wavefunctions of $^{BZAC'}Au_{Cz}$ (left) and $_{Cz}Au^{BAZ'}Au_{Cz}$ (right).

The hole (purple) and electron (yellow) wavefunctions of complexes. The value in bracket is the oscillator strength of each state. The iso value was set to 0.1 and the phase information omitted for the wavefunction visualization.

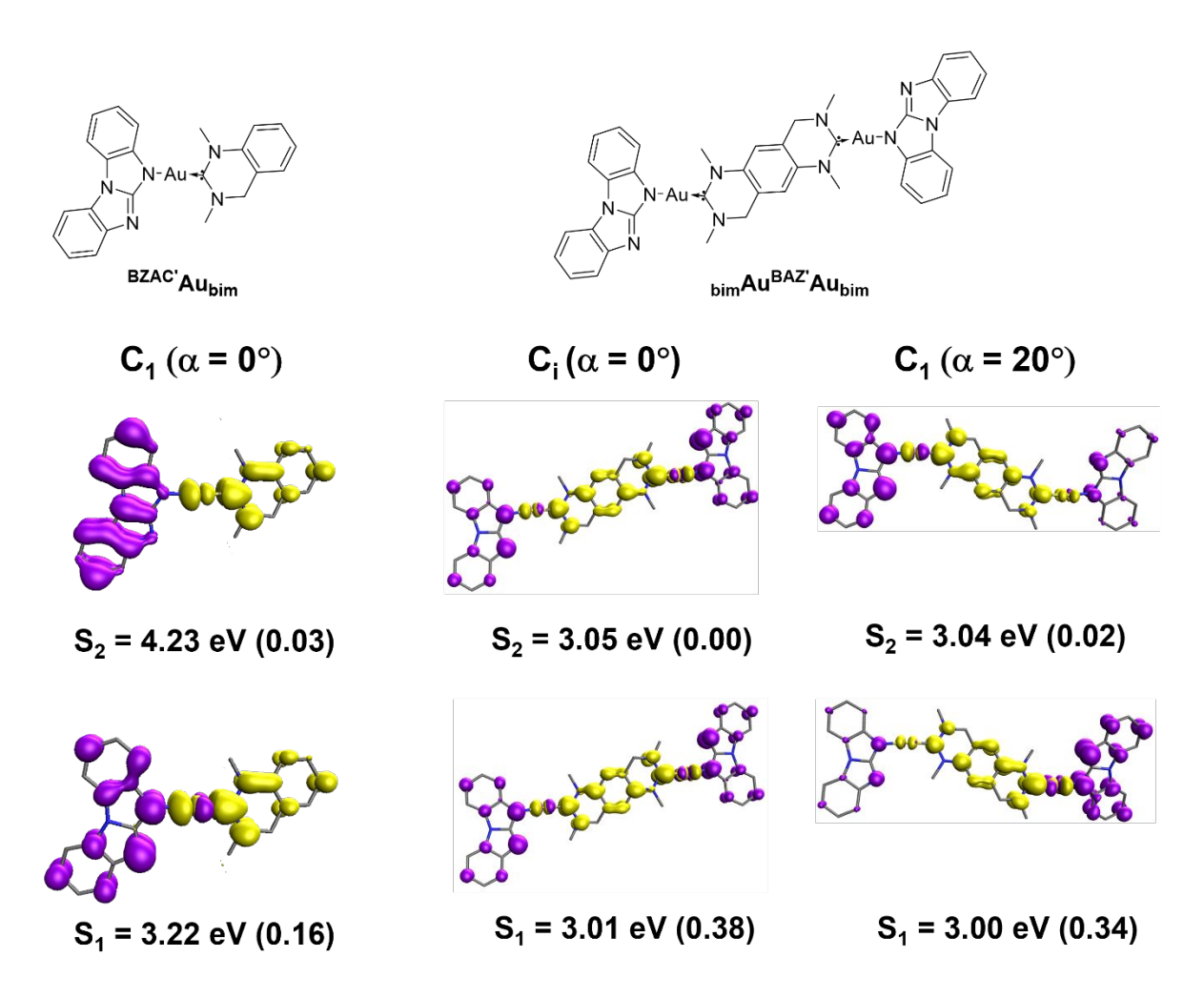


Figure S3c. The NTOs for wavefunctions of $^{BZAC'}\!Au_{bim}$ (left) and $_{bim}\!Au^{BAZ'}\!Au_{bim}$ (right).

Table S3: HOMO-1/HOMO/LUMO/LUMO+X images of all cMa complexes.

Complex	НОМО-1	НОМО	LUMO	LUMO+X
_{Cz} Au ^{BAZ'} Au _{Cz} (Ci symmetry)	8	8	8	8-8
$_{Cz}Au^{BAZ'}Au_{Cz}$ ($\alpha = 20^{\circ}$)		S-pot-	8	8-0-5
$^{\mathrm{BZAC}}\mathbf{A}\mathbf{u}_{\mathrm{Cz}}$			8.	
$_{Cz}Au^{BBI'}Au_{Cz}$ (D2h symmetry)			8-01-10-8	800000
$_{\text{Cz}}\text{Au}^{\text{BBI'}}\text{Au}_{\text{Cz}}$ ($\alpha = 30^{\circ}$)		B	8 mg (mg	8
BZI'Au _{Cz}				
$_{bim}Au^{BAZ'}Au_{bim}$ (Ci symmetry)			}	3-4-6
$_{bim}Au^{BAZ'}Au_{bim}$ ($\alpha = 20^{\circ}$)		S->->-	8	
^{BZAC} 'Au _{Cz}				

Table S4. Energies of the frontier orbitals and excited states for the cMa complexes

Complex	HO/HO-1 (eV)	LU (eV)	ΔE _{HO,LU} (eV)	S ₁ (eV/f)	S ₂ (eV/f)	T ₁ / T ₂ (eV)	ΔE _{ST} (eV)
$_{Cz}Au^{BAZ'}Au_{Cz}$ (Ci symmetry)	-4.54/-4.55	-2.18	2.36	2.84/0.43	2.86/0.00	2.65/2.66	0.19
$_{Cz}Au^{BAZ'}Au_{Cz}$ ($\alpha = 10^{\circ}$)	-4.55/-4.56	-2.17	2.38	2.84/0.46	2.89/0.00	2.66/2.67	0.18
$_{Cz}Au^{BAZ'}Au_{Cz}$ ($\alpha = 20^{\circ}$)	-4.55/-4.56	-2.17	2.38	2.83/0.40	2.88/0.03	2.66/2.67	0.17
BZAC'Au _{Cz}	-4.17/-4.76	-1.43	2.74	3.06/0.17	3.86/0.00	2.86/3.22	0.20
$_{Cz}Au^{BBI'}Au_{Cz}$ (D2h symmetry)	-4.57/-4.62	-2.50	2.07	2.56/0.62	2.64/0.00	2.36/2.40	0.20
$_{\text{Cz}}\text{Au}^{\text{BBI}'}\text{Au}_{\text{Cz}}$ ($\alpha = 10^{\circ}$)	-4.59/-4.63	-2.54	2.05	2.55/0.55	2.64/0.00	2.39/2.44	0.16
$_{\text{Cz}}\text{Au}^{\text{BBI}'}\text{Au}_{\text{Cz}}$ ($\alpha = 20^{\circ}$)	-4.58/-4.63	-2.55	2.03	2.54/0.52	2.63/0.01	2.39/2.43	0.15
$_{\text{Cz}}\text{Au}^{\text{BBI}'}\text{Au}_{\text{Cz}}$ ($\alpha = 30^{\circ}$)	-4.57/-4.62	-2.56	2.01	2.52/0.45	2.62/0.05	2.38/2.42	0.14
^{BZI} 'Au _{Cz}	-4.22/-4.80	-1.47	2.75	3.08/0.20	3.88/0.00	2.87/3.21	0.21
bimAu ^{BAZ'} Au _{bim} (Ci symmetry)	-4.61/-4.62	-2.12	2.49	3.01/0.39	3.05/0.00	2.88/2.90	0.13
$_{bim}Au^{BAZ'}Au_{bim}$ ($\alpha = 10^{\circ}$)	-4.61/-4.62	-2.12	2.49	3.01/0.37	3.05/0.00	2.88/2.90	0.13
$_{bim}Au^{BAZ'}Au_{bim}$ ($\alpha=20^{\circ}$)	-4.60/-4.62	-2.13	2.47	3.00/0.33	3.04/0.02	2.88/2.90	0.12
BZAC'Au _{bim}	-4.28/-5.00	-1.43	2.85	3.22/0.16	4.23/0.03	3.06/3.33	0.16

Table S5. Compositions of the excited states for the cMa complexes.

Complex	S_1	S_2	T_1	T_2
$_{Cz}Au^{BAZ^{\prime}}Au_{Cz}$	HO-1→ LU+2 19%	HO-1→ LU 77%	HO-1→LU+2 24%	HO-1→ LU 68%
(Ci symmetry)	HO→LU 77%	HO→LU+2 20%	HO→LU 69%	HO→LU+2 25%
$_{Cz}Au^{BAZ^{\prime}}Au_{Cz}$	HO-1→ LU+2 18%	HO-1→ LU 75%	HO-1→LU+2 22%	HO-1→ LU 67%
$(\alpha = 10^{\circ})$	HO→LU 75%	HO→LU+2 19%	HO→LU 68%	HO→LU+2 23%
A DA7/ A	HO-1→ LU+2 12%	HO-1→ LU 73%	HO-1→ LU+2 11%	HO-1→ LU 67%
$_{Cz}Au^{BAZ'}Au_{Cz}$	HO→LU 74%	HO→LU+2 8%	HO→LU 68%	HO→LU+2 13%
$(\alpha = 20^{\circ})$	HO→LU+2 8%	HO→LU+2 12%	HO→LU+2 13%	HO→LU+2 12%
^{BZAC} 'Au _{Cz}	110 .111.040/	HO-1→LU 96%	HO→LU 88%	
Au_{Cz}	HO→LU 94%	HO-1→LU 90%	HO→LU+6 6%	
_{Cz} Au ^{BBI} 'Au _{Cz}	HO-1→ LU+1 9%	HO-1→ LU 88%	HO-1→ LU+1 12%	HO-1→ LU 80%
(D2h symmetry)	HO→LU 88%	HO→LU+1 10%	HO→LU 82%	HO→LU+1 15%
_{Cz} Au ^{BBI} 'Au _{Cz}	HO-1→ LU+1 7%	HO-1→ LU 92%	HO-1→ LU+1 9%	HO-1→ LU 85%
$(\alpha = 10^{\circ})$	HO→LU 91%	HO→LU+1 7%	HO→LU 85%	HO→LU+1 11%
_{Cz} Au ^{BBI} 'Au _{Cz}	HO-1→ LU+1 6%	HO-1→ LU 92%	HO-1→ LU+1 9%	HO-1→ LU 84%
$(\alpha = 20^{\circ})$	HO→LU 91%	HO→LU+1 6%	HO→LU 84%	HO→LU+1 10%
A RRI' A	HO 1 . I II + 1 50/	HO 1 . I H 010/	HO-1→ LU 5%	HO-1→ LU 80%
$_{\rm Cz}{\rm Au^{BBI'}Au_{\rm Cz}}$	$HO-1 \rightarrow LU+1.5\%$	HO-1→ LU 91%	$HO-1 \rightarrow LU+1.7\%$	$HO \rightarrow LU 5\%$
$(\alpha = 30^{\circ})$	HO→LU 90%	HO→LU+1 4%	HO→LU 80%	HO→LU+1 9%
BZI' A	110 . 1 11 020/	110 1 .111 040/	HO→LU 85%	
$^{\mathrm{BZI'}}\!\mathrm{Au}_{\mathrm{Cz}}$	HO→LU 92%	HO-1→LU 94%	HO→LU+6 6%	
_{bim} Au ^{BAZ'} Au _{bim}	HO-1→ LU+2 16%	HO-1→ LU 80%	HO-1→ LU+2 18%	HO-1→ LU 73%
(Ci symmetry)	HO→LU 79%	HO→LU+2 17%	HO→LU 70%	HO→LU+2 20%
_{bim} Au ^{BAZ'} Au _{bim}	HO-1→ LU+2 16%	HO-1→ LU 78%	HO-1→ LU+2 17%	HO-1→ LU 72%
$(\alpha = 10^{\circ})$	HO→LU 78%	HO→LU+2 17%	HO→LU 70%	HO→LU+2 20%
	HO 1 . I II 2 100/	HO 1 . I I I 7/0/	HO-1→ LU 6%	HO-1→ LU 66%
$_{bim}Au^{BAZ^{\prime}}Au_{bim}$	$HO-1 \rightarrow LU+2 10\%$	HO-1→ LU 76%	$\text{HO-1} \rightarrow \text{LU+2 } 12\%$	$\text{HO-1} \rightarrow \text{LU+2} 5\%$
$(\alpha = 20^{\circ})$	HO→LU 75%	HO-1→LU+2 6%	HO→LU 64%	HO→LU 6%
	HO→ LU+2 7%	$HO \rightarrow LU+2 11\%$	$HO \rightarrow LU+2.6\%$	$HO \rightarrow LU+2 15\%$
BZAC'Au bim	HO→LU 93%	HO-1→LU 93%	HO→LU 87%	

Table S6. Dipole moments of the ground and excited states.

Complex	$\mu S_0 (D)$	$\mathbf{S}_{1}\left(\mathbf{D}\right)$	$egin{array}{c} \mu \\ S_2 \left(D \right) \end{array}$	μ $T_1(D)$	μ Τ ₂ (D)
CzAu ^{BAZ'} Au _{Cz} (Ci symmetry)	0.00	0.21	0.21	0.85	0.85
$C_z A u^{BAZ'} A u_{Cz}$ ($\alpha = 10^\circ$)	0.36	3.50	3.48	4.58	4.53
$_{\text{Cz}}\text{Au}^{\text{BAZ'}}\text{Au}_{\text{Cz}}$ ($\alpha = 20^{\circ}$)	0.12	12.89	13.05	16.45	16.34
BZAC'Au _{Cz}	11.68	12.72	17.48	10.70	10.87
CzAu ^{BBI'} AuCz (D2h symmetry)	0.00	0.00	0.00	0.00	0.00
$_{\text{Cz}}\text{Au}^{\text{BBI}}\text{Au}_{\text{Cz}}$ ($\alpha = 10^{\circ}$)	0.03	1.93	1.99	0.56	0.54
$_{\text{Cz}}\text{Au}^{\text{BBI'}}\text{Au}_{\text{Cz}}$ ($\alpha = 20^{\circ}$)	0.10	7.33	7.56	2.35	2.29
$_{\text{Cz}}\text{Au}^{\text{BBI'}}\text{Au}_{\text{Cz}}$ ($\alpha = 30^{\circ}$)	0.22	15.71	16.20	5.64	5.54
^{BZI} 'Au _{Cz}	12.09	12.49	17.47	9.70	11.44
_{bim} Au ^{BAZ'} Au _{bim} (Ci symmetry)	0.00	0.21	0.22	0.55	0.55
$_{\text{bim}}$ Au $^{\text{BAZ'}}$ Au $_{\text{bim}}$ ($\alpha = 10^{\circ}$)	0.46	2.05	2.07	2.38	2.48
$_{bim}Au^{BAZ'}Au_{bim}$ ($\alpha = 20^{\circ}$)	0.72	11.85	12.16	6.73	6.73
BZAC'Au _{bim}	10.85	15.17	20.76	12.65	12.20

Table S7. Transition dipole moments of the excited states.

Complex	S ₁ X	S ₁ Y	S ₁ Z	S ₂ X	S ₂ Y	S_2Z
$_{Cz}Au^{BAZ'}Au_{Cz}$ (Ci symmetry)	2.4814	-0.2782	-0.0557	-0.0093	0.0014	0.0004
$C_z A u^{BAZ'} A u_{Cz}$ $(\alpha = 10^\circ)$	-2.9632	-0.0022	0.0012	-0.1125	-0.0005	0.0000
${_{Cz}Au^{BAZ'}Au_{Cz}}$ $(\alpha = 20^{\circ})$	-2.4012	-0.2509	0.0840	-0.6957	-0.0644	0.0120
BZAC'Au _{Cz}	-1.4793	-0.2399	-0.0223	0.0051	-0.0189	-0.0013
CzAu ^{BBI'} Au _{Cz} (D2h symmetry)	-3.1527	0	0	0	0	0
$C_z A u^{BBI'} A u_{Cz}$ ($\alpha = 10^\circ$)	-2.9632	-0.0022	0.0012	-0.1125	-0.0005	0.0000
$C_z A u^{BBI'} A u_{Cz}$ ($\alpha = 20^\circ$)	-2.8857	0.0027	-0.0003	-0.4097	-0.0024	0.0002
$C_z A u^{BBI'} A u_{Cz}$ ($\alpha = 30^\circ$)	2.7017	0.0060	-0.0035	0.8838	0.0084	0.0030
BZI'Au _{Cz}	-1.6403	0.1168	0.0089	-0.0031	-0.0385	0.0031
bimAu ^{BAZ'} Au _{bim} (Ci symmetry)	2.2378	-0.2830	-0.0515	0.0035	-0.0040	0.0008
$\frac{1}{\text{bim}} A u^{\text{BAZ'}} A u_{\text{bim}}$ $(\alpha = 10^{\circ})$	2.2129	-0.2758	-0.0447	-0.0914	0.0042	0.0167
$\frac{1}{\text{bim}} A u^{\text{BAZ'}} A u_{\text{bim}}$ ($\alpha = 20^{\circ}$)	2.1219	-0.2506	-0.0414	-0.5265	0.0717	0.0264
BZAC'Au _{bim}	-1.3827	0.3281	-0.0026	0.4955	-0.0133	0.0030

TD-DFT calculations using cam-B3LYP/LACVP were performed to study the S_1 , S_2 , T_1 and T_2 excited states with varying conformations. The geometries optimized in the PES scan were used for calculations, with a 30-degree dihedral angle interval. The PES scan for binuclear complexes was conducted by constraining one dihedral angle between the carbene and the amides (Cz or bim) at 0° while twisting the other dihedral angle (α) away from 0° . As the dihedral angle increase from 0 to 90, S_1 is the transition mainly from the twisted Cz or bim to the center carbene, while S_2 is the transition mainly from the coplanar Cz or bim. Thus, the S_1 is stabilized to a greater extent by the twisted Cz or bim due to the decreasing electronic interaction. Additionally, the oscillator strength of the S_1 drops as the α increases. S_1 and S_2 states are slightly affected by the twisting conformations. At 90 degrees, S_1 and S_2 are close in energy to the S_1 state. In the mono analog, the S_1 and S_2 state follow the same trend, while the S_2 and S_2 state are barely affected and remain high in energy.

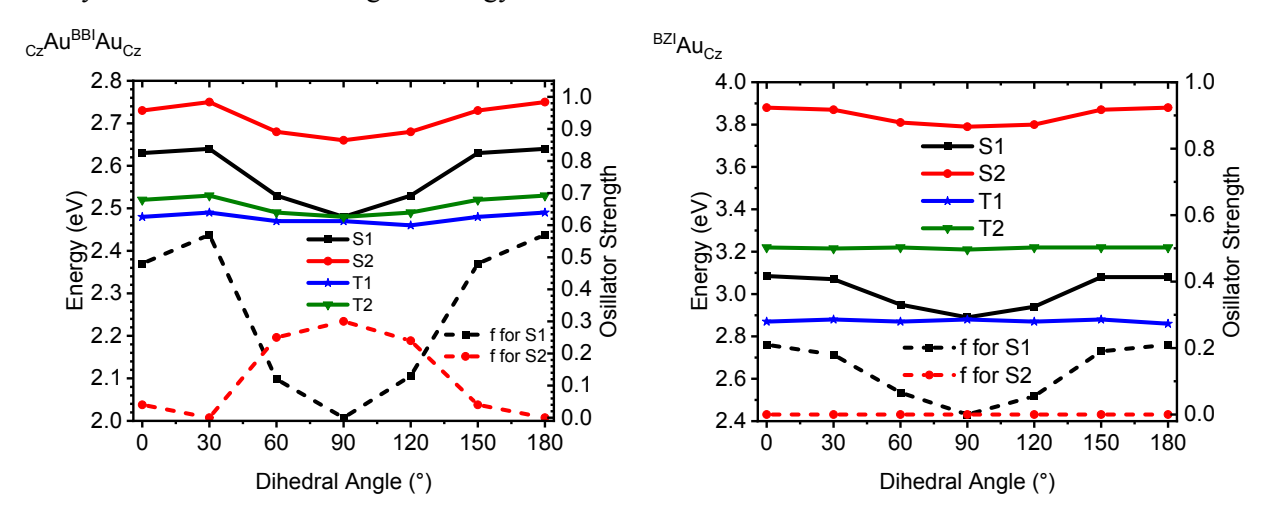


Figure 4a. Calculated S_1 , S_2 (with oscillator strength) and T_1 , T_2 energies of $C_2Au^{BBI}Au_{Cz}$ (left) and $C_2Au^{BBI}Au_{Cz}$ (right) with respect to their dihedral angles $C_2Au^{BBI}Au_{Cz}$

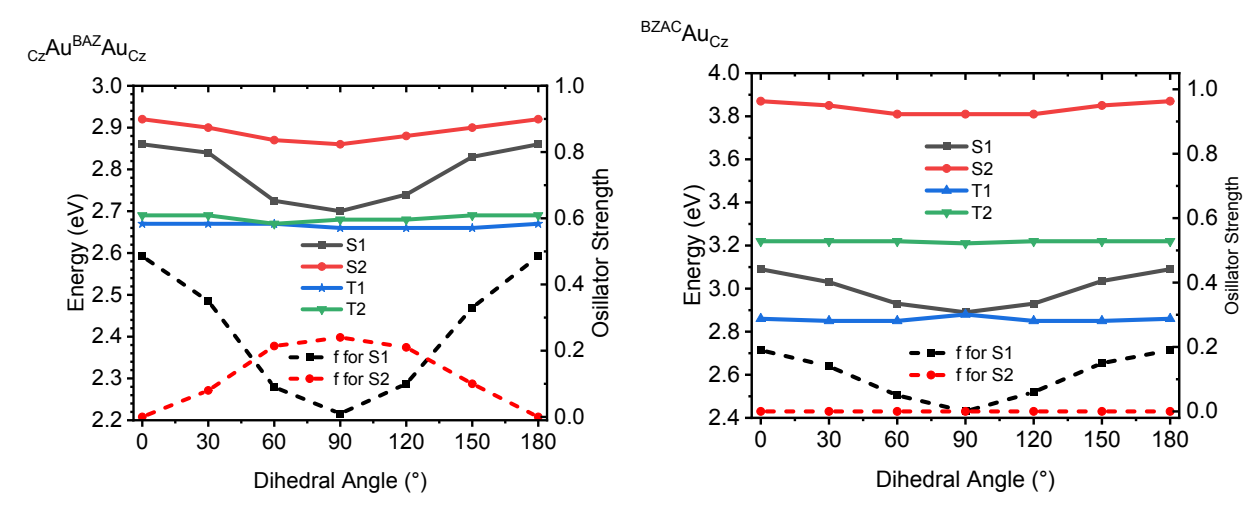


Figure 4b. Calculated S_1 , S_2 (with oscillator strength) and T_1 , T_2 energies of $C_2Au^{BAZ}Au_{Cz}$ (left) and $C_2Au^{BAZ}Au_{Cz}$ (right) with respect to their dihedral angles α

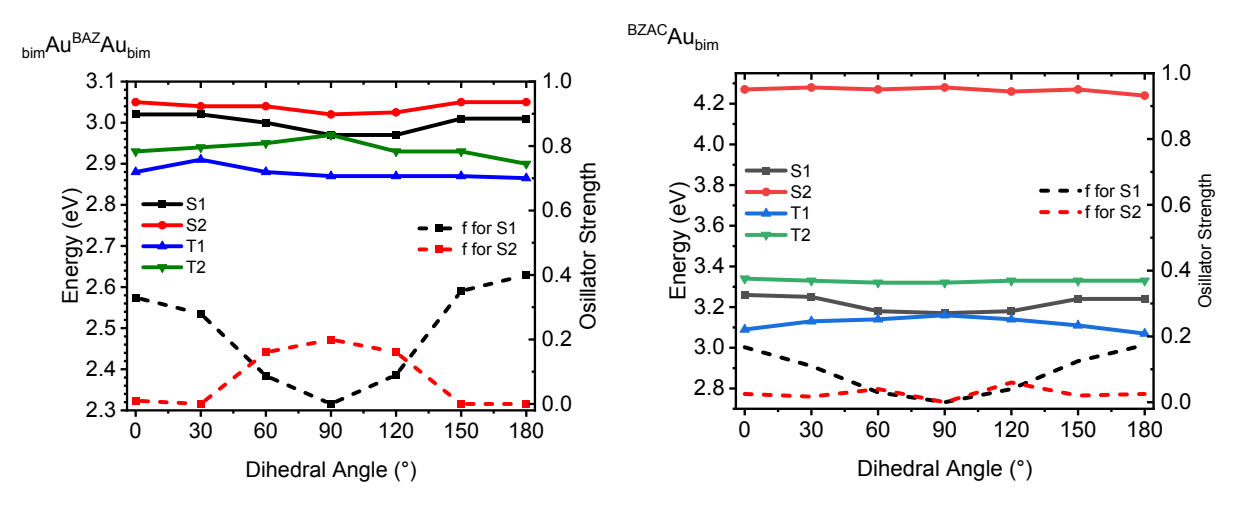


Figure 4c. Calculated S_1 , S_2 (with oscillator strength) and T_1 , T_2 energies of $_{bim}Au^{BAZ}Au_{bim}$ (left) and $^{BZAC}Au_{bim}$ (right) with respect to their dihedral angles α

Table S8. h^+ , e^- separation distances for cMa complexes

	S1(Å)	T1(Å)
$_{BCz}Au^{BAZ}Au_{BCz}$	6.17	5.56
$^{\mathrm{BZAC}}\mathrm{Au}_{\mathrm{BCz}}$	5.19	4.74
$_{BCz}Au^{BBI}Au_{BCz}$	6.87	6.27
^{BZI} Au _{BCz}	5.30	4.72
_{bim} Au ^{BAZ} Au _{bim}	6.29	5.33
_{bim} Au ^{BZAC}	5.39	4.83

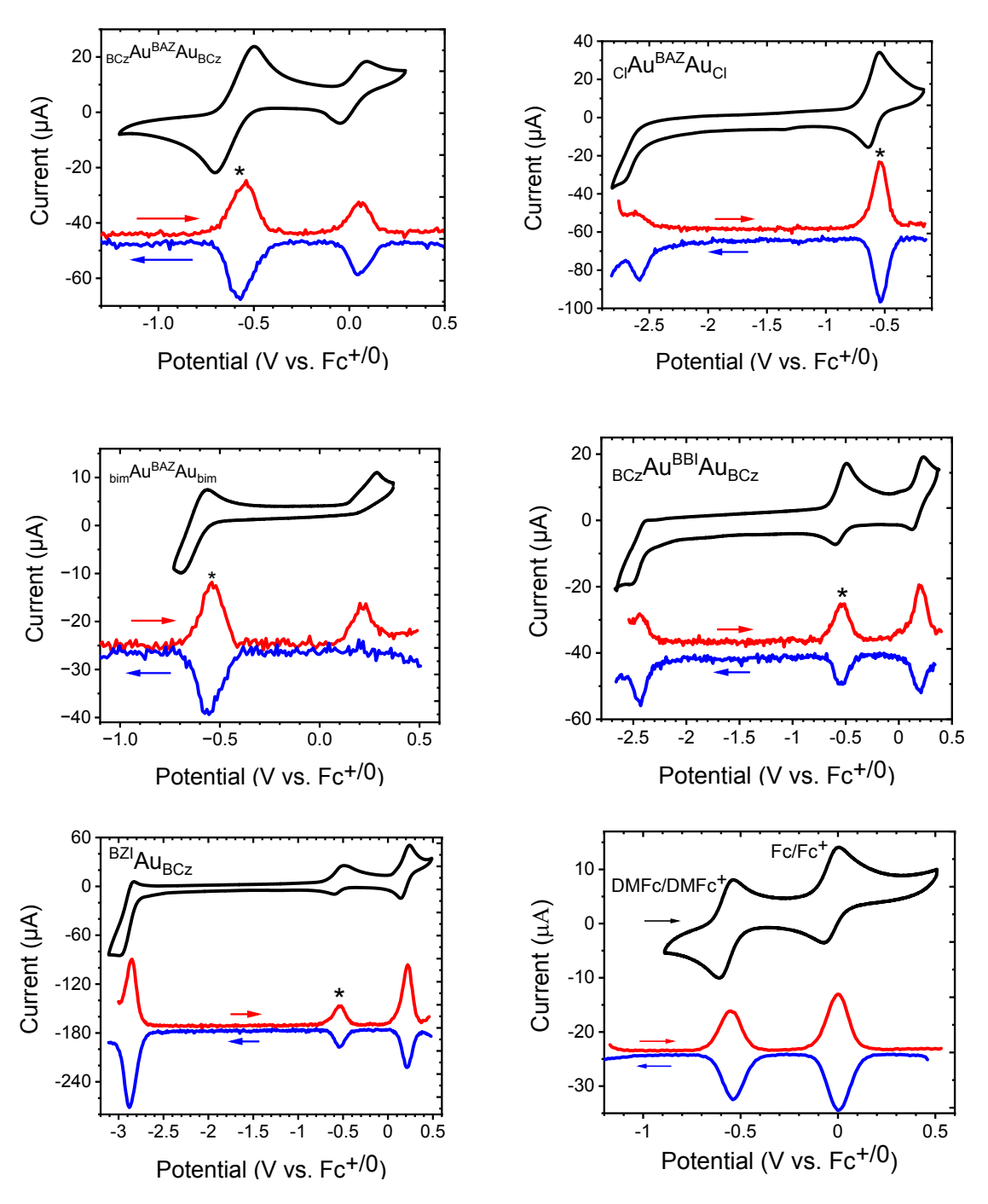
Table S9. Center of h+,e- for S1 NTOs for cMa complexes.

The d(h⁺, e⁻) calculation on the geometry of complexes $_{BCz}Au^{BAZ}Au_{BCz}$, $_{BCz}Au^{BBI}Au_{BCz}$ and $_{bim}Au^{BAZ}Au_{bim}$ is zero because the centers of h⁺ and e⁻ are overlapped because of the symmetry. To avoid this situation, these complexes' d(h⁺, e⁻) calculation was done by swapping one amide ligand to a Cl⁻ which are $_{BCz}Au^{BAZ}Au_{Cl}$, $_{BCz}Au^{BBI}Au_{Cl}$ and $_{bim}Au^{BAZ}Au_{Cl}$.

Complex	Center of Hole	Center of Electron
$_{\mathrm{BCz}}\mathrm{Au^{BAZ}Au_{BCz}}$		
^{BZAC} Au _{BCz}		
$_{\mathrm{BCz}}\mathrm{Au^{BBI}Au_{BCz}}$		
^{BZI} Au _{BCz}		
$_{\text{bim}}Au^{BAZ}Au_{\text{bim}}$		
$^{ m BZAC}\!{ m Au}_{ m bim}$		

Electrochemistry

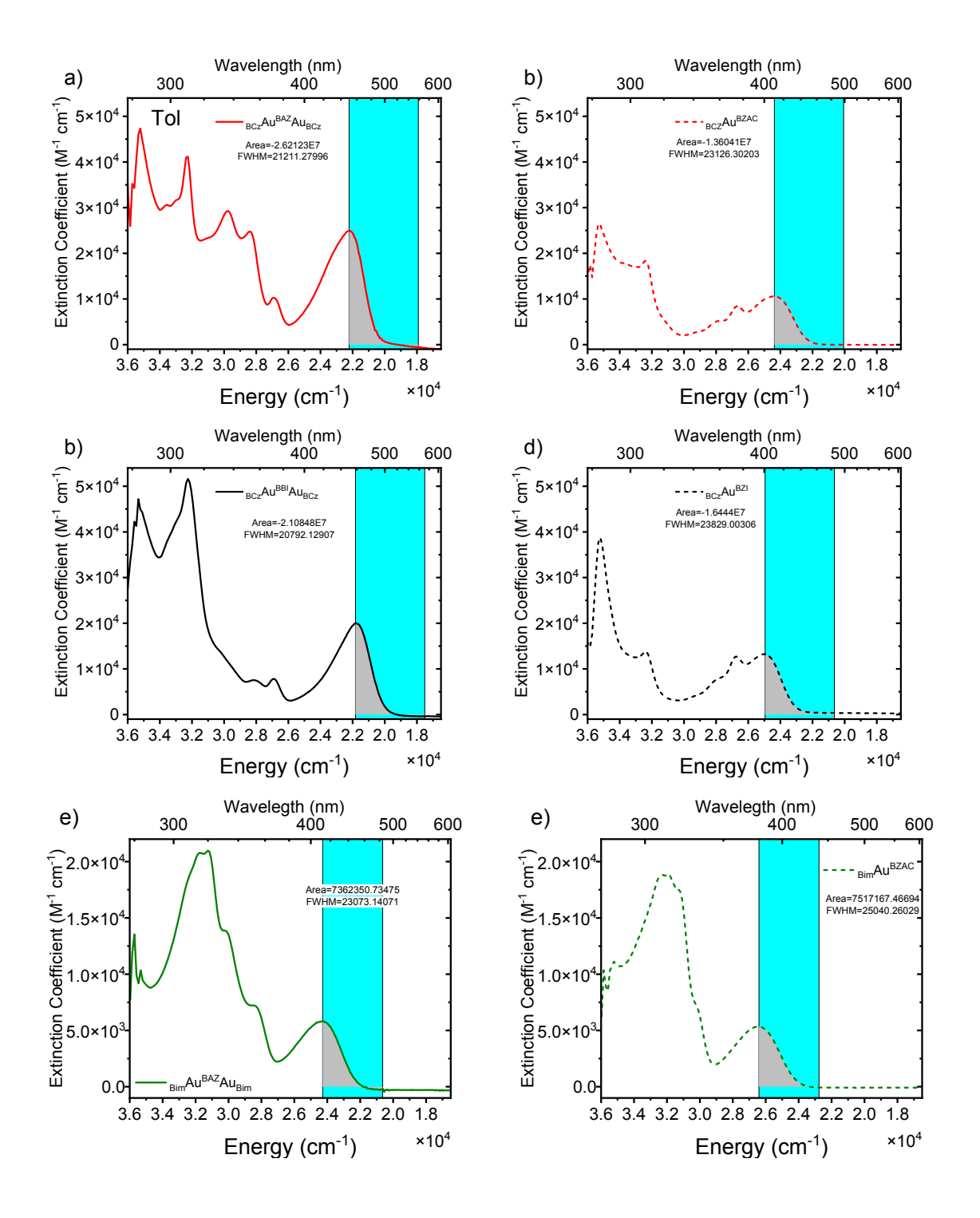
Cyclic voltammetry (CV) and differential pulse voltammetry (DPV) were performed in tetrahydrofuran (THF) or N, N-Dimethylformamide (DMF) using a VersaSTAT 3 potentiostat with a 0.1 M tetra-n-butyl ammonium hexafluorophosphate (TBAF) as the supporting electrolyte, an Ag wire was used as the pseudo reference electrode, a Pt wire as the counter electrode, and a glassy carbon rod as the working electrode. Decamethylferrocene is employed as an internal reference. To determine the relative redox potential of decamethylferrocene compared to ferrocene, CV and DPV scans are performed in acetonitrile (MeCN) with these two references only as shown in Figure S2. Two references present reversible oxidation peaks as shown in CV plots. According to the DPV results, when the redox potentials of ferrocene are fixed to 0.0 V, those of decamethylferrocene are around -0.54 V. Thus, by setting the decamethylferrocene reference peaks at -0.54 V, all the samples' redox potentials are reported relative to 0.0 V for ferrocene. The redox potentials of complexes are based on the values from differential pulsed voltammetry measurements and are reported relative to the Fc⁺/Fc redox couple, whereas cyclic voltammetry was measured to look at if any electrochemical reversibility is inherent to these materials in order to obtain more accurate redox potentials. The CV and DPV of complexes were taken in DMF except the oxidation of BCzAuBAZAuBCz was taken in THF.



<u>Figure S5.</u> CV (black) and DPV (red: oxidation, blue: reduction) traces of complexes and decamethylferrocene collected in THF or DMF or MeCN with 0.1 M TBAPF₆ as an electrolyte. The asterisk indicates the redox peak of decamethylferrocene. The electrochemical plot at the bottom shows a comparison of Fc and DMFc.

Photophysical measurements

2-Methyl tetrahydrofuran (2-MeTHF) and methylcyclohexane (MeCy) were purchased from Sigma-Aldrich. Tetrahydrofuran (THF) and toluene (Tol) were purified using a Pure Process Technology solvent dispensing system. Absorbance and molar absorptivity data were measured using a UV-vis Hewlett-Packard 4853 diode array spectrometer. Steady state emission spectra were obtained using a Photon Technology International QuantaMaster spectrofluorimeter. Solution samples with concentration of 10⁻⁵ M were prepared under N₂ in a glass cuvette fitted with a Teflon stopcock. Photoluminescence quantum yields were recorded using a Hamamatsu C9920 integrating sphere equipped with a xenon lamp. Luminescence lifetimes were measured using Time-Correlated Single Photon Counting (TCSPC) on an IBH Fluorocube apparatus.



<u>Figure S6.</u> Integration of the low energy half of the CT-Band for BCz and bim complexes in Tol. The ICT and amide absorption bands do not overlap in the bim derivatives as the π - π * transitions in bim are at higher energy ($\lambda = 310 \text{ nm}$)² than in BCz ($\lambda = 372 \text{ nm}$).²

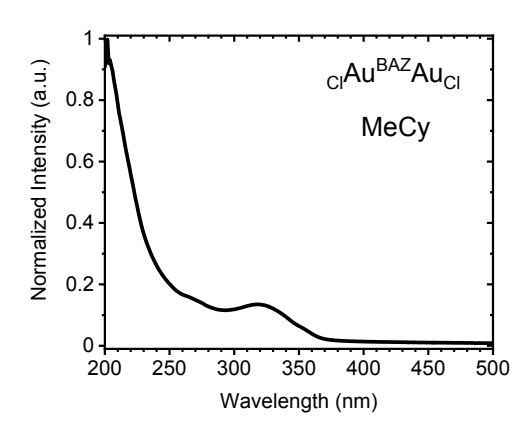


Figure S7. Absorption spectrum of $C_{Cl}Au^{BAZ}Au_{Cl}$ in MeCy.

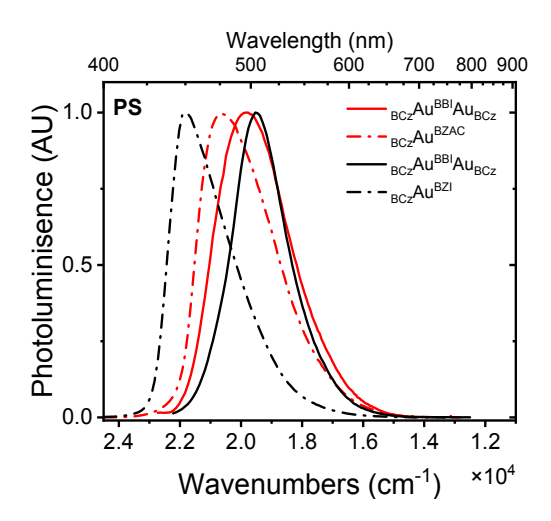


Figure S8. Emission of all BCz mono and binuclear complexes in PS.

<u>Table S10:</u> Integrated Area of the CT Band in Toluene from Figure S5. Ratio was $determined \ by: \ Ratio = \frac{Biscarbene}{Monocarbene}.$

	Monocurbene	
	Areas (M ⁻¹ cm ⁻²) x10 ⁷	Ratio
$_{\mathrm{BCz}}\mathrm{Au^{BAZ}Au_{BCz}}$	2.62	1.9
$^{ m BZAC}Au_{ m BCz}$	1.36	
$_{BCz}Au^{BBI}Au_{BCz}$	2.11	1.3
$^{\mathrm{BZI}}\mathrm{Au}_{\mathrm{BCz}}$	1.64	
$_{Bim}Au^{BAZ}Au_{Bim}$	0.74	1.0
$_{\text{Bim}}Au^{\text{BZAC}}$	0.75	

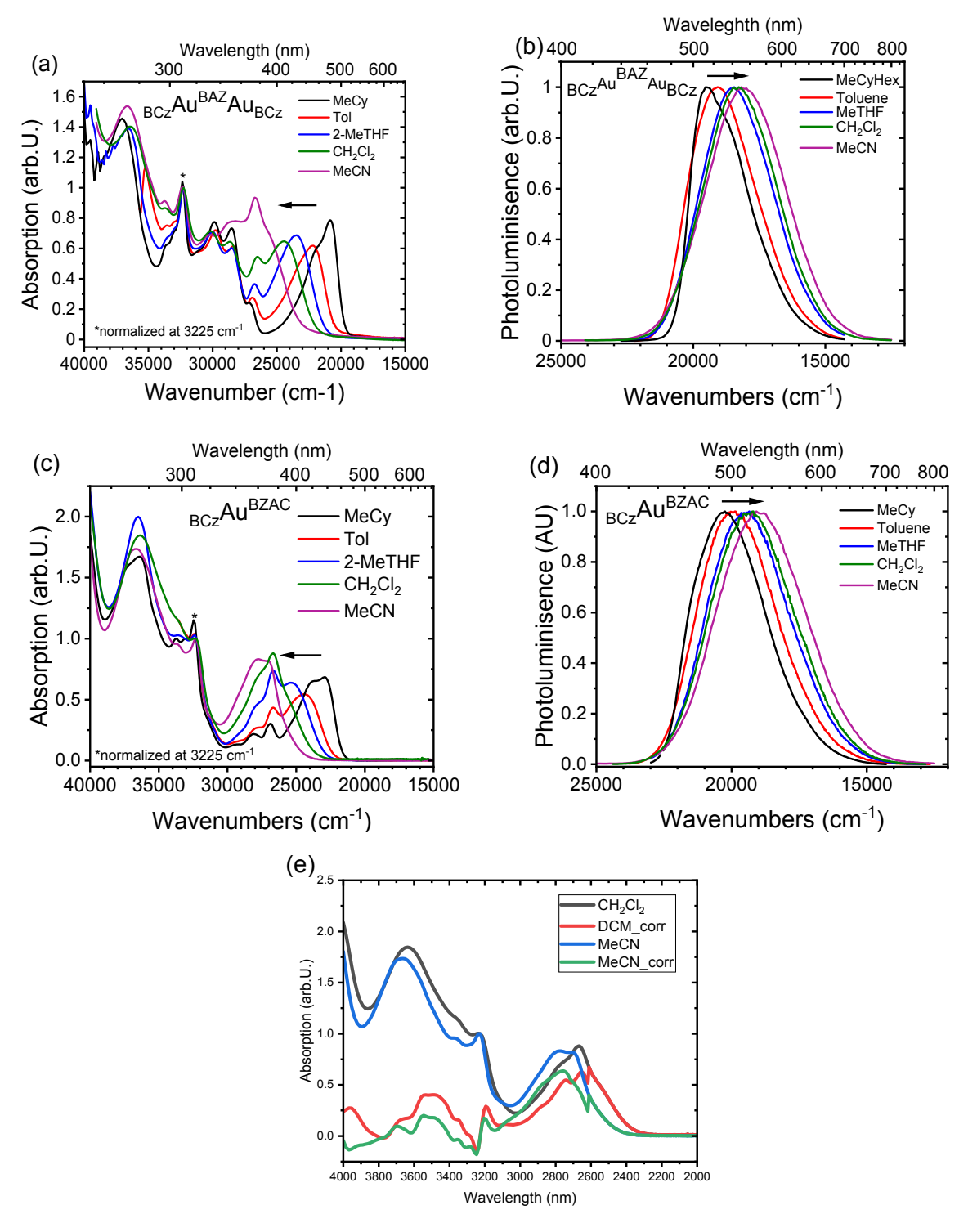


Figure S9(a-d): Solvent dependent Absorption and Emission spectra for $_{BCz}Au^{BAZ}Au_{BCz}$, $_{BCz}Au^{BAZ}$ in MeCycloHexane, Toluene, 2-MeTHF, Dichloromethane and Acetonitrile., (e) correction by substracting the MeCyHexane spectra >30000cm-1 to remove the BCz band from the Absorption spectra, to determine the Abs_{max} of $^{BZAC}Au_{BCz}$

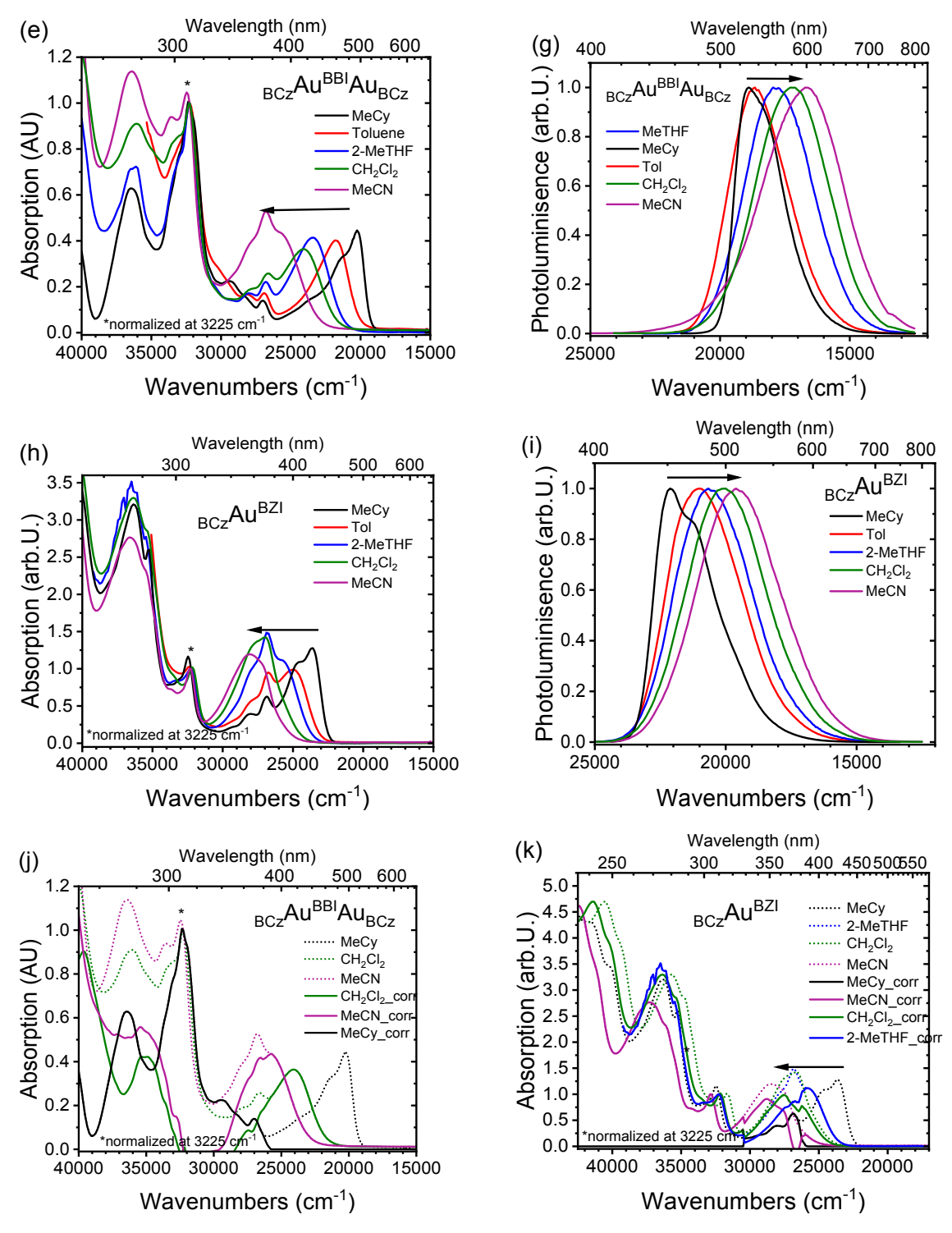


Figure S9(f-i): Solvent dependent Absorption and Emission spectra for $_{BCz}Au^{BBI}Au_{BCz}$, $_{BCz}Au^{BZ}$ in MeCycloHexane, Toluene, 2-MeTHF, Dichloromethane and Acetonitrile, (j,k) correction by substracting the MeCyHexane spectra $> 30000cm^{-1}$ to remove the BCz band from the Absorption spectra, to determine the Abs_{max} for $_{BCz}Au^{BBI}Au_{BCz}$ and $_{BZI}Au_{BCz}$

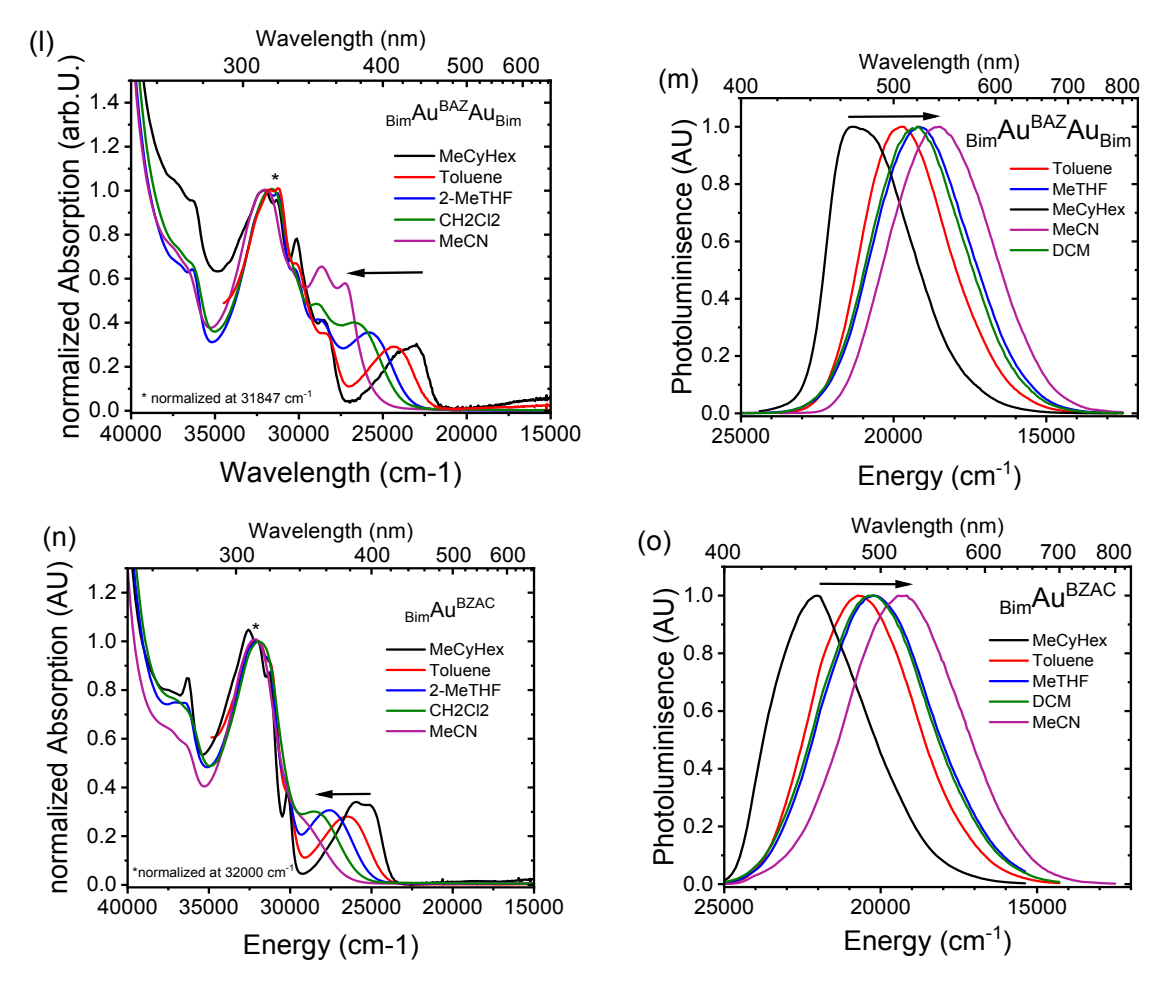


Figure S9(l-o): Solvent dependent Absorption and Emission spectra for $_{Bim}Au^{BAZ}Au_{Bim}$, $_{Bim}Au^{BAZ}$ in MeCycloHexane, Toluene, 2-MeTHF, Dichloromethane and Acetonitrile.

cpd	Abs _{max} (nm)	0h (%)	1h (%)	4h (%)	6h (%)	24h (%)
$^{\mathrm{BZI}}\mathrm{Au}_{\mathrm{BCz}}$	400	100	84.34	79.96	74.74	58.46
$_{BCz}Au^{BBI}Au_{BCz}$	455	100	96.98	89.34	85.71	78.57
$^{\mathrm{BZAC}}\mathrm{Au}_{\mathrm{BCz}}$	410	100	99.31	99.17	97.98	96.80
$_{BCz}Au^{BAZ}Au_{BCz}$	450	100	99.57	95.73	93.59	91.45
$^{\mathrm{BZAC}}\mathrm{Au}_{\mathrm{bim}}$	380	100	99.12	98.59	98.23	95.76
$_{bim}Au^{BAZ}Au_{bim}$	410	100	97.25	95.54	95.53	92.78
Ir(ppy) ₃	380	100	97.51	94.00	93.32	90.63

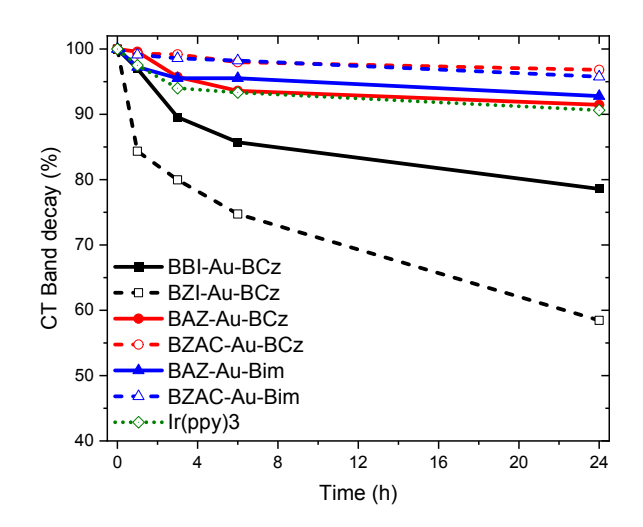


Figure S10: Photostability of all complexes and Ir(ppy)3 as reference in degassed Toluene. Solutions were in an air-free Schlenk cuvette and were excited with a 375nm LED lamp (1450 mW, 19.2 μ W mm⁻²)

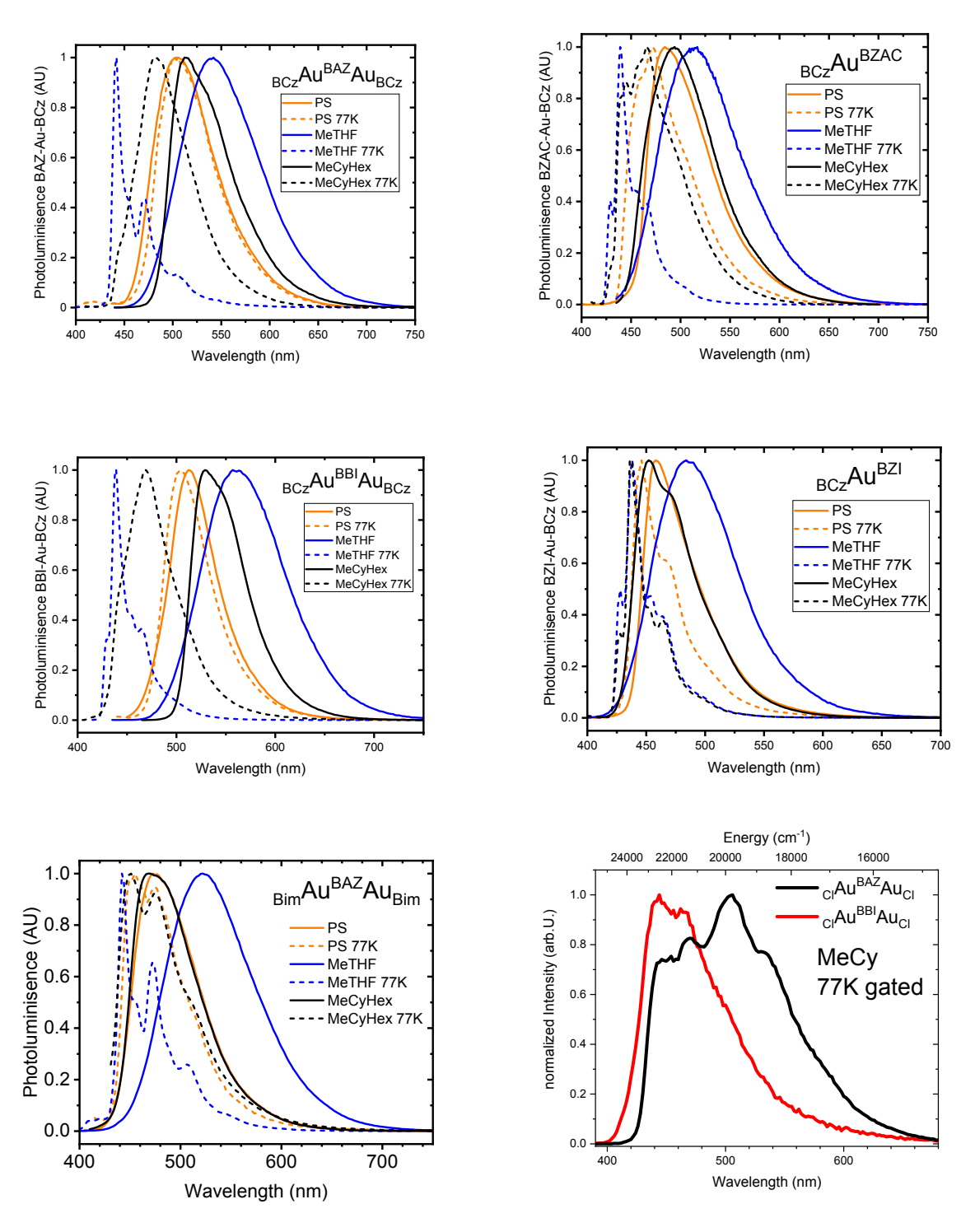
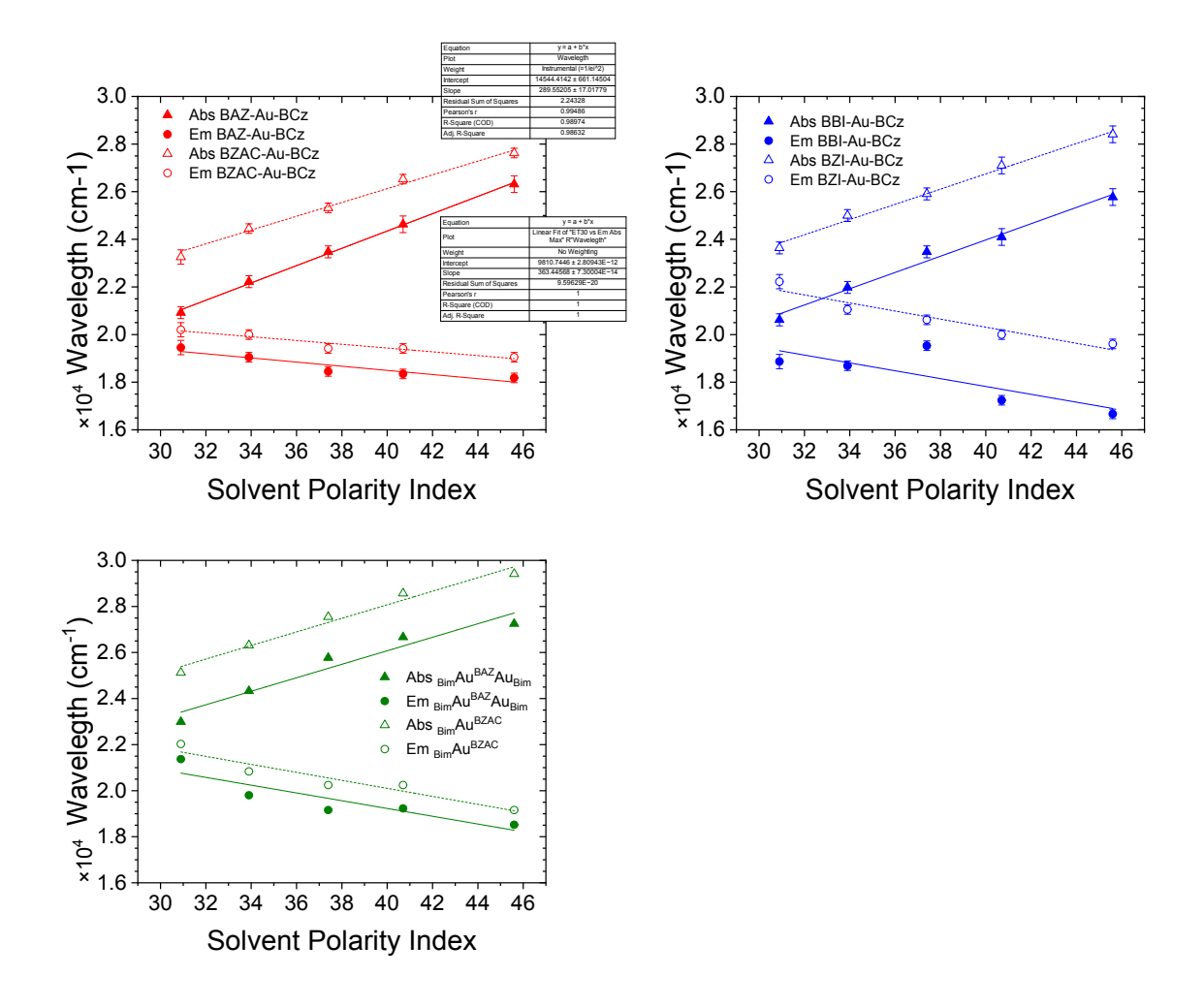


Figure S11. Emission spectra in PS, MeTHF and Me-Cyclo-Hexane at RT and 77K for complexes $_{BCz}Au^{BAZ}Au_{BCz}$, $_{BCz}Au^{BAZ}Au_{BCz}$, $_{BCz}Au^{BAZ}Au_{BCz}$, $_{BCz}Au^{BAZ}Au_{BCz}$ and $_{Bim}Au^{BAZ}Au_{Bim}$

Table S11: Photophysical Data for all BCz and bim compounds in MeCy, 2MeTHF, MeCN and CH_2Cl_2

Complexes	Abs λ_{max}	PL λ_{max}	$\Phi_{ ext{PL}}$	τ	k_r	k_{nr}	λ _{max} 77K	τ 77 Κ
Complexes	(nm)	(nm)	(%)	(µs)	$(10^6 \mathrm{s}^{-1})$	$(10^6 \mathrm{s}^{-1})$	(nm)	(µs) (%)
MeCy								
$_{\mathrm{BCz}}\mathrm{Au^{BAZ}Au_{BCz}}$	478	514	93	0.370	2.5	0.19	480	60
$^{\mathrm{BZAC}}\!\mathrm{Au}_{\mathrm{BCz}}$	430	495	>95	0.637	1.5	< 0.01	430	92 (47) 390 (53)
BCzAu ^{BBI} Au _{BCz}	495	530	>95	0.254	3.8	< 0.01	475	12.84
$^{\mathrm{BZI}}\!\mathrm{Au}_{\mathrm{BCz}}$	423	452	90	0.723	1.2	0.14	438	265
$_{\text{Bim}}Au^{\text{BAZ}}Au_{\text{Bim}}$	435	468	>95	0.265	3.7	0.11	451	790 (62) 273 (38)
$_{\text{Bim}}Au^{\text{BZAC}}$	385	454	>95	0.290	3.4	0.07	400	259
			2-]	MeTHF				
$_{BCz}Au^{BAZ}Au_{BCz} \\$	426	544	83	0.420	2.0	0.4	442	250 (44) 530 (56)
$^{BZAC}Au_{BCz} \\$	395	515	88	0.664	1.3	0.18	430	533(0.35) 875(0.65)
BCzAu ^{BBI} Au _{BCz}	426	551	89	0.278	3.2	0.4	438	80 (25) 307 (75)
$^{\mathrm{BZI}}\!\mathrm{Au}_{\mathrm{BCz}}$	375	485	97	0.868	1.1	0.03	438	358
$_{\text{Bim}}Au^{\text{BAZ}}Au_{\text{Bim}}$	388	522	63	0.327	1.9	1.1	442	563
$_{\text{Bim}}Au^{\text{BZAC}}$	363	494	78	0.310	2.5	0.71	400	467
-				MeCN				
$_{BCz}Au^{BAZ}Au_{BCz}$	360	550	75	0.371	2.0	0.67	-	-
$^{\mathrm{BZAC}}\!\mathrm{Au}_{\mathrm{BCz}}$	375	525	69	0.801	0.86	0.39	-	-
$_{BCz}Au^{BBI}Au_{BCz}$	375	600	34	0.139	2.4	0.47	-	-
$^{BZI}\!Au_{BCz}$	350	510	65	2.82	0.23	0.12	-	-
$_{Bim}Au^{BAZ}Au_{Bim}$	367	540	30	2.468	0.12	0.28	-	-
$_{Bim}Au^{BZAC}$	311	522	42	-	-	-	-	-
CH ₂ Cl ₂								
$_{BCz}Au^{BAZ}Au_{BCz}$	410	545	89	0.374	2.3	0.29	-	-
$^{\mathrm{BZAC}}\!\mathrm{Au}_{\mathrm{BCz}}$	375	515	81	0.664	1.2	0.29	-	
$_{BCz}Au^{BBI}Au_{BCz}$	415	580	77	0.274	2.8	0.84	-	-
$^{\mathrm{BZI}}\!\mathrm{Au}_{\mathrm{BCz}}$	370	500	66	1.80	0.36	0.19	-	-
$_{Bim}Au^{BAZ}Au_{Bim}$	375	520	80	0.581	1.4	0.34	-	-
$_{\text{Bim}}Au^{\text{BZAC}}$	350	494	83	0.325	2.6	0.52	-	-



<u>Figure S12</u>. ET30 plots and linear fits for all complexes. Slopes are listed in Figure 5d. ET 30 Values are the following for: MeCyHex: 30.9, Toluene: 33.9, MeTHF: 37.4, CH₂Cl₂: 40.7 and MeCN: 45.6.

Table S12. The value of solvatochromic shift from MeCN to MeCy

	$_{\mathrm{BCz}}\mathrm{Au^{BAZ}A}$ $\mathrm{u_{BCz}}$	$^{\mathrm{BZAC}}\!\mathrm{Au}_{\mathrm{BCz}}$	_{BCz} Au ^{BBI} A u _{BCz}	$^{\mathrm{BZI}}\mathrm{Au}_{\mathrm{BCz}}$	$_{\mathrm{Bim}}\mathrm{Au^{BAZ}A}$	_{Bim} Au ^{BZAC}
Abs Shift (cm ⁻¹)	5830	4060	6550	4400	4080	4030
em Shift (cm ⁻¹)	1420	1280	2250	2490	2850	2870

Table S13. Photophysical Data for $_{Cz}Au^{BAZ}Au_{Cz}$ based compounds in MeCy, 2MeTHF, MeCN and CH_2Cl_2

	Abs λ_{max} (nm)	PL λ _{max} (nm)	Ф _{РL} (%)	τ (μs)	k_r (10 ⁶ s ⁻¹)	k_{nr} (10 ⁶ s ⁻¹)	λ _{max} 77K (nm)	τ 77 K (μs)
PS	430	476	98	0.33 (0.77) 1.01 (0.16) 5.6 (0.07)	1.2	0.02	476	60 (0.22) 220 (0.58) 590 (0.2)
MeCy	456	478	90	0.39 (0.97) 3.1 (0.03)	1.9	0.21	440	130 (0.44) 370 (0.56)
Tol	430	500	96	0.36	2.2	0.09		
2-MeTHF	405	515	81	0.45 (0.98) 3.09 (0.02)	1.6	0.38	443	380 (0.87) 760 (0.13)

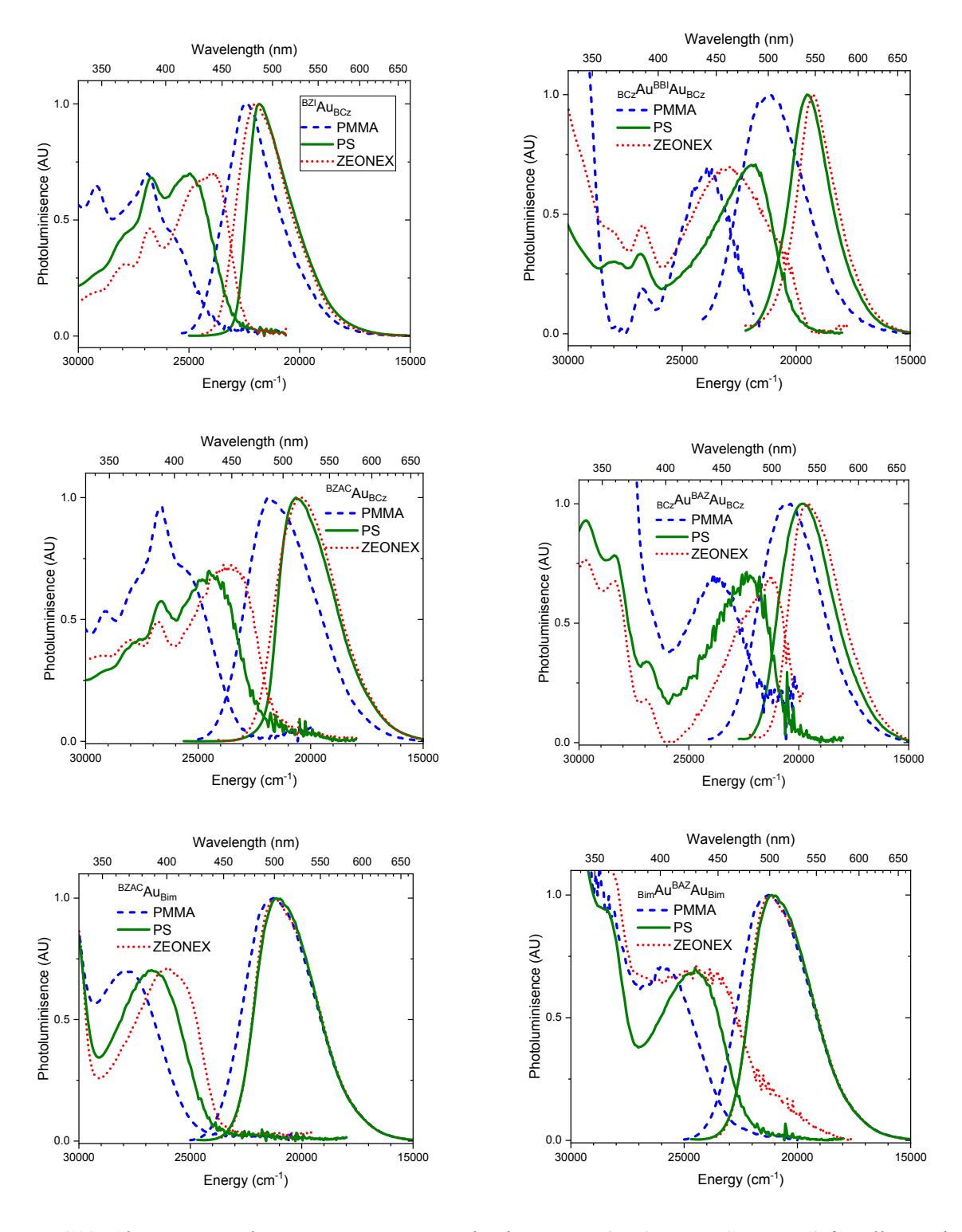


Figure S13: Absorption and Emission spectra in ridged matrixes (ZEONEX, PS, PMMA) for all complexes

Table S14. Photophysical Data for all complexes in the rgid matrixes ZEONEX®, PS and PMMA

Complexes	$\begin{array}{c} \text{Abs} \\ \lambda_{\text{max}} \\ (\text{nm}) \end{array}$	PL λ_{max} (nm)	Φ _{PL} (%)	τ (μs)	k_r (10 ⁶ s ⁻¹)	k_{nr} (10 ⁶ s ⁻¹)	λ_{max} 77K (nm)	τ 77 K (μs) (%)
				Zeonex				
$^{\mathrm{BZI}}\!\mathrm{Au}_{\mathrm{BCz}}$	415	454	92	0.777	1.2	0.1	-	-
$_{BCz}Au^{BBI}Au_{BCz}$	438	518	74	0.24 (0.58) 1.04 (0.42)	-	-	-	-
$^{\mathrm{BZAC}}\!Au_{\mathrm{BCz}}$	426	489	95	0.532	1.8	0.1	-	-
$_{BCz}Au^{BAZ}Au_{BCz} \\$	470	510	69	0.325	2.1	1.0	-	-
_{bim} Au ^{BZAC}	386	452	99	0.250	4.0	0.04	-	-
$_{\text{bim}}Au^{BAZ}Au_{\text{bim}}$	419	472	80	0.325	2.5	0.6	-	_
				PS				
$^{\mathrm{BZI}}\mathrm{Au}_{\mathrm{BCz}}$	402	460	94	1.58 (0.5) 8.98 (0.5)	-	-	445	65 (0.3) 219 (0.7)
$_{BCz}Au^{BBI}Au_{BCz} \\$	455	515	93	0.21	4.3	0.33	505	25
$^{\mathrm{BZAC}}\!\mathrm{Au}_{\mathrm{BCz}}$	409	484	>95	0.72	1.4	< 0.01		
$_{BCz}Au^{BAZ}Au_{BCz}$	450	506	90	0.30	3	0.33	506	50
_{bim} Au ^{BZAC}	374	452	>95	0.28	3.7	<0.01	-	-
$_{\text{bim}}Au^{BAZ}Au_{\text{bim}}$	407	475	76	0.33 (0.8) 2.85 (0.2)	-	-	455	27 (0.2) 346 (0.8)
				PMMA				
$^{\mathrm{BZI}}\!Au_{\mathrm{BCz}}$	368	447	87	34.7 (27%) 261 (73%)	-	-	-	-
$_{BCz}Au^{BBI}Au_{BCz} \\$	420	471	48	0.29 (54%) 1.41 (46%)	-	-	-	-
^{BZAC} Au _{BCz}	387	458	100	3.24 (22%) 20.2 (33%) 11.8 (45%)	-	-	-	-
$_{BCz}Au^{BAZ}Au_{BCz}$	424	487	69	0.36 (65%) 1.40 (35%)	-	-	-	-
$_{\text{bim}}Au^{\text{BZAC}}$	359	440	95	0.280	-	-	-	-
$_{\text{bim}}Au^{BAZ}Au_{\text{bim}}$	388	470	79	1.27 (15%) 10.3 (36%) 68.2 (50%)	-	-	-	-

Table S15. Abs and PL max in Wavenumbers (cm⁻¹) in ZEONEX®, PS and PMMA

Complexes	Abs ZEONEX	PL ZEONEX	ABS PS	PL PS	Abs PMMA	PL PMMA
$^{\mathrm{BZI}}\!\mathrm{Au}_{\mathrm{BCz}}$	24096	22026	24875	21739	27174	22371
$_{BCz}\!Au^{BBI}\!Au_{BCz}$	22831	19305	21978	19417	23810	21231
$^{\mathrm{BZAC}}\!\mathrm{Au}_{\mathrm{BCz}}$	23747	20450	24450	20661	25839	21834
$_{BCz}Au^{BAZ}Au_{BCz} \\$	21277	19608	22222	19763	23696	20534
$_{bim}Au^{BZAC}$	25907	22124	26737	22124	27855	22727
$_{bim}Au^{BAZ}Au_{bim} \\$	23697	21186	24450	21053	25906	21277

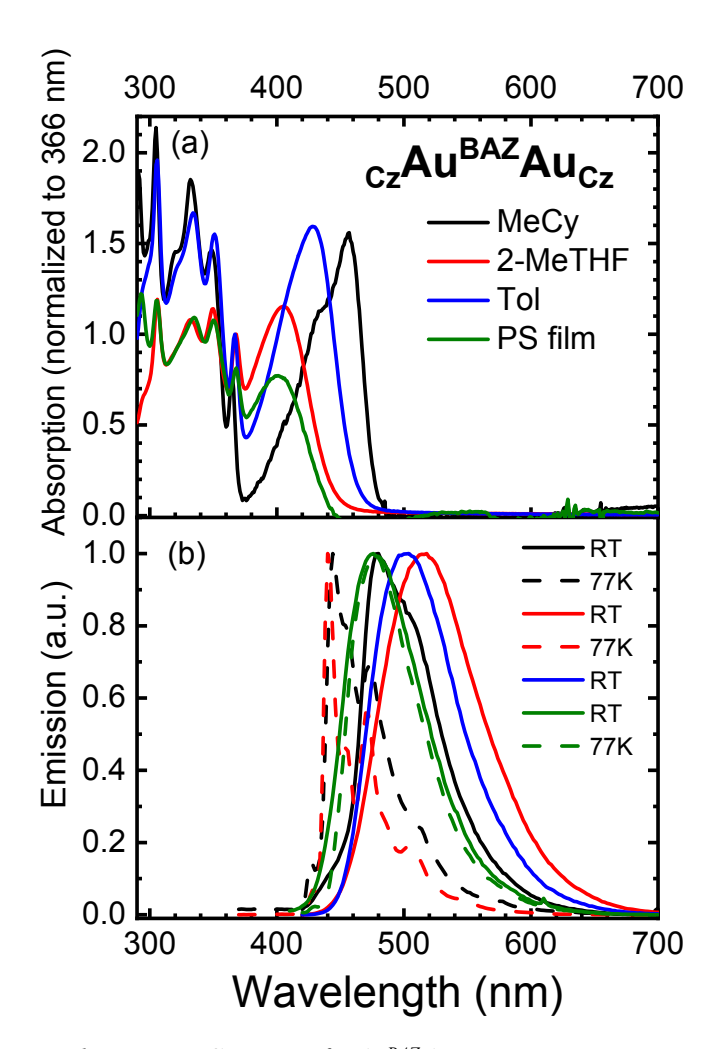


Figure S14. Absorption and Emission Spectra of _{Cz}Au^{BAZ}Au_{Cz}

Temperature Dependent Lifetime Measurements

Cryogenic photophysical measurements were carried out on a Janis SHI-4-2 cryostat with a Lakeshore 335 Temperature controller and evacuated by an Drytel 31 Turbomolecular pump to 1.2*10⁻⁴ mTorr. Doped polystyrene thin films spin coated on a round sapphire substrate were used for good thermal conductivity. Experiments showed that quartz substrates have a too low heat conductivity, and only sapphire is thermally conductive enough, to truly reach 4K inside the PS film. This was checked by measuring the Lifetime of an Ir(ppy)₃ doped PS and PMMA film and cross checked with the data published by Yersin et.al.⁵

The original sample holder was modified in a way, that the emitted light can be collected from the side of the sapphire substrate, as the outcoupling efficiency is highest and the unwanted collected excitation light is minimal in this set-up geometry. See the following figure for the modified sample holder as an inset on the right side.

The emitted light was collimated by an Edmund Optics 45-716 Lens (Focus: 75mm, Ø 50 mm, VIS-NIR coating for 400-1000nm) and focused with an Edmund Optics 47-393 Lens (Focus: 125mm, Ø 50 mm, VIS-NIR coating for 400-1000nm) Lens onto a Thorlabs BF13LSMA02 (400-2200 nm, Ø 1.3 mm) optical fiber connected to a Thorlabs bifurcated fiber BF19Y2LS02 (250-1200 nm, 19 Fiber, Ø 200 μ m) with 10 fibers ending in the TCSPC and 9 Fibers in the Spectrafluorimeter.



Emission spectra were collected with a Photon Technology International QuantaMaster spectrofluorimeter. As Excitation source a 365nm LED

(Thorlabs M365L3 365nm LED, 1000 mW) equipped with the Thorlabs SM1U25-A Adjustable Collimation Adapter and driven with a Thorlabs LEDD1B driver.

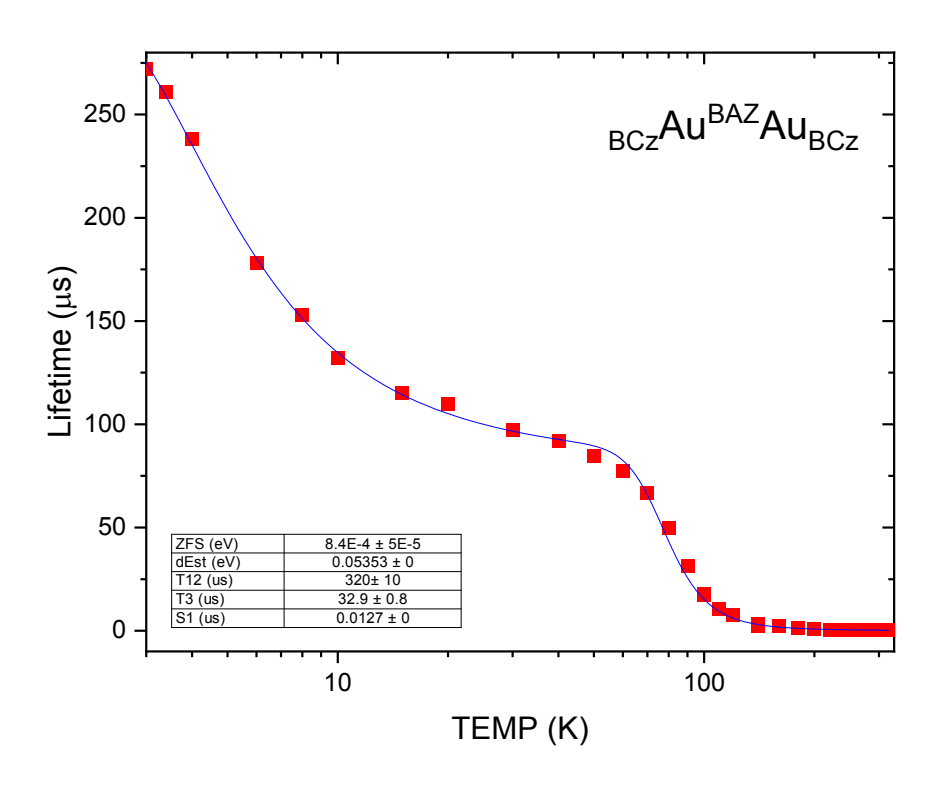
For luminescence lifetime studies a Horibia Fluorohub+ with a Horiba Jobin Yvon detector with monochromator was used. As excitation source a NanoLED 407N (405 nm) or IBH SpectraLED S-03 (372 nm) was used.

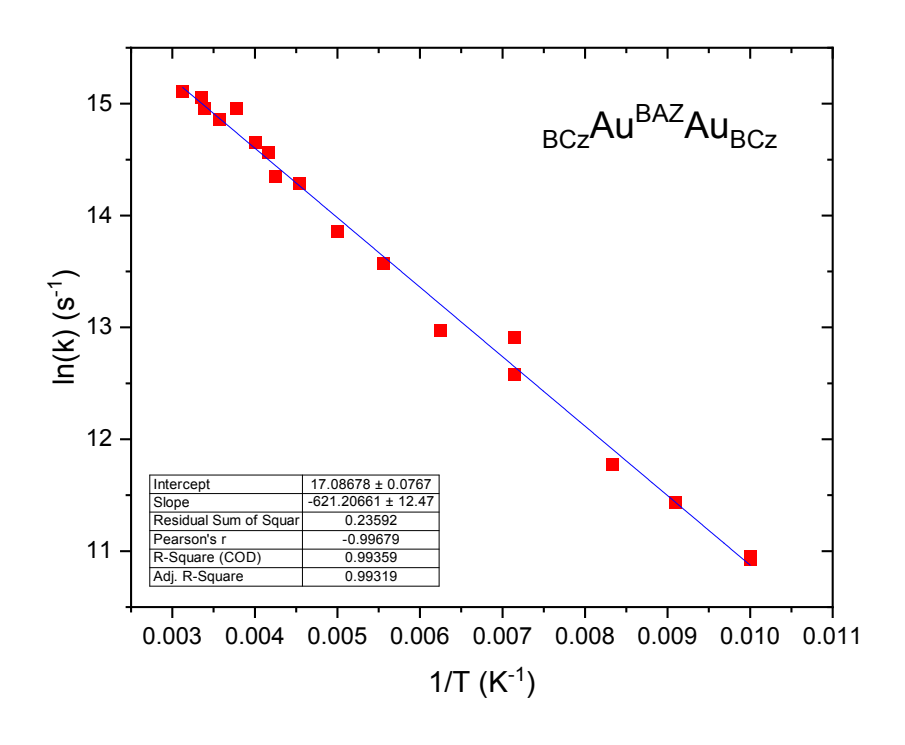
Values for the measured lifetime were plotted against temperature to obtain the plots in the following figures. High temperature data from 150 K – 300 K were fitted to an Arrhenius equation according to Hamze, et al.⁶ The plots of $\ln(k_{TADF})$ vs. 1/T are given below with their linear fit values. ΔE_{ST} and τ_{S1} was obtained from the slope and intercept respectfully.

Zero-Field Splitting (ZFS) and τ_{T3} was obtained from Boltzmann fits of the plots Lifetime vs. Temperature with the following fit equation:

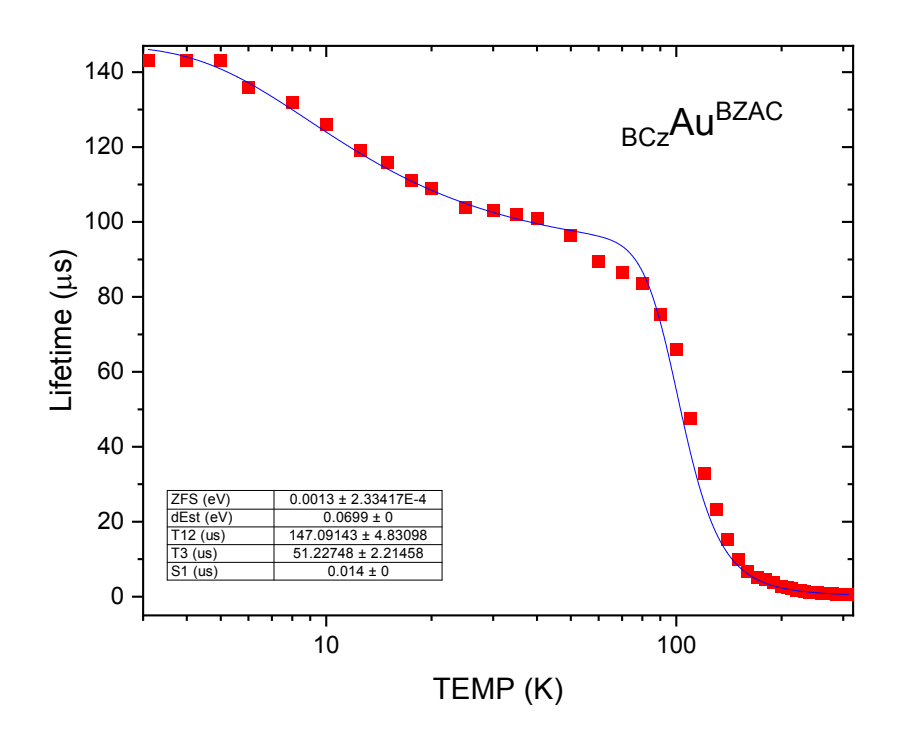
$$\tau = \frac{2 + e^{-\frac{\Delta E(III - I,II)}{k_B T}} + e^{-\frac{\Delta E(S_1 - I,II)}{k_B T}}}{2(\frac{1}{k_{I,II}}) + (\frac{1}{k_{III}})e^{-\frac{\Delta E(III - I,II)}{k_B T}} + (\frac{1}{k_{fl}})e^{-\frac{\Delta E(S_1 - I,II)}{k_B T}}$$

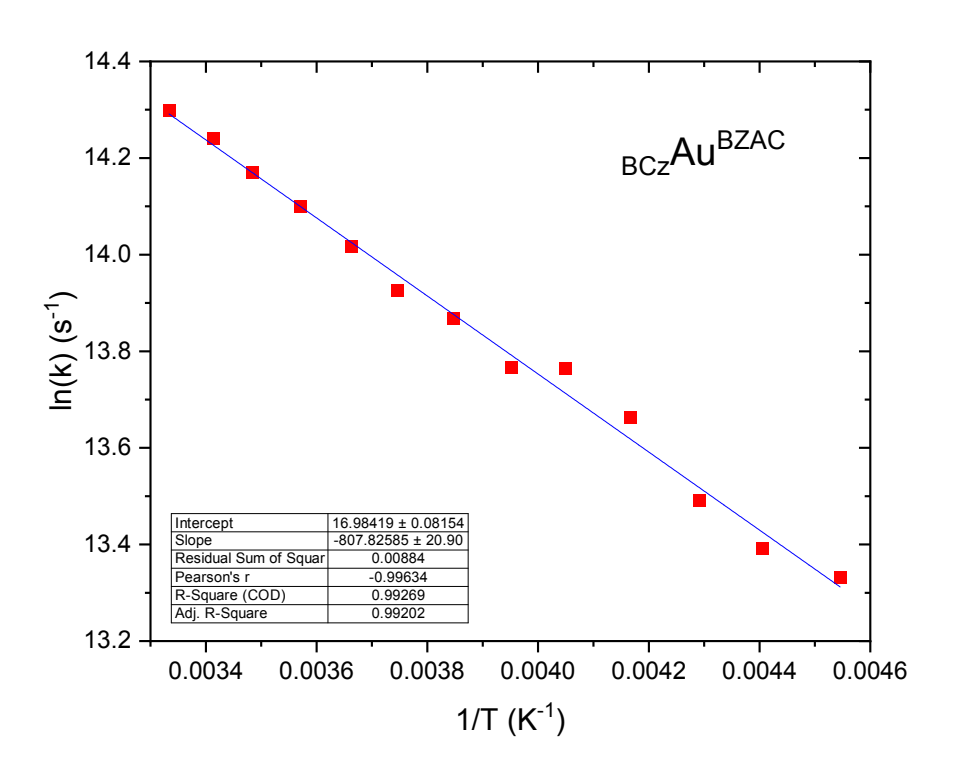
Statistical weighing was used in fits to prevent a higher contribution of long lifetimes. The previously determined $\Delta E_{\rm ST}$ and $\tau_{\rm S1}$ were used as fixed parameters in the equation. $\tau_{\rm T1,2}$ could not be reliably determined due to insufficient data below 4 K.



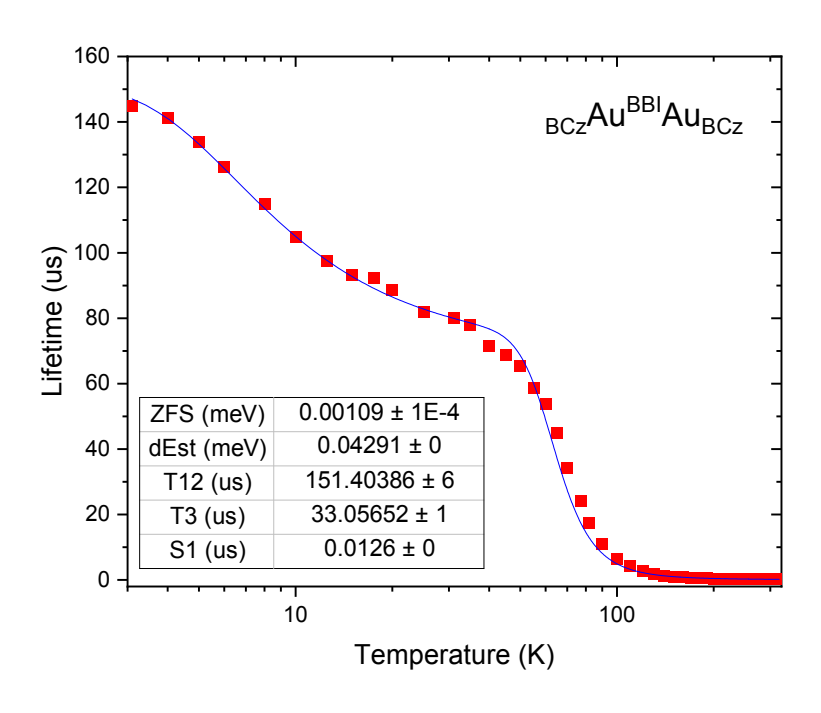


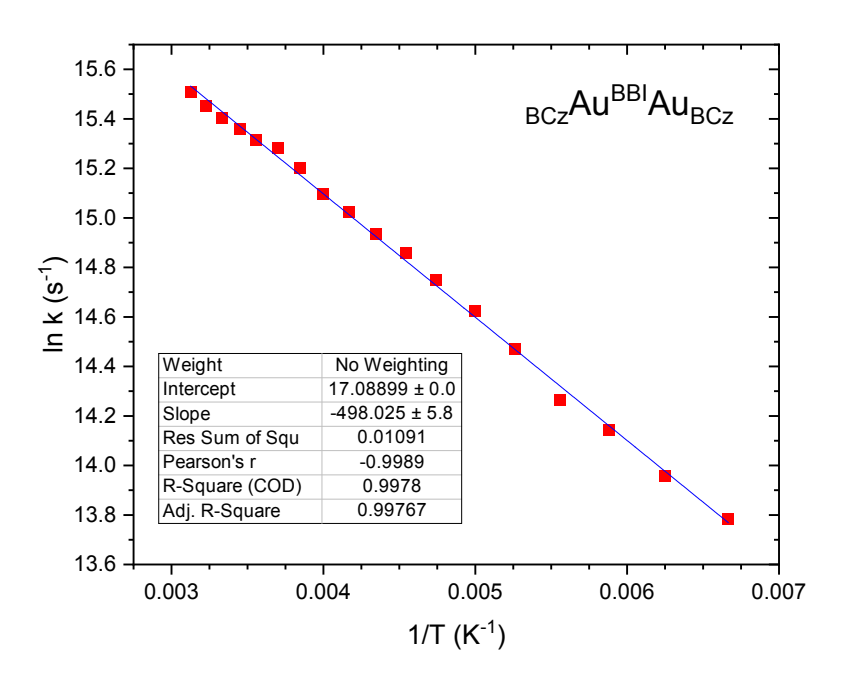
<u>Figure S15a</u>: Temperature dependent lifetime for $_{BCz}Au^{BAZC}Au_{BCz}$ in PS. Boltzmann fit (top) and Arrhenius plot (bottom).



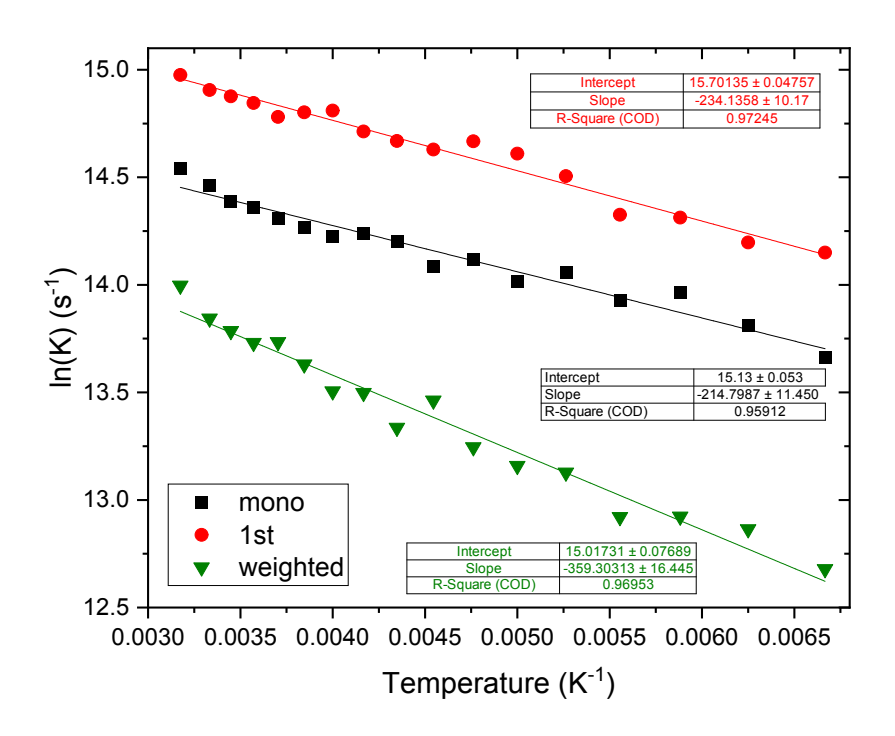


<u>Figure S15b</u>: Temperature dependent lifetime for ^{BZAC}Au_{BCz} in PS. Boltzmann fit (top) and Arrhenius plot (bottom).





<u>Figure S15c</u>: Temperature dependent lifetime for $_{BCz}Au^{BBI}Au_{BCz}$ in PS. Boltzmann fit (top) and Arrhenius plot (bottom).



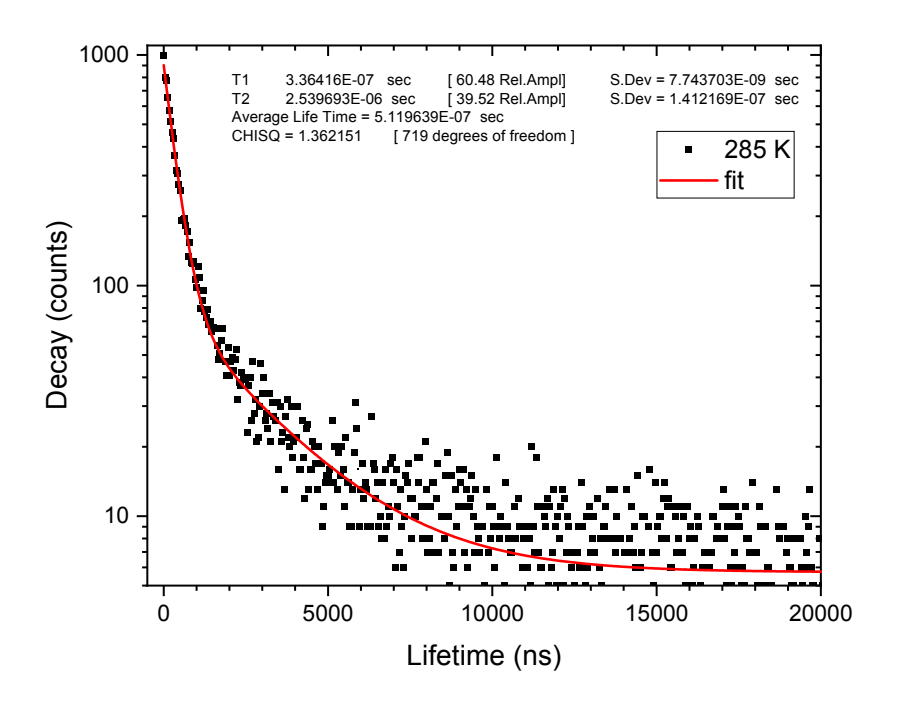
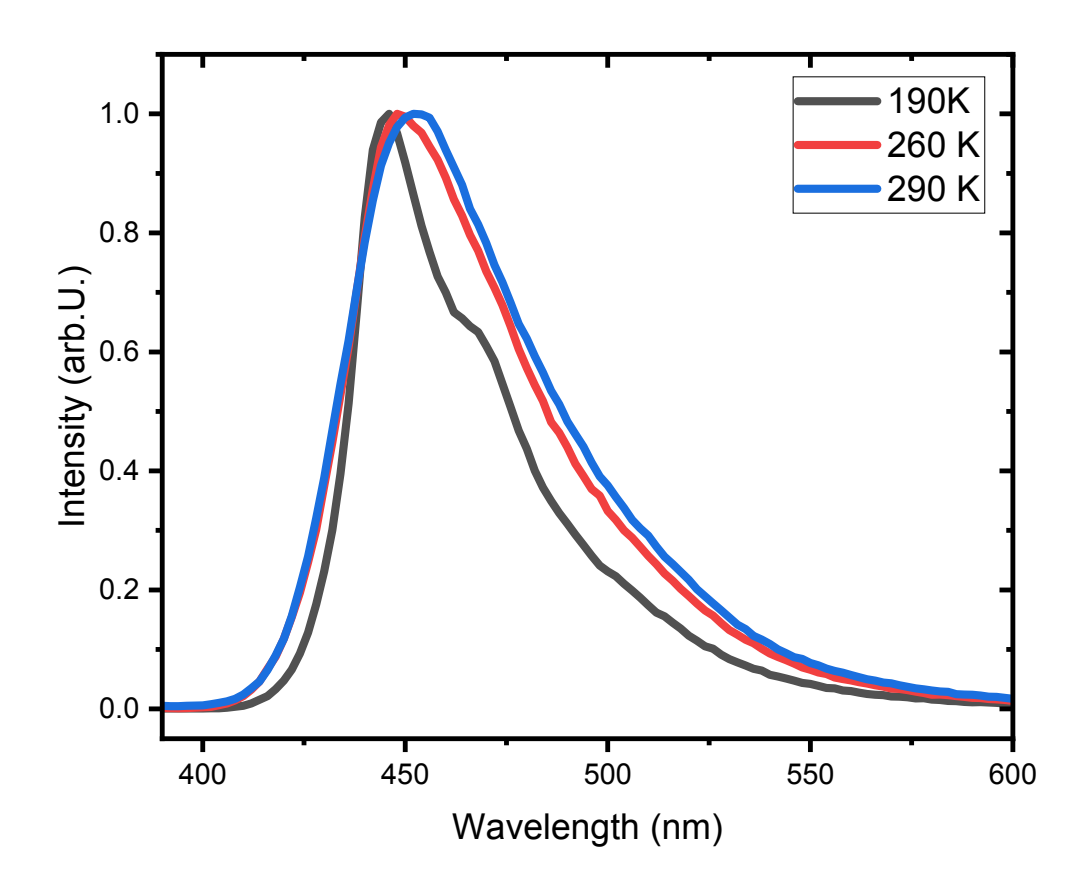


Figure S16: Temperature dependent lifetime for $_{Bim}Au^{BAZC}Au_{Bim}$ in PS. Arrhenius plots (top) for the 1^{st} and 2^{nd} component of the fitted Lifetime data in addition to the weighted average are shown. Only the Fit for the 1^{st} component is used, to determine ΔEST and S_1 , as the ratios between the components was constant in the shown temperature range and the 2^{nd} component is attributed to aggregation. The fitted lifetime data for 298K is shown as representative example (bottom).



<u>Figure S17</u>: Temperature dependent emission for ^{BZI}Au_{BCz} in PS. ³LE emission and ICT emission is visible in the emission spectra, with higher influence at lower temperatures. The lifetime is biexponential at and below room temperature with increasing contribution of the slower component towards lower temperatures, indicating a increasing influence of the ³LE emission to the overall lifetimes towards lower energies.

OLED Device Studies

OLED devices were fabricated on pre-patterned ITO-coated glass substrates ($20 \pm 5 \Omega$ cm2, Thin Film Devices, Inc.). Prior to deposition, the substrates were cleaned with soap, rinsed with deionized water and sonicated for 10 minutes. Afterwards, two subsequent rinses and 15-minute sonication baths were performed in acetone and isopropyl alcohol sequentially, followed by 15 min UV ozone exposure. After the MoO_x deposition (5nm) with an EvoVac (Angstrom Engineering) the substrates were transferred without contact to air into a particle free Nitrogen Glovebox. The EML was spin coated from a toluene solution, which was stirred overnight at 65 C and filtered before usage. A consistent thickness of 30 nm was achieved with 65 μ L of solution with concentration of 8mg per mL toluene at a spin rate of 3000 rpm for 90s. If applicable substrates were annealed under N_2 atmosphere for 10min @110C. Transfer into the deposition system occurred without contact to air. TPBi (ETL) was deposited using a Vacuum Thermal Evaporation (Angstrom Engineering) and the Cathode (Liq and Al) was deposited using a Vacuum Thermal Evaporation (Kurt J. Lesker).

Current-voltage-luminescence (J-V-L) curves were measured in an by using a Keithley power source meter model 2400 and a Newport multifunction optical model 1835-C, PIN-220DP/SB blue enhanced silicon photodiodes (OSI optoelectronics Ltd.). The sensor was set to measure power at an energy of 520 nm, followed by correcting to the average electroluminescence wavelength for each individual device during data process. Electroluminescence (EL) spectra of OLEDs were measured using the fluorimeter (model C-60 Photon Technology International QuantaMaster) at several different voltages. Thicknesses were determined on Silicon wafers using a Filmsense FS-1 Ellipsometer.

PEDOT:PSS based solution OLED devices have a large hole injection barrier, indicated by the high turn-on voltage ($V_{\rm on}$, defined at brightness of 1 cd/m²) generally around 4 to 6 V.7 MoO_x has not been widely used in OLEDs as a HIL despite the suitable frontier energies (-9.7 eV/-5.5 eV). A device with MoO_x as the HIL with structure ITO/ MoO_x (5 nm)/ 20% $_{\rm BCz}$ Au $^{\rm BBI}$ Au $_{\rm BCz}$ in TCTA (30 nm)/TPBi (50 nm)/Liq (1.5 nm)/Al (100 nm), was fabricated. Pure PL spectrum (0.28, 0.61) has been observed for the device. The MoO_x device exhibits much better current conduction and luminance than the PEDOT device in literature at a certain voltage as shown in the current-luminance-voltage (J-L-V). The turn-on voltage ($V_{\rm on}$, defined at brightness of 1 cd/m²) is

2.8 V for the MoO_x devices. At 4.8 V, the MoO_x device gives a current density of 10 mA/cm^2 and a luminance 3423 cd/m^2 . The absence of MoOx as an HIL leads to a high high dark current and therefore poor device performance. Furthermore, in the absence of PEDOT:PSS in the devices, annealing is not required. The devices with the same structure were fabricated, with and without annealing of the EML layer after spin coating. Their *J-L-V* characteristics are found to be similar.

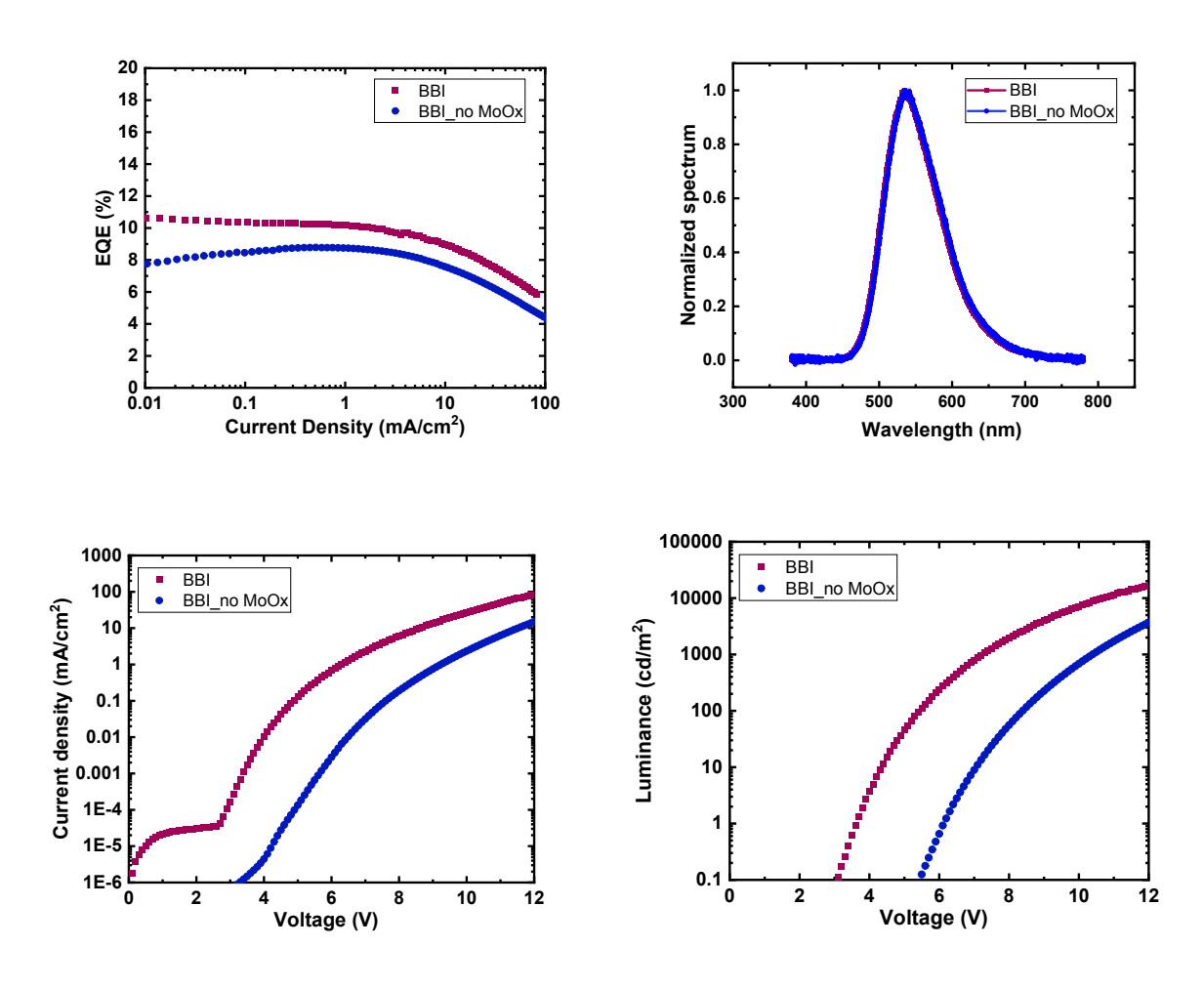


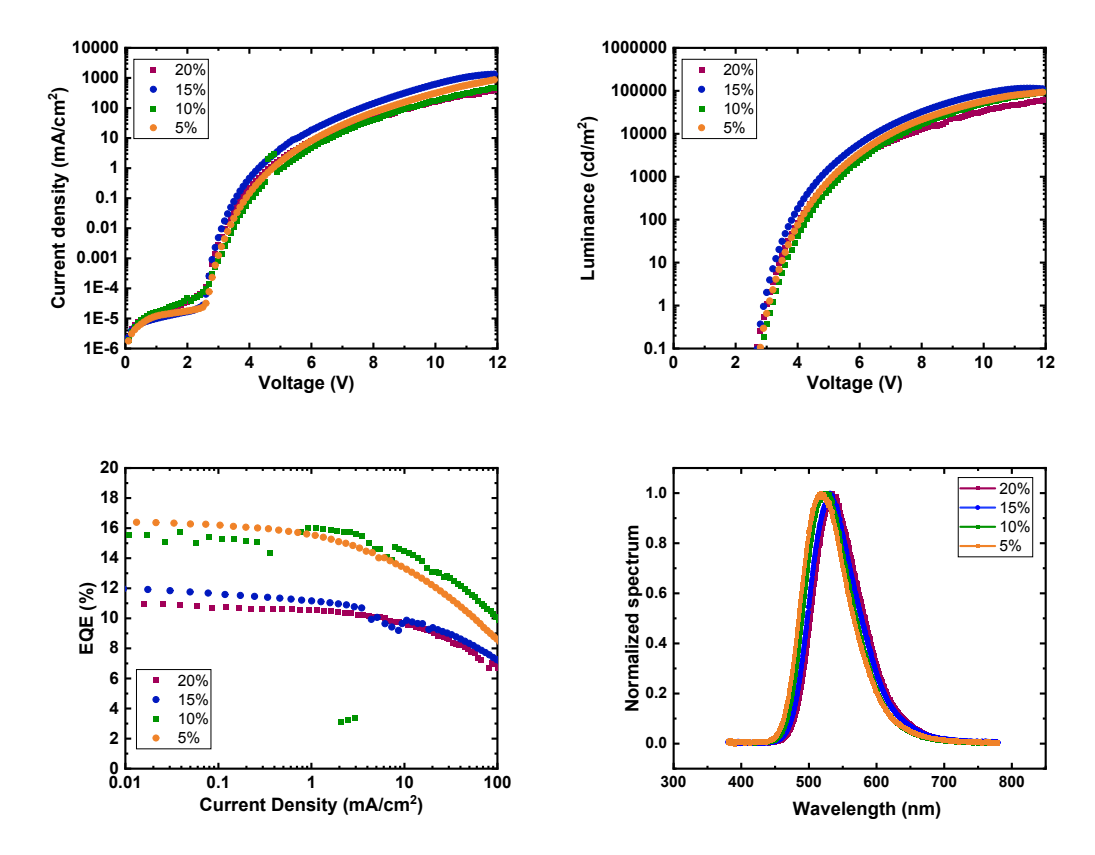
Figure S18. OLED Devices with 20% BCzAuBBIAuBCz in TCTA as host material.

Red: 5nm MoO_x , device structure: ITO/MoO_x (5 nm)/20 % $_{BCz}Au^{BBI}Au_{BCz}$ dopants in TCTA (30 nm)/ TPBi (50 nm)/Liq (1.5 nm)/Al (100 nm)

Blue: no MoO_x , device structure: ITO/20 % $_{BCz}Au^{BBI}Au_{BCz}$ dopants in TCTA (30 nm)/TPBi (50 nm)/Liq (1.5 nm)/Al (100 nm)

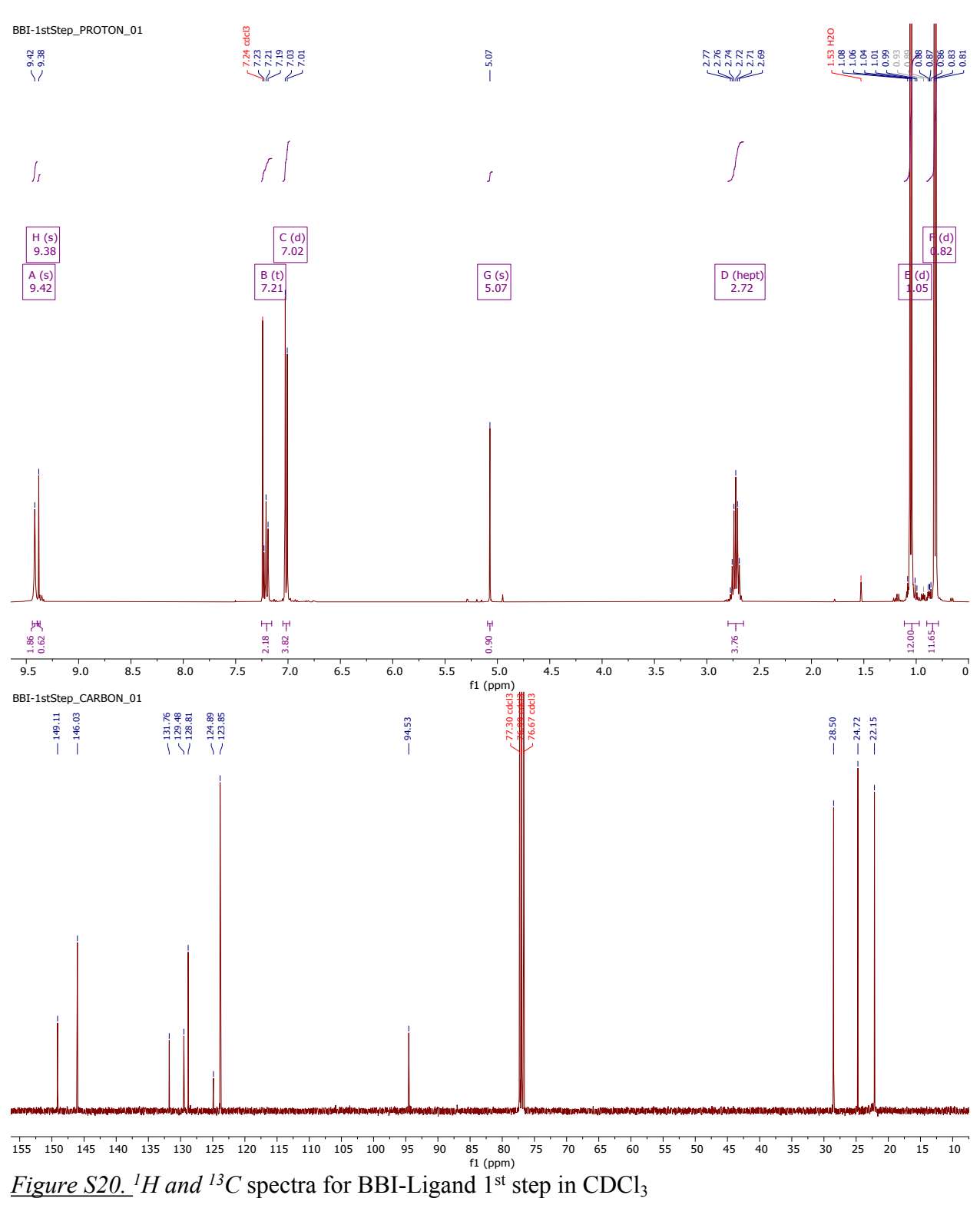
Table S16: Photoluminescence data of binuclear complexes and $^{MAC}Au_{Cz}$ in the host material TCTA.

Emitter	Conc. in	= (0/)	τ	k_r	k_{nr}
Emitter	TCTA	$\Phi_{ m PL}(\%)$	(ns)	$(10^6 s^{-1})$	$(10^6 \mathrm{s}^{\text{-}1})$
BCzAu ^{BBI} Au _{BCz}	5	86	203	4.2	0.7
	10	74	209	3.5	1.2
	20	63	232	2.7	1.6
_	30	46	176	2.6	3.0
BCzAuBAZAuBCz	5	64	277	2.3	1.3
BCZAU AUBCZ -	10	50	250	2.0	2.0
MACAu _{Cz}	5	100	752	1.3	<0.01
	10	79	752	1.1	0.28



<u>Figure S19.</u> Doping concentration-controlled OLED devices with $_{BCz}Au^{BBI}Au_{BCz}$ and TCTA as host material with the following device structure: ITO/MoO_3 (5 nm)/X% $_{BCz}Au^{BBI}Au_{BCz}$ in TCTA (30 nm)/TPBi (50 nm)/Liq (1.5 nm)/Al (100 nm)

NMR spectra



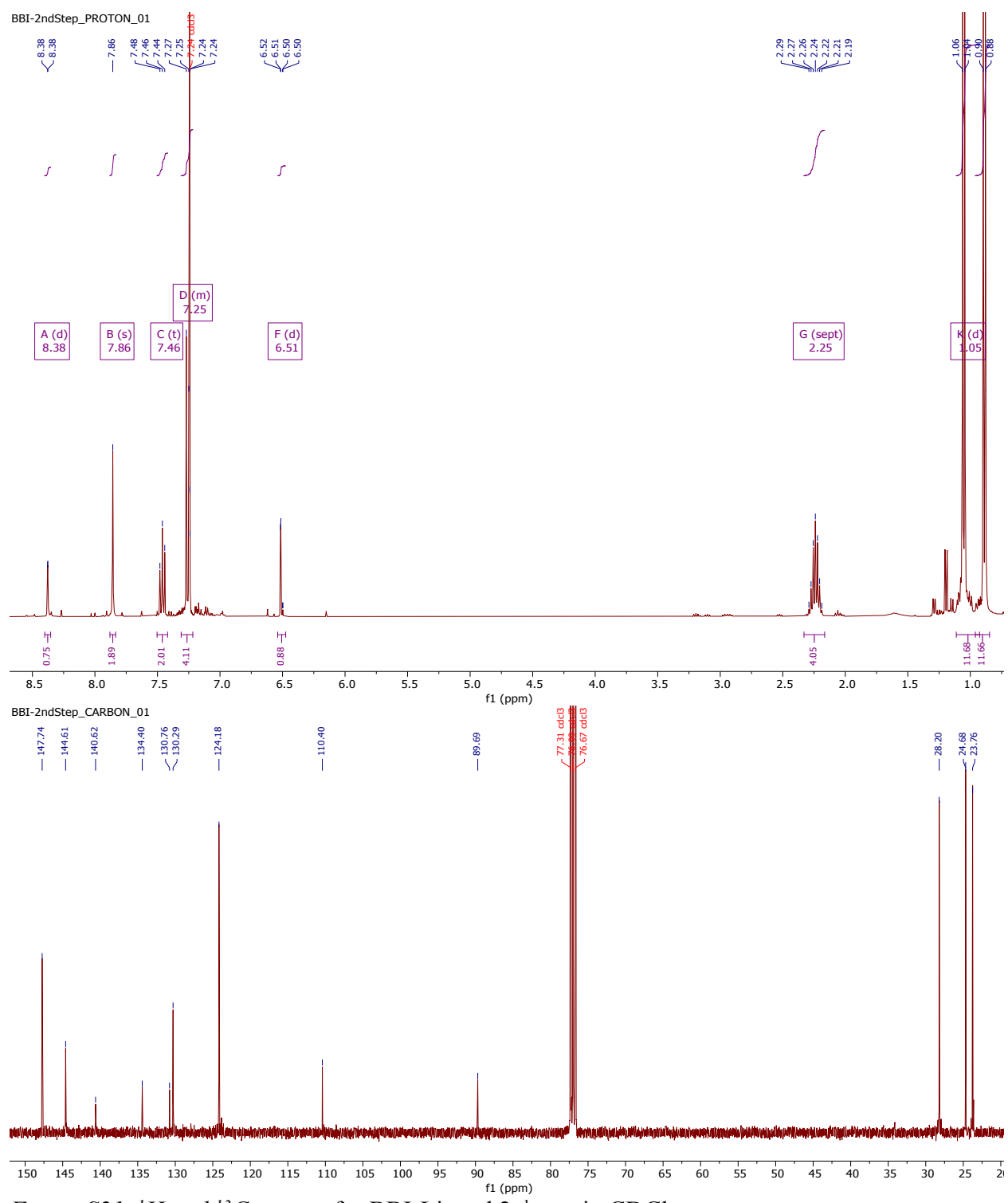
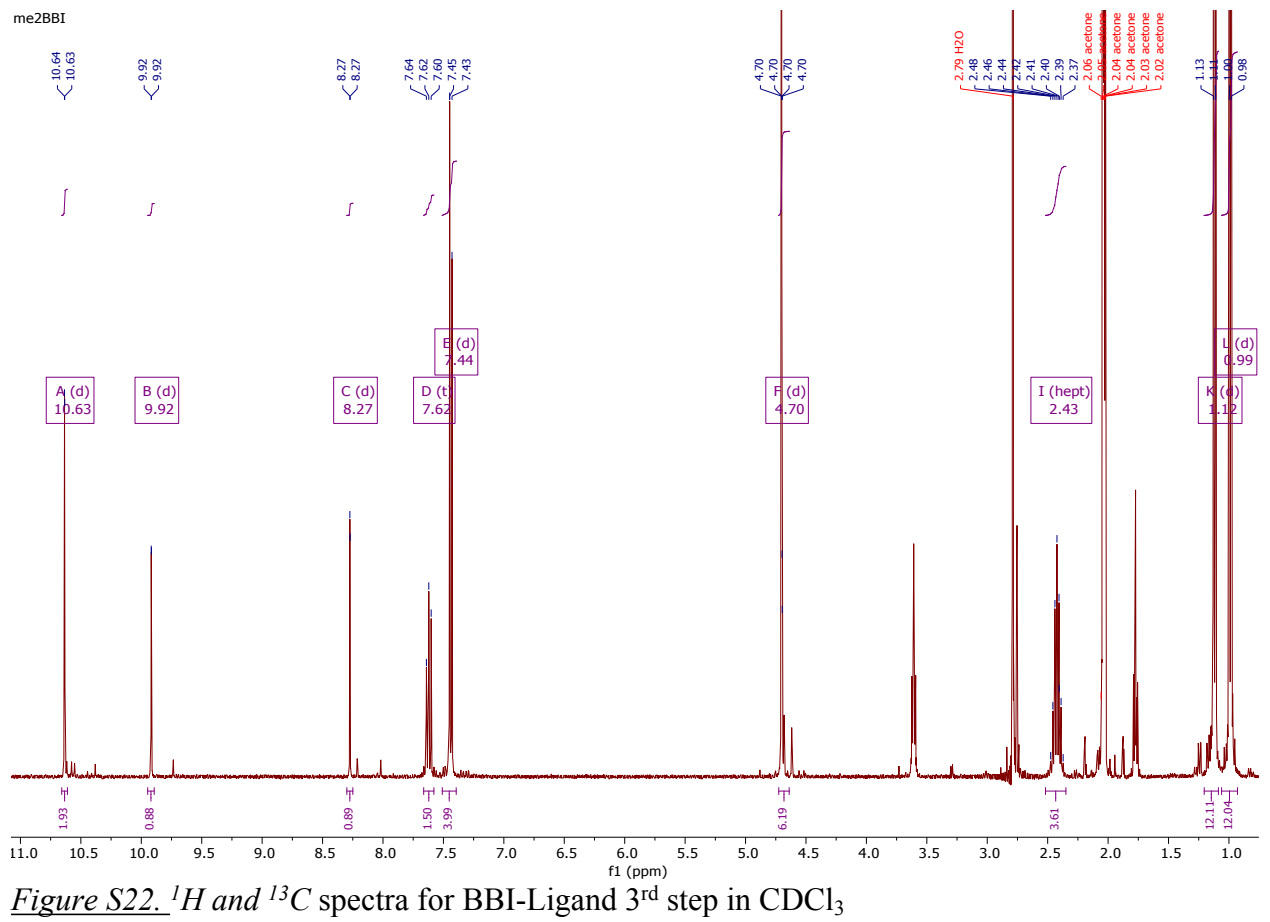


Figure S21. ¹H and ¹³C spectra for BBI-Ligand 2nd step in CDCl₃



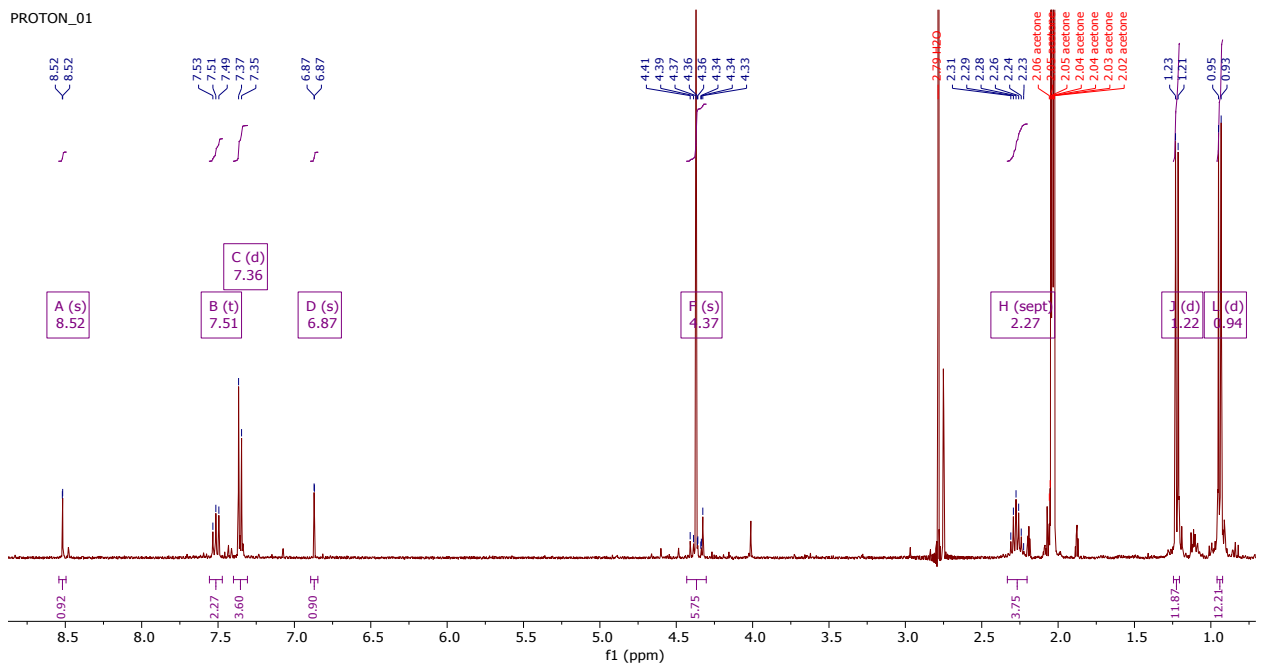


Figure S23. ¹H spectra for ClAuBBIAuCl in acetone-d6

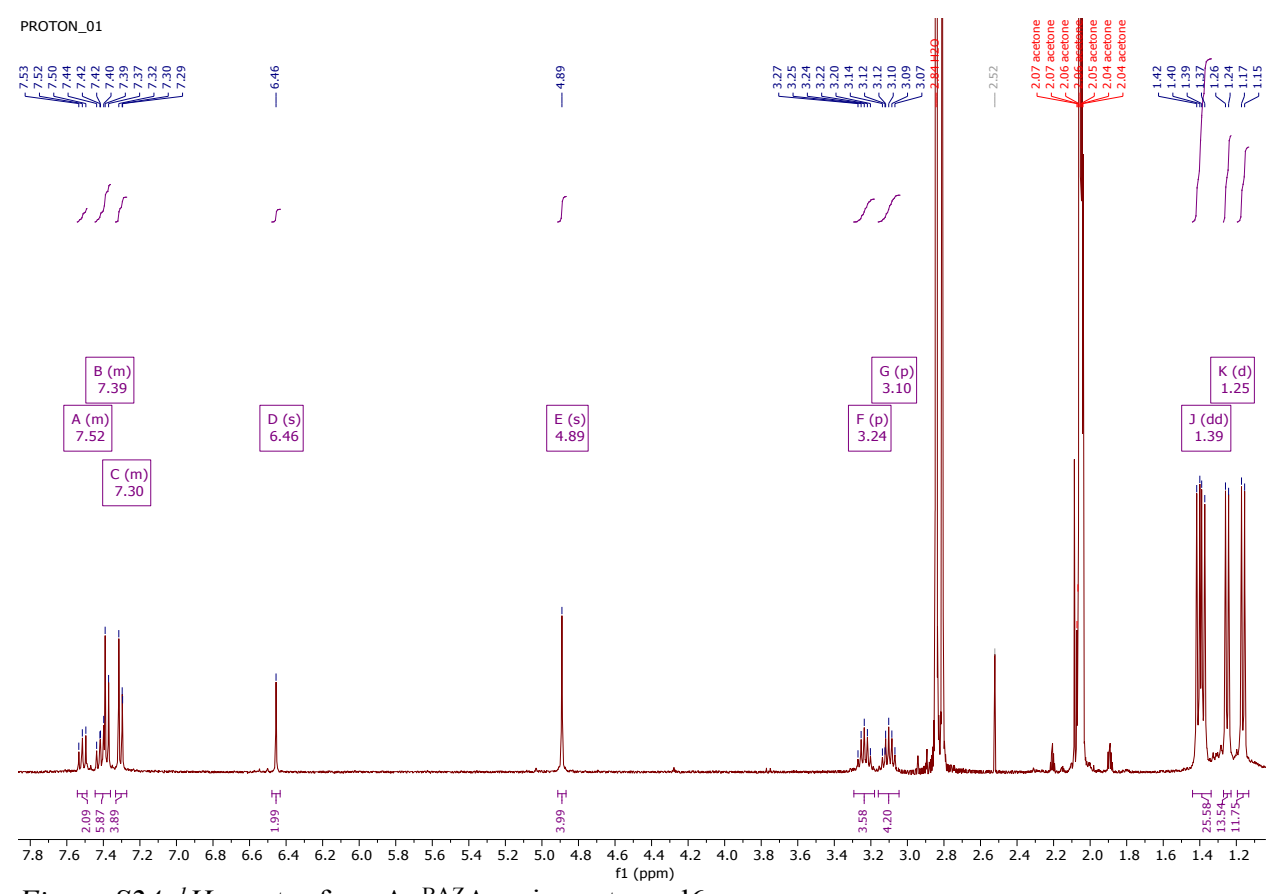
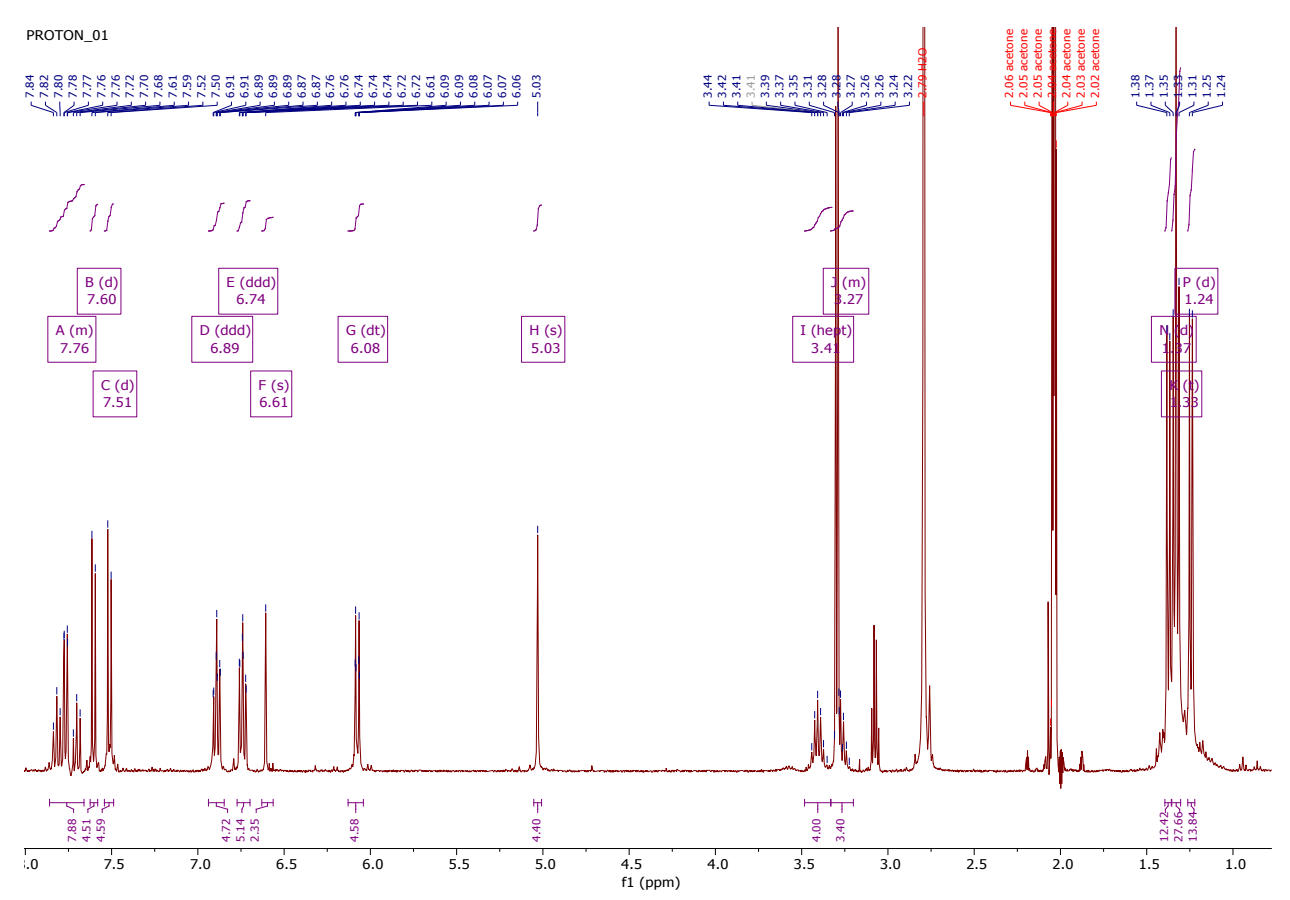
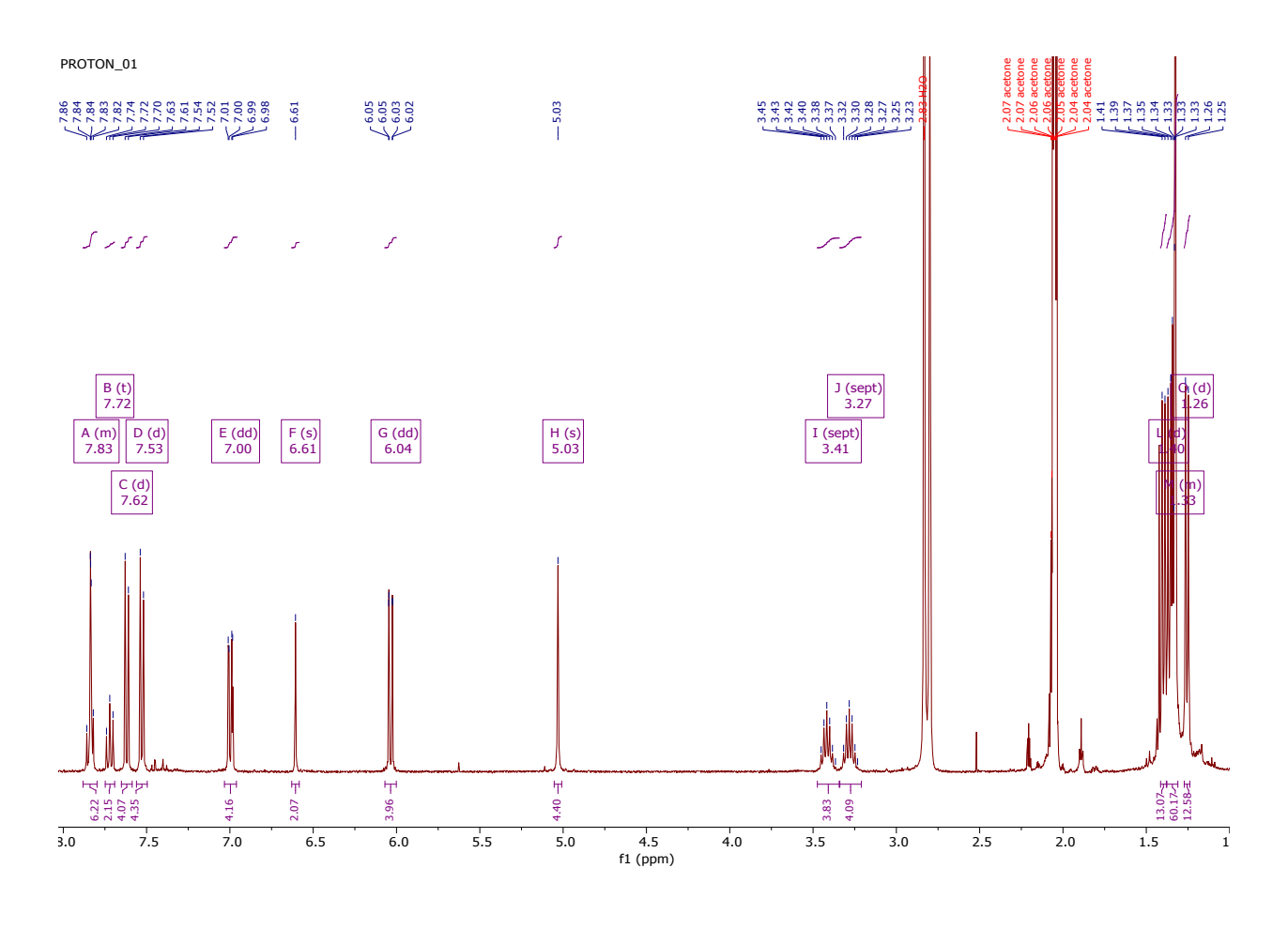


Figure S24. ¹H spectra for ClAu^{BAZ}Au_{Cl} in acetone-d6



<u>Figure S25.</u> ^{I}H and ^{I3}C spectra for $_{Cz}Au^{BAZ}Au_{Cz}$ in acetone-d6



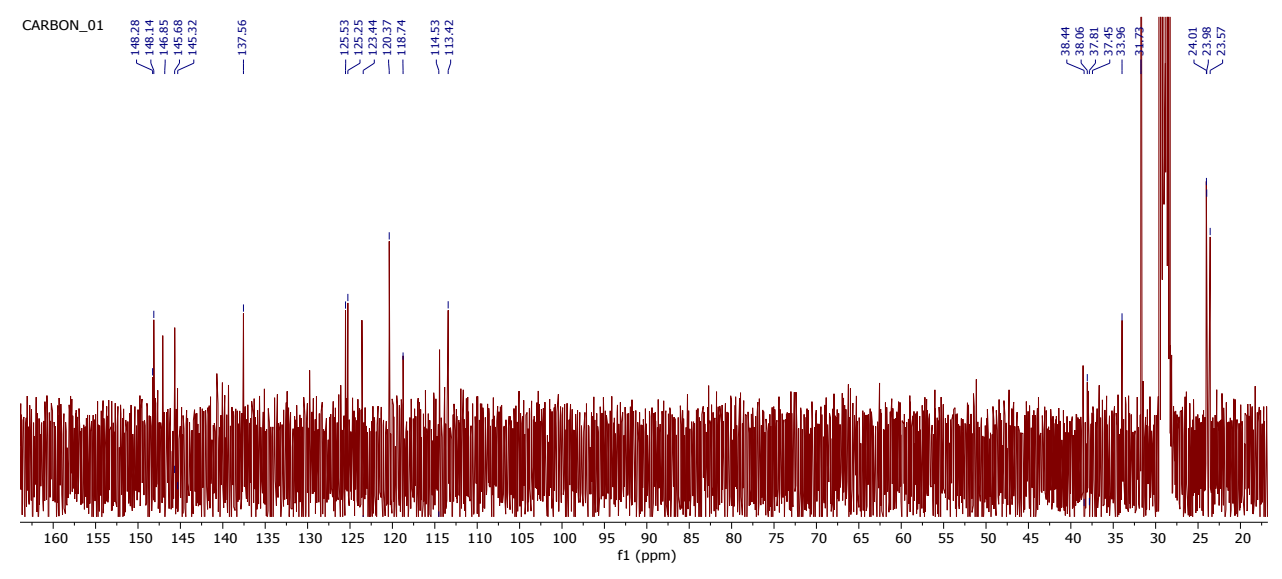


Figure S26. ¹H and ¹³C spectra for _{BCz}Au^{BAZ}Au_{BCz} in acetone-d6

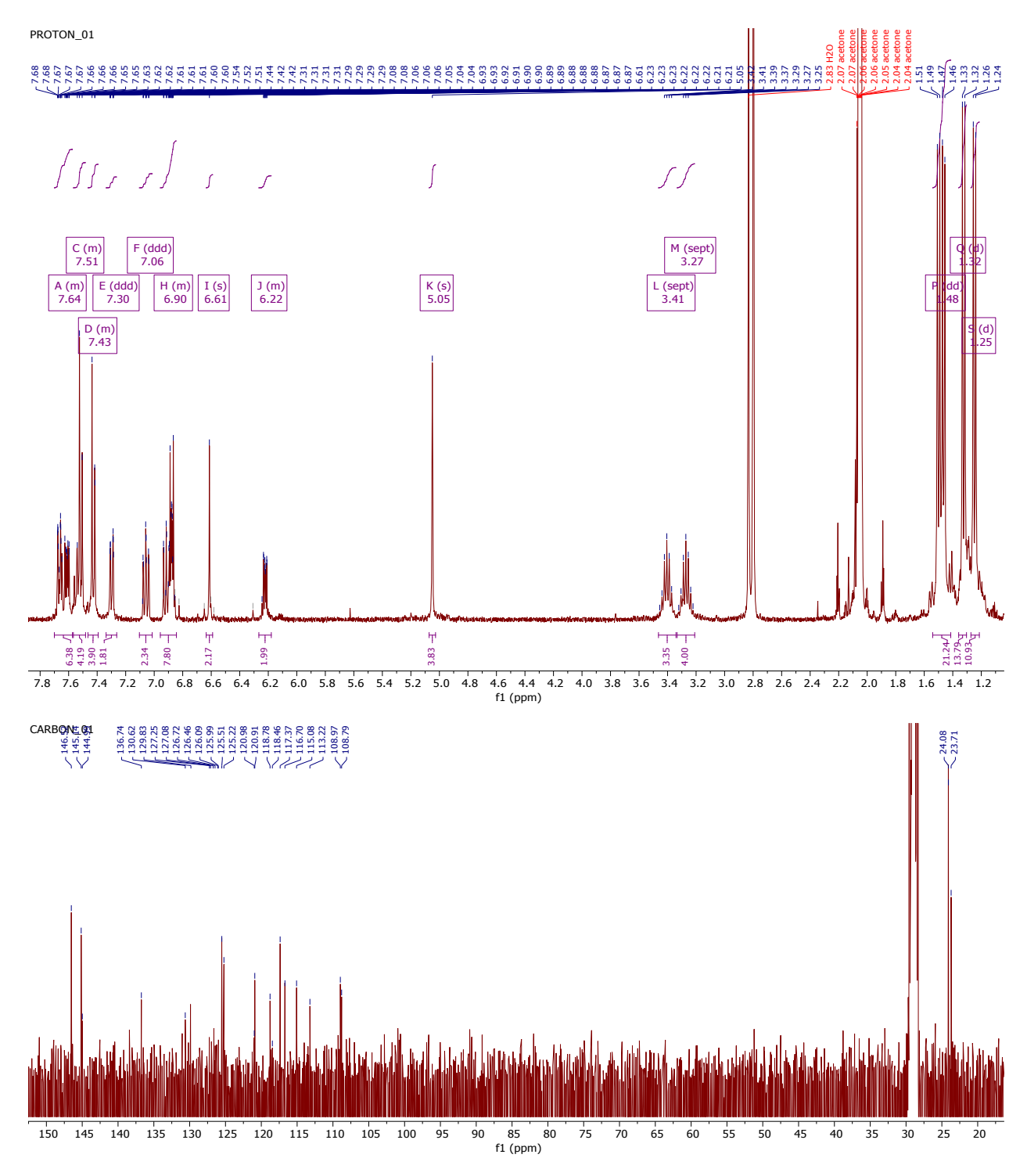


Figure S27. ^{1}H and ^{13}C spectra for $_{Bim}Au^{BAZ}Au_{Bim}$ in acetone-d6

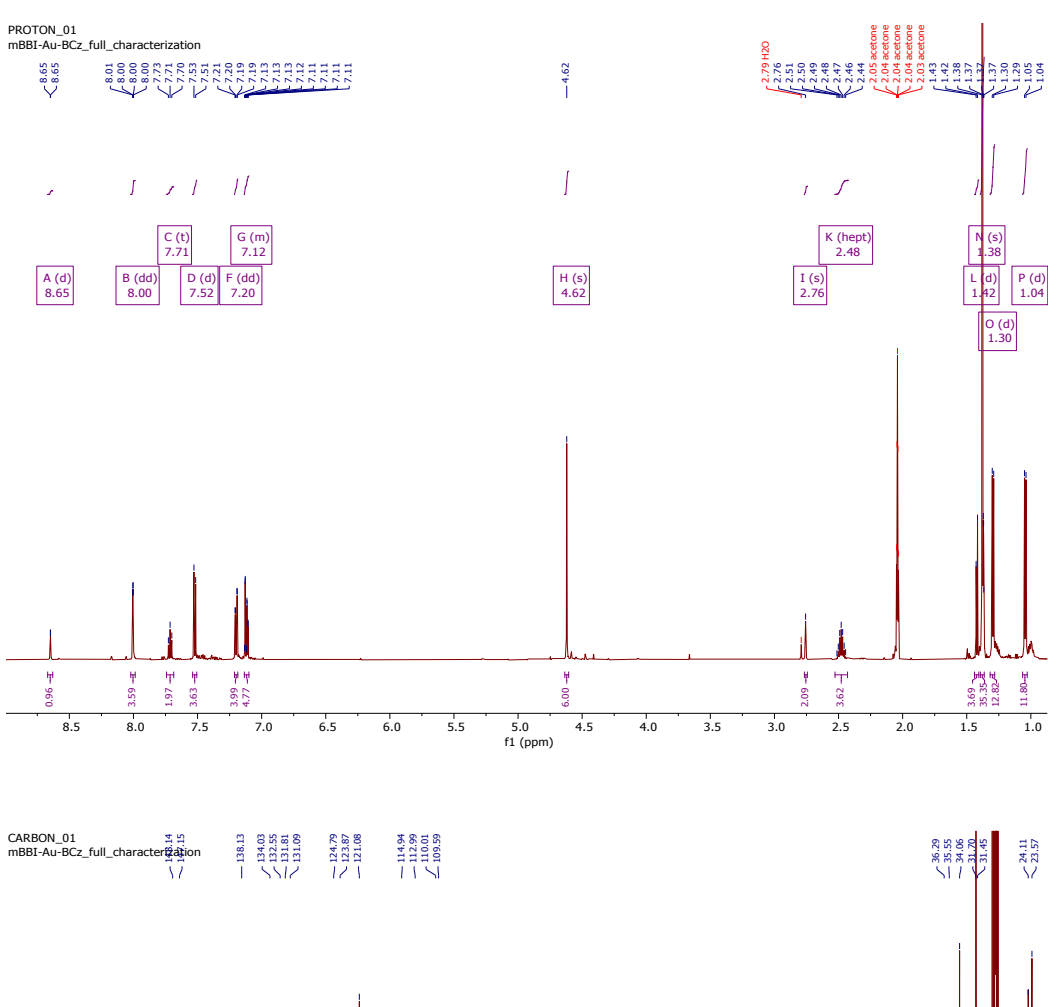
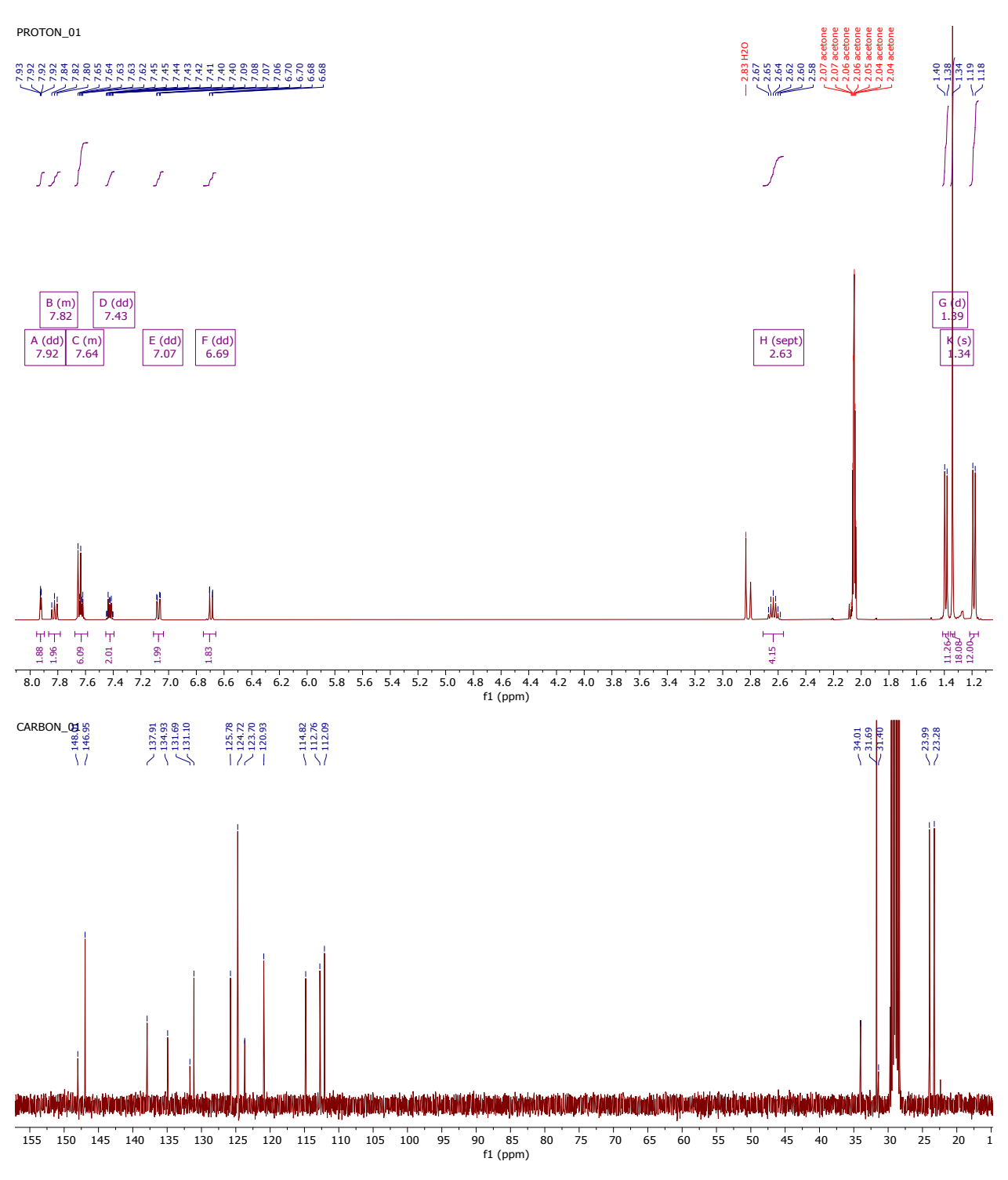


Figure S28. ¹H and ¹³C spectra for _{BCz}Au^{BBI}Au_{BCz} in acetone-d6



<u>Figure S29.</u> ^{1}H and ^{13}C spectra for $^{BZI}Au_{BCz}$ in acetone-d6

References

- 1. Shen, W.; Li, J.; Zhang, C.; Shi, M.; Zhang, J., Copper, Silver and Sodium Salt-Mediated Quaternization by Arylation: Syntheses of N-Heterocyclic Carbene Precursors and 6-H-Phenanthridine Derivatives. *Chemistry An Asian Journal* **2016**, *11* (13), 1883-1886.
- 2. Muniz, C. N.; Schaab, J.; Razgoniaev, A.; Djurovich, P. I.; Thompson, M. E., π -Extended Ligands in Two-Coordinate Coinage Metal Complexes. *Journal of the American Chemical Society* **2022**, *144* (39), 17916-17928.
- 3. Hamze, R.; Idris, M.; Muthiah Ravinson, D. S.; Jung, M. C.; Haiges, R.; Djurovich, P. I.; Thompson, M. E., Highly Efficient Deep Blue Luminescence of 2-Coordinate Coinage Metal Complexes Bearing Bulky NHC Benzimidazolyl Carbene. *Frontiers in Chemistry* **2020**, 8.
- 4. Sheldrick, G., Crystal structure refinement with SHELXL. *Acta Crystallographica Section C* **2015**, 71 (1), 3-8.
- 5. Hofbeck, T.; Yersin, H., The Triplet State of fac-Ir(ppy)3. *Inorganic Chemistry* **2010**, *49* (20), 9290-9299.
- 6. Hamze, R.; Shi, S.; Kapper, S. C.; Muthiah Ravinson, D. S.; Estergreen, L.; Jung, M.-C.; Tadle, A. C.; Haiges, R.; Djurovich, P. I.; Peltier, J. L.; Jazzar, R.; Bertrand, G.; Bradforth, S. E.; Thompson, M. E., "Quick-Silver" from a Systematic Study of Highly Luminescent, Two-Coordinate, d10 Coinage Metal Complexes. *Journal of the American Chemical Society* **2019**, *141* (21), 8616-8626.
- 7. Huang, F.; Liu, H.; Li, X.; Wang, S., Enhancing hole injection by processing ITO through MoO3 and self-assembled monolayer hybrid modification for solution-processed hole transport layer-free OLEDs. *Chemical Engineering Journal* **2022**, *427*, 131356.